

AN ABSTRACT OF THE THESIS OF

Hyungmo Yoo for the degree of Doctor of Philosophy in Electrical and Computer Engineering presented on May, 11, 1990.

Title: Effect of Structural Parameters on Resonant Tunneling Diode Performance

Abstract approved: Redacted for privacy

John R. Arthur

The influence of structural parameters on resonant tunneling diode (RTD) performance is described in this thesis. $\text{Al}_x\text{Ga}_{1-x}\text{As}/\text{In}_y\text{Ga}_{1-y}\text{As}$ resonant tunneling diodes grown by molecular beam epitaxy (MBE) with a symmetric and asymmetric spacer layer have been fabricated and tested via electric and high magnetic field measurements.

The device performance (peak current, peak to valley current ratio and valley width) improves as the spacer layer thickness increases for lattice matched AlGaAs/GaAs RTDs because of reduced ionized impurity scattering in the tunneling region of the diode, and it does not show any further improvement once the layer thickness is greater than a certain critical value. This is due to the formation of a spacer barrier which reduces the number of carriers available for the conduction process.

Spacer layers on pseudomorphic AlGaAs/InGaAs RTDs produce quite different features when the lowest allowed state in the well lies below the spacer barrier height. A thick spacer layer at the leading edge of the diode forms an accumulation layer while one at the trailing edge acts as an effective tunnel barrier. Pseudomorphic AlGaAs/InGaAs RTDs

with asymmetric spacer layer thicknesses provide very strong evidence that the spacer layer is playing a different role which depends on the bias configuration. Tunnel injection is through the ground state of the InGaAs well when the thick spacer layer is located at the leading edge of the device while it is through the first excited state of the InGaAs well when the thick spacer layer is at the trailing edge of the diode. Evidence is also provided which suggests that silicon impurity outdiffusion occurs during MBE growth.

RTDs subjected to a strong magnetic field exhibit magneto-quantum assisted tunneling features which become larger with increasing applied magnetic field. These features are distinguished between phonon assisted tunneling or successive Landau level tunneling by the peak position dependence on the magnetic field, as well as by Shubnikov-de Haas oscillations obtained from the RTDs.

Effect of Structural Parameters on Resonant Tunneling Diode Performance

by
Hyungmo Yoo

A THESIS
Submitted to
Oregon State University

in partial fulfillment of
the degree requirements for the
degree of

Doctor of Philosophy

Completed May, 11 1990
Commencement June, 1991

APPROVED:

Redacted for privacy

Professor of Electrical and Computer Engineering in Charge of Major

Redacted for privacy

Head of Department, Electrical and Computer Engineering

Redacted for privacy

Dean of the Graduate School

Date thesis is presented May, 11, 1990

Typed by researcher for Hyungmo Yoo

ACKNOWLEDGEMENT

I would like to thank the numerous individuals who contributed to the completion of the manuscript. First and foremost, I am indebted to my adviser, Dr. J.R. Arthur for his encouragement during the course of this work. I would also like to thank the members of my committee. In particular, I would like to express my gratitude to Dr. S.M. Goodnick for close consultation and cooperation with regard to various aspects of this work. I would like to express my gratitude as well to Dr. J.F. Wager for his valuable comments and advice with regard to this thesis.

The research presented in this dissertation came about through the friendship with Leon Ungier, Dr. J.T. Ebner, R.T. Kollipara, and J.E. Lary. Also, I am grateful to S.B. Kim for deposition of the plasma enhanced chemical vapor deposition (PECVD) oxide. I also would like to express my special gratitude to my wife Jeongsoo and son Byungoh as well as our family back in Korea for their patience and understanding.

TABLE OF CONTENTS

1.	Introduction	1
2.	Theory and Review	9
	2.1 Energy Quantization	9
	2.2 Basic Concepts of Tunneling	12
	2.3 Solution of Schrodinger's Equation	14
	2.4 I-V Characteristics	20
	2.5 Self-Consistent Approach	23
	2.5.1 Normalization of Wavefunction	25
	2.5.2 Implementation of Boundary Conditions	27
	2.5.3 Solution of the Self-consistent Model	32
	2.6 Device Applications	33
3.	Experimental Technique	38
	3.1 Molecular Beam Epitaxy	38
	3.1.1 GaAs	39
	3.1.2 AlAs and AlGaAs	40
	3.1.3 Pseudomorphic InGaAs	42
	3.1.4 Dopant	43
	3.1.5 RTD Growth	44
	3.2 Device Fabrication	47
	3.3 Current-Voltage Characteristics	49
	3.4 High Field Mageto-Transport	49
4.	Experimental Results and Analysis I	56
	4.1 Lattice-Matched AlAs/GaAs RTD	56
	4.1.1 I-V Characteristics	57
	4.1.2 Shubnikov-de Haas Measurement	63
	4.2 Pseudomorphic $Al_{0.4}Ga_{0.6}As/In_{0.1}Ga_{0.9}As$ RTD	67
	4.2.1 I-V Characteristics	67
	4.2.2 Shubnikov-de Haas Measurement	72
5.	Experimental Results and Analysis II	74
	5.1 Analysis of the Spacer Layer	74
	5.2 Lattice Matched RTD	78
	5.2.1 I-V Characteristics	78
	5.2.2 Magnetic Field Analysis	83
	5.3 Pseudomorphic RTDs	92
	5.4 Pseudomorphic RTDs with Asymmetric Spacer	95
	5.4.1 The 50/500 RTD	97
	5.4.2 The 500/50 RTD	100
	5.4.3 Magnetic Field Study	104
6.	Summary and Conclusions	110
	Bibliography	114

LIST OF FIGURES

		<u>Page</u>
1.1	(a) Conduction band diagram of resonant tunneling diode. (b) Electron tunneling probability through the RTD as a function of electron energy.	3
2.1	Allowed energy bands (dotted area), E_1 , E_2 and E_3 calculated as a function of well or barrier width, w , in a finite period superlattice.	11
2.2	Tunneling probability of electrons through a superlattice period of (a) four, (b) three and (c) two.	13
2.3	Double barrier structure (a) at thermal equilibrium and (b) under bias. T_l and T_r are tunneling probabilities of the left and the right barrier, respectively. w_i 's and k_i 's represent width of the barrier and $k_i = \sqrt{2m^*(V_i - E)}/\hbar$.	15
2.4	(a) Arbitrary tunneling barrier of a finite length is segmented into N regions. Each region is approximated with a constant potential and effective mass. (b) i th interface. a_l and b_l are amplitudes of the incident and reflected flux from the left whereas a_r and b_r are those from the right, respectively.	18
2.5	A typical I-V characteristics of a RTD measured at 77 K (solid line) and calculated from Tsu and Esaki's model.	22
2.6	RTD under bias. (a) Tsu and Esaki's model. A linear voltage drop between the two barriers was assumed so resonant tunneling occurs at $qV_{bias} = 2E_0$. (b) The modified model which accounts for charge accumulation in accumulation layer adjacent to the emitter tunnel barrier as well as in the well. Resonant tunneling occurs at $qV_{bias} > 2E_0$.	24
2.7	Solid line in the figure shows a conduction band profile at zero bias and singly broken line represents a carrier concentration $n(z)$. Doubly broken line depicts magnified $n(z)$ away from the tunnel barrier.	26
2.8	RTD is segmented into three regions to include scattering and diffusion in a heavily doped contact region. Region I and III are classical regimes and region II is a QM regime.	28

2.9	RTD under bias V_a . The solid line in the figure is the CB profile and dotted line is a carrier concentration, $n(z)$ obtained from the new boundary condition. The solid line in the well is $n(z)$ magnified.	31
2.10	I-V characteristics obtained from four different self-consistent approaches. Solid line: Cahay <i>et al.</i> , broken line: Landheer <i>et al.</i> , dotted line: Ohnishi <i>et al.</i> , and dash and dot line: present work.	34
2.11	Resonant tunneling transistor (RTT) proposed by Capasso <i>et al.</i> (a) RTT at thermal equilibrium. (b) RTT biased for ground energy level tunneling. (c) RTT biased for the first excited state tunneling.	37
3.1	Photoluminescence (PL) of i-GaAs epi-film grown by MBE at different substrate temperature. Substrate temperatures are (a) 500 C, (b) 550 C, (c) 600 C, and (d) 650C. PL intensity in (a) is magnified 4 times. The peaks at ~ 8355 and 8255 Å are due to transitions associated with carbon and exciton, respectively.	41
3.2	RTD structures used in present work. (a) The CB profile of metallurgical junction. (b) Vertical structures.	45
3.3	(a) Side view of RTD after final processing. (b) The final metalization mask. The numbers in the figure represent lateral device dimensions in micrometers.	48
3.4	Experimental setup for I-V characteristic measurements.	50
3.5	Conduction band profile under the influence of a quantizing magneticfield. Magnetic field is assumed to be normal to the barrier ($B \parallel J$). The energy levels denoted by the dotted and the solid lines are with and without magnetic field, respectively.	53
3.6	Experimental setup for Shubnikov-de Haas type measurements.	55
4.1	AlAs/GaAs RTD. (a) Conduction band Profile. (b) I-V characteristics measured at RT, 77K, and 1.8K.	58
4.2	I-V characteristics of the AsAs/GaAs RTD at 1.8 K. The solid and the dashed lines are for $B = 8$ Tesla ($B \parallel J$) and 0 field, respectively. The additional curves show the valley region of the I-V curve at different magnetic fields ($B \parallel J$).	60

- 4.3 Evolution of the magneto-quantum peaks as a function of applied magnetic field ($B \parallel J$). The squares and triangles correspond to the maximum and minimum of the magneto-quantum peaks, respectively. The inset figure is a plot of the slope of a least square fit as a function of Landau level index. 62
- 4.4 (a) Differential conductance of the AlAs/GaAs RTD as a function of magnetic field ($B \parallel J$). The inset figures are the magnified differential conductance at low magnetic field. (b) The lower series of magneto-quantum oscillation periods as a function of bias. 65
- 4.5 Pseudomorphic $\text{Al}_{0.4}\text{Ga}_{0.6}\text{As}/\text{In}_{0.1}\text{Ga}_{0.9}\text{As}$ RTD. (a) Conduction band profile. (b) I-V characteristics measured at 250, 150, 77, and 1.7 K. 68
- 4.6 I-V characteristics of the pseudomorphic $\text{Al}_{0.4}\text{Ga}_{0.6}\text{As}/\text{In}_{0.1}\text{Ga}_{0.9}\text{As}$ RTD at 1.8 K. The solid and the dashed lines are for $B = 8$ Tesla ($B \parallel J$) and 0 field, respectively. The inset figure shows ΔV_p as a function of magnetic field. $\Delta V_p = V_p(B) - V_p(B=0)$. 70
- 4.7 Differential conductance of the pseudomorphic $\text{Al}_{0.4}\text{Ga}_{0.6}\text{As}/\text{In}_{0.1}\text{Ga}_{0.9}\text{As}$ RTD as a function of magnetic field ($B \parallel J$) at $V_{\text{bias}} = 0.90, 0.95$ and 1.0 V. 73
- 5.1 Analysis of the spacer layer. (a) $n^+ - n^-$ homojunction. (b) Spacer barrier height, dE_s in an $n^+ - n^- - n^+$ homojunction. 75
- 5.2 I-V characteristic of lattice matched AlAs/GaAs RTDs with 50, 500 and 1000 Å thick spacer layers measured at 77 K. The solid and dashed lines in the left inset signifies the CB profile at thermal equilibrium and metallurgical junction respectively. The right inset figure shows a two step conduction process for electrons with below spacer barrier height energy dE_s . 79
- 5.3 Normalized I-V characteristics of the lattice matched AlGaAs/GaAs RTDs. The I-V curves are normalized in a way that the peak voltage and the peak current of all RTDs are aligned at one point. 82
- 5.4 Influence of the magnetic field on lattice matched AlGaAs/GaAs RTD with 500 Å thick spacer layer. (a) I-V characteristics measured at 1.8 K with ($B = 8.7$ T) and without magnetic field ($B \parallel J$). The inset figure shows magnified I-V curves in the valley region with different magnetic fields. (b) Change of the second satellite peak position in (a) as a function of magnetic field. The straight line is a result of a least-squares fit. 84

- 5.5 Density of states under quantizing a magnetic field. The dashed line represents a density of states in the absence of a magnetic field. 86
- 5.6 (a) I-V characteristics of the AlGaAs/GaAs RTD with a 1000 Å spacer layer measured at 1.8 K with magnetic field $B = 8.7$ Tesla ($B \parallel J$). Inset figure shows the second satellite peak position as a function of magnetic field shown in (b). (b) Differential conductance of the RTD in the valley region of the I-V curve with magnetic field. 88
- 5.7 (a) Shubnikov-de Haas oscillations obtained from the AlGaAs/GaAs RTD with a 500 Å thick spacer layer. Numbers in the figure represent the applied bias. (b) SdH oscillation period, B_f , as a function of applied bias. $B_f = [\Delta(1/B)]^{-1}$. 90
- 5.8 I-V characteristics of a pseudomorphic Al_{0.35}Ga_{0.65}As/In_{0.2}Ga_{0.8}As RTDs with 50, 100 and 250 Å thick spacer layers measured at 77 K. I-V curves of the pm-RTD with 250 Å thick spacer layer is magnified by 20 times. The inset figure is a calculated CB profile at thermal equilibrium. 93
- 5.9 I-V characteristics of (a) pm-Al_{0.35}Ga_{0.65}As/In_{0.2}Ga_{0.8}As RTD and (b) the lattice matched Al_{0.35}Ga_{0.65}As/GaAs RTD with 50 Å thick spacer layers measured at 77 (dashed line) and 1.8 K (solid line). 96
- 5.10 I-V characteristics of the 50/500 RTD measured at 77 and 1.8 K. The right and the left inset figures show the as-grown metallurgical CB edge and CB edge at thermal equilibrium, respectively. 98
- 5.11 Peak voltage position of the pm-Al_{0.35}Ga_{0.65}As/In_{0.1}Ga_{0.9}As RTD with symmetric 35, 50, 100, 250, 500 Å thick spacer layers measured at 77 K. 101
- 5.12 I-V characteristics of the 500/50 RTD measured at 1.8 K. The dotted curve in the figure is that of the 50/500 RTD with I(-V). Inset figure shows the CB profile at thermal equilibrium. 102
- 5.13 Shubnikov-de Haas oscillations of the (a) 500/50 and (b) 50/500 RTDs 105
- 5.14 (a) SdH oscillation period of the 500/50 and 50/500 RTD as a function of applied bias. The right ordinate shows a two-dimensional carrier density with the corresponding B_f . (b) Forward I-V characteristics of the 500/50 RTD measured at 1.8 K with $B = 8.7$ Tesla and 0 field. The peak marked as L0 is a L0 phonon assisted tunneling feature. 107

Effect of Structural Parameters on Resonant Tunneling Diode Performance

1. Introduction

The objectives of the present research are to develop an understanding and to improve the performance of resonant tunneling diodes (RTDs) by means of a study of structural parameters on both lattice matched and pseudomorphic AlGaAs/InGaAs RTDs. The effect of structural parameters on RTD performance, e.g. the influence of the spacer layer thickness and the presence of an InGaAs layer in the well, is currently not well understood. Realization of these devices is now possible as a result of recent advances in semiconductor fabrication techniques.

Considerable progress has been made in the fabrication of compound semiconductor devices over the past decades through advances in epitaxial growth technology. These techniques have made possible what is sometimes described as "band gap engineering" in which growth of different band gap semiconductor materials is accomplished in a single monocrystalline device. Band gap engineered heterojunction devices are the result of crystal growth techniques such as molecular beam epitaxy (MBE) and metal organic chemical vapor deposition (MOCVD). These techniques make possible the growth of structures composed of different semiconductor materials with layer thicknesses precisely controlled to within a few angstroms. As the device dimensions are reduced, quantum mechanical phenomena, which do not have classical analogies, become increasingly important. One such device which depends

explicitly on quantum interference phenomena is the RTD whose transport properties were first investigated by Tsu and Esaki [1].

The active region of an RTD consists of a double barrier structure with a lower bandgap material (well) such as GaAs sandwiched between two higher bandgap materials (barriers) such as AlGaAs, with heavily doped contact regions on either side of the structure, as shown in Fig. 1.1 (a). If the width of the well is comparable to the carrier de Broglie wavelength (typically 100 Å to 1000 Å), the conduction band in the well is separated into a series of subbands and the carriers in the well are confined to characteristic resonant energy levels. Thus, carriers with energy coincident with one of the subband energy (or resonant energy) levels in the well can propagate through the structure without attenuation. This transport mechanism is known as resonant tunneling. The probability of carrier tunneling (ratio of incident to outgoing flux) through the structure as a function of energy exhibits highly resonant behavior as shown in Fig. 1.1 (b). Carrier tunneling becomes discernible indirectly by applying a bias across the device. As the applied bias increases, the subband energy (resonant energy) in the well is aligned with the Fermi energy (E_F) in the heavily doped contact region and carriers can tunnel through the double barrier structure resonantly via the resonant state in the well. As the bias is increased further, the resonant energy in the well becomes misaligned with the Fermi energy of the emitter contact layer and the tunneling probability through the device drops sharply as does the current. The resulting negative differential resistance (NDR) is a useful phenomenon for producing both amplification and oscillation.

Tsu and Esaki [1] assumed coherent resonant tunneling of

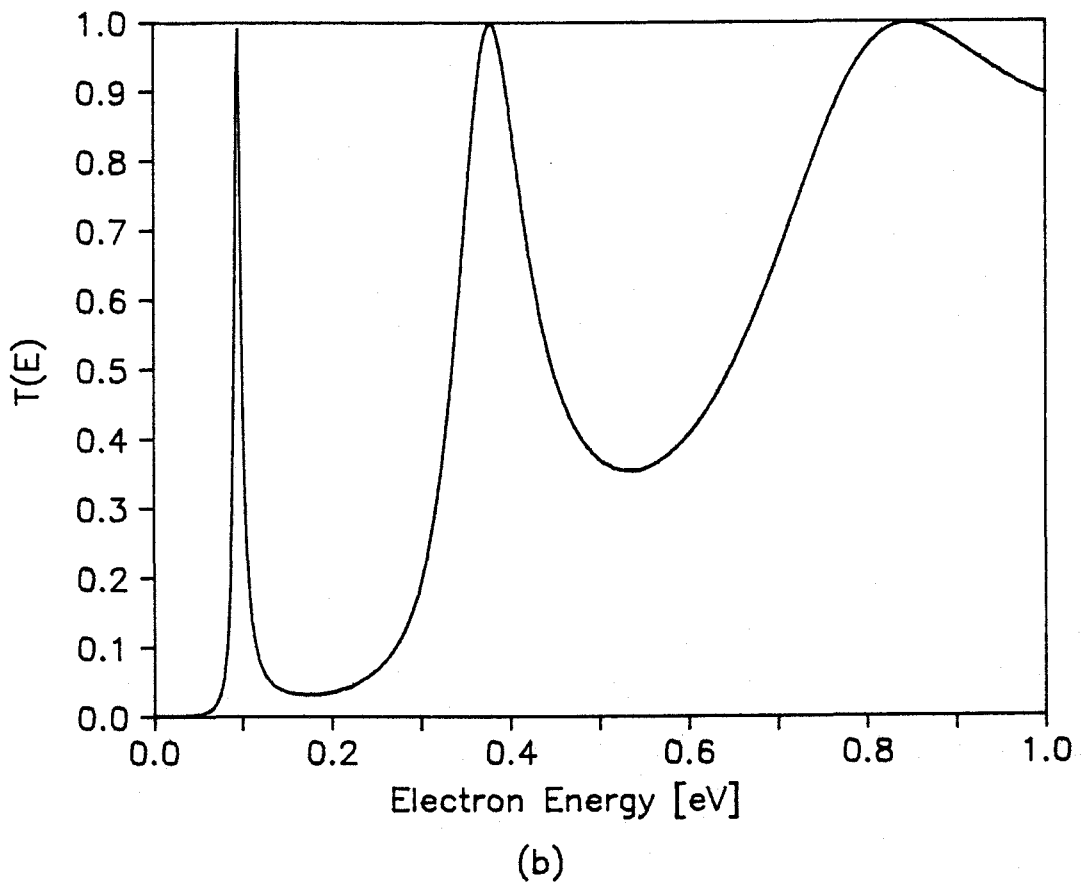
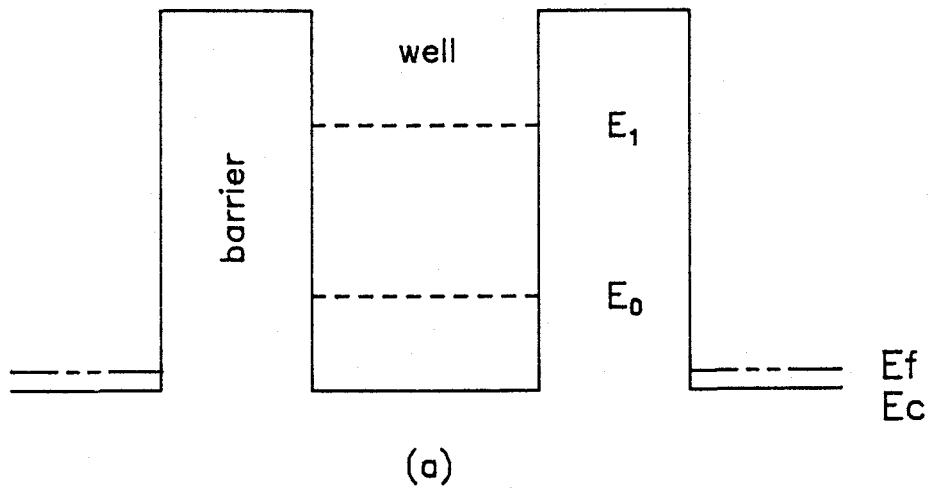


Figure 1.1: (a) Conduction band diagram of a resonant tunneling diode. (b) Electron tunneling probability through the RTD as a function of electron energy.

electrons through the double barrier structure. Coherent resonant tunneling is a direct result of the wave nature of electrons. Electrons from one side of double barrier structure may propagate to the other side of the contact by undergoing multiple reflections between the two potential barriers. If the spacing between potential barriers is an integer multiple of the incident electron half wavelength, the amplitude of the wave function in the well interferes constructively [2]. In their model, it is assumed that scattering is infrequent, so that the phase of an electron remains coherent for the entire time of transit. If inelastic scattering is involved in the process, phase coherence, which is needed for constructive interference, is destroyed. Without coherence, the wave function within the well would not build up and the probability of transmission through the double barrier region would be greatly reduced. This phenomenon can be easily understood from the optical analogy of the Fabry-Perot cavity which shows unity transmission at particular resonant frequencies [2]. The model proposed by Tsu and Esaki was generally accepted until being challenged by Luryi [3] who was the first to question this assumption, proposing an alternative mechanism, viz, sequential tunneling. If in the course of multiple reflection, an electron suffers a scattering event, the wavefunction phase will be randomized. Therefore, scattering events destroy the coherence needed for constructive interference in the Fabry-Perot effect. Without coherence, the wave function amplitude in the well will not be enhanced. However, tunneling will still occur in a sequential fashion, and negative differential resistance, dependent only upon lateral momentum and energy conservation considerations, will still be observed. The question of whether resonant or sequential

tunneling is the dominant transport mechanism, was resolved by Capasso *et al.* [4] followed by Stone and Lee's [5] work of resonant tunneling through an impurity center. To achieve the coherent resonant enhancement of transmission (Fabry-Perot effect), a finite time τ_0 is required to build up the steady state resonant probability density in the well. If the scattering time τ is much shorter than τ_0 , the peak transmission at resonance is reduced by $\tau_0/(\tau+\tau_0)$. The scattering time τ is the reciprocal of the total scattering rate including elastic and inelastic scattering. The ratio of the number of electrons that resonantly tunnel without experiencing collisions to the number that tunnel after undergoing collisions is equal to τ/τ_0 . If the intrinsic tunneling time τ_0 exceeds or equals the scattering time τ , coherent resonant tunneling is observable, otherwise electrons will tunnel incoherently (or sequentially) without resonant enhancement and with reduced peak transmission.

The first experimental evidence of NDR from this device, based on AlGaAs barriers and a GaAs well, was reported by Chang *et al.* [6] in 1974 at a temperature below 77 K. However, not much progress was made for a decade due to technical problems related to crystal growth. During that period, a new crystal growth technique called molecular beam epitaxy made remarkable progress after the pioneering work of Cho and Arthur [7]. In 1983, Sollner *et al.* [8] revived interest in the RTD by demonstrating the feasibility of high speed device applications. They showed a large NDR region in the current-voltage characteristics of an AlGaAs/GaAs RTD grown by MBE with a peak to valley current ratio (PVCR) of 6:1 at 25 K. They also demonstrated the RTD as a detector and mixer of far infrared radiation at 2.5 THz, indicating the potential

for high frequency applications. One year later, Sollner *et al.* reported the first oscillations generated by a resonant tunneling diode, with a power output of $5 \mu\text{W}$ at frequencies up to 18 GHz [9].

More recently, Broekaert *et al.* reported PVCRs of 30:1 at 300 K and 63:1 at 300 and 77 K from RTDs consisting of $\text{In}_{.52}\text{Al}_{.48}\text{As}$ barriers and a $\text{In}_{.53}\text{Ga}_{.47}\text{As}$ well, lattice matched on an InP substrate [10]. RTDs from lattice matched $\text{In}_{.52}\text{Al}_{.48}\text{As}/\text{In}_{.53}\text{Ga}_{.47}\text{As}$ layers on an InP substrate display better performance (PVCr) than when AlGaAs/GaAs layers on a GaAs substrate are employed since the former has a smaller electron effective mass than the latter. RTDs based on the AlGaAs/GaAs material system usually contain an AlAs concentration of more than 30 % in the AlGaAs barriers in order to provide a reasonable band offset between the barriers and the well and thus suppress thermionic current. As the AlAs concentration in AlGaAs increases to more than 30 %, the Γ , X and L bands start to overlap and an indirect band gap develops at an AlAs concentration above 45 %. Increasing the AlAs concentration also increases the rate of inter-valley scattering. However, the detailed band structure of $\text{In}_{.52}\text{Al}_{.48}\text{As}$ and $\text{In}_{.53}\text{Ga}_{.47}\text{As}$ are not well known, and RTDs using the $\text{In}_{.52}\text{Al}_{.48}\text{As}/\text{In}_{.53}\text{Ga}_{.47}\text{As}$ material system were not considered any further in the present work.

Success in the demonstration of resonant tunneling has stimulated a number of device studies. They have been mostly devoted to the phenomenological study of the device and not much work has been done to improve the performance of the RTD with regard to such parameters as the PVCr and the valley width (W_v). A high quality RTD implies a higher PVCr and W_v since high values of these parameters are necessary for device applications such as oscillators, mixers and amplifiers.

Improved performance of devices to date has been partially due to a better understanding of the device physics. However, improvements are mostly due to advances in crystal growth techniques. One of the best ways to improve the RTD performance is to increase the ratio of the coherent resonant to incoherent resonant (sequential) tunneling, which can be achieved by optimizing the device parameters and minimizing the carrier scattering [10-12]. One obvious method to suppress scattering within the device is to place an undoped GaAs layers (referred to as a spacer layer) adjacent to the tunnel barrier to reduce ionized impurity scattering [13]. The principal effect of scattering in the active region of the device is to decrease the peak transmission and broaden the energy levels which degrades the RTD performance by reducing the peak to valley current ratio (PVCR).

The RTDs fabricated by numerous groups contain spacer layers with thickness ranging from 0 Å to 1000 Å. However, the role of the spacer layer on RTD performance has not been systematically studied. Most theoretical models have also neglected the effect of spacer layers [14,15]. It is generally believed that a thick spacer layer improves the PVCR by reducing ionized impurity scattering; however, the performance of RTDs based on the lattice matched $\text{Al}_x\text{Ga}_{1-x}\text{As}/\text{GaAs}$ system degrades for spacer layers greater than a certain critical width as shown by the present work. Spacer layers based on pseudomorphic $\text{Al}_x\text{Ga}_{1-x}\text{As}/\text{In}_y\text{Ga}_{1-y}\text{As}$ RTDs produce dramatic differences compared to $\text{AlGaAs}/\text{GaAs}$ RTDs due to the relative position of the quasi-bound state in the well [16]. The influence of the spacer layer on lattice matched and pseudomorphic $\text{AlGaAs}/\text{InGaAs}$ RTDs is discussed in detail later of this thesis.

An overview of the thesis is as follows: A review of carrier quantization due to the periodicity of the crystal potential and tunneling through the structure is given in chapter 2. In addition to reviewing transport mechanisms through the RTD, two proposed novel device applications, one for two and one for three terminal devices, are also presented since they aid in understanding carrier transport through the device. Experimental efforts to build and test the RTDs used in this research, e.g. molecular beam epitaxial growth, device fabrication and device characterization techniques, are discussed in chapter 3. Analysis of two typical device structures, lattice matched and pseudomorphic RTDs, by electric and magnetic field measurements are discussed in chapter 4. Influence of spacer layer on both lattice matched and pseudomorphic RTDs are presented in chapter 5. Finally, the work accomplished in this research is summarized in chapter 6.

2. Theory and Review

The theoretical basis for the RTD is fairly well established, however the fit between theory and experiment is still poor. The main purpose of the present chapter is to develop the understanding of transport in resonant tunneling diodes. This chapter begins with a quantum mechanical (QM) description of carrier quantization due to the periodic crystal potential. This introduction provides the necessary background for discussion of carrier transport through the double barriers. Discussions in the remaining chapters are focused on a superlattice with two periods, *i.e.* double barriers, and carrier transport through these barriers. Two novel devices utilizing QM phenomena, which do not have a classical analogy are presented in section 2.6 of this chapter.

2.1 Energy Quantization

It is well known that the periodicity of the crystal potential gives rise to allowed and forbidden energy bands in a semiconductor. The exact calculations of real band structures are exceedingly difficult; consequently, various approximate calculations have been developed. Here we consider a simplified band model, the Kronig-Penney model, which enables one to develop the essential features of electron behavior in solids [17]. According to the Kronig-Penny model, the periodicity of material layers in a superlattice (SL) also results in energy quantization. The effect of an infinite period SL is a formation

of conduction minibands and nearly all energies in each band are allowed. The allowed subbands in a SL can be calculated from the following expression, assuming a one dimensional, periodic square well potential [18]:

$$\begin{aligned}
 -1 \leq \cos \left[\frac{a\sqrt{2m^*E}}{\hbar} \right] \cosh \left[\frac{b\sqrt{2m^*(V-E)}}{\hbar} \right] \\
 + \left[\frac{V}{2E} - 1 \right] \frac{1}{\sqrt{V-E-I}} \sin \left[\frac{a\sqrt{2m^*E}}{\hbar} \right] \sinh \left[\frac{b\sqrt{2m^*(V-E)}}{\hbar} \right] \leq 1 \quad (2.1)
 \end{aligned}$$

where E is the electron energy in the SL direction, V is the barrier height, a is the well width, b is the barrier width, and m^* is the effective mass of the carriers. Energy bands for an infinite SL of period with $a = b = 50 \text{ \AA}$ and a barrier height of $V = 0.4 \text{ eV}$ are shown in Figure 2.1. The cross-hatched regions in the figure are the allowed energy bands. E_0 , E_1 , and E_2 represent the ground, the first and the second excited energy states, respectively.

Figure 2.2 is a schematic representation of the effect of decreasing the number of SL periods. Vezzetti *et al.* [19] has shown that for a finite SL of N periods, there are $N-1$ energies in each band for which the Bloch wavenumber has N values, yielding $N-1$ resonant energies for each energy band. As the number of SL periods decreases, energy selection becomes sharper since the allowed energy in each bands is reduced. For a quadruple barrier (SL period of four), the range of Bloch wave numbers is segmented into four intervals, yielding three allowed energies in each of the energy bands. The probability of carriers from one side of the SL reaching the other side (the tunneling probability) is unity when the energies of the incident carriers match with the allowed energies. Thus the tunneling probability, $T(E)$ via a

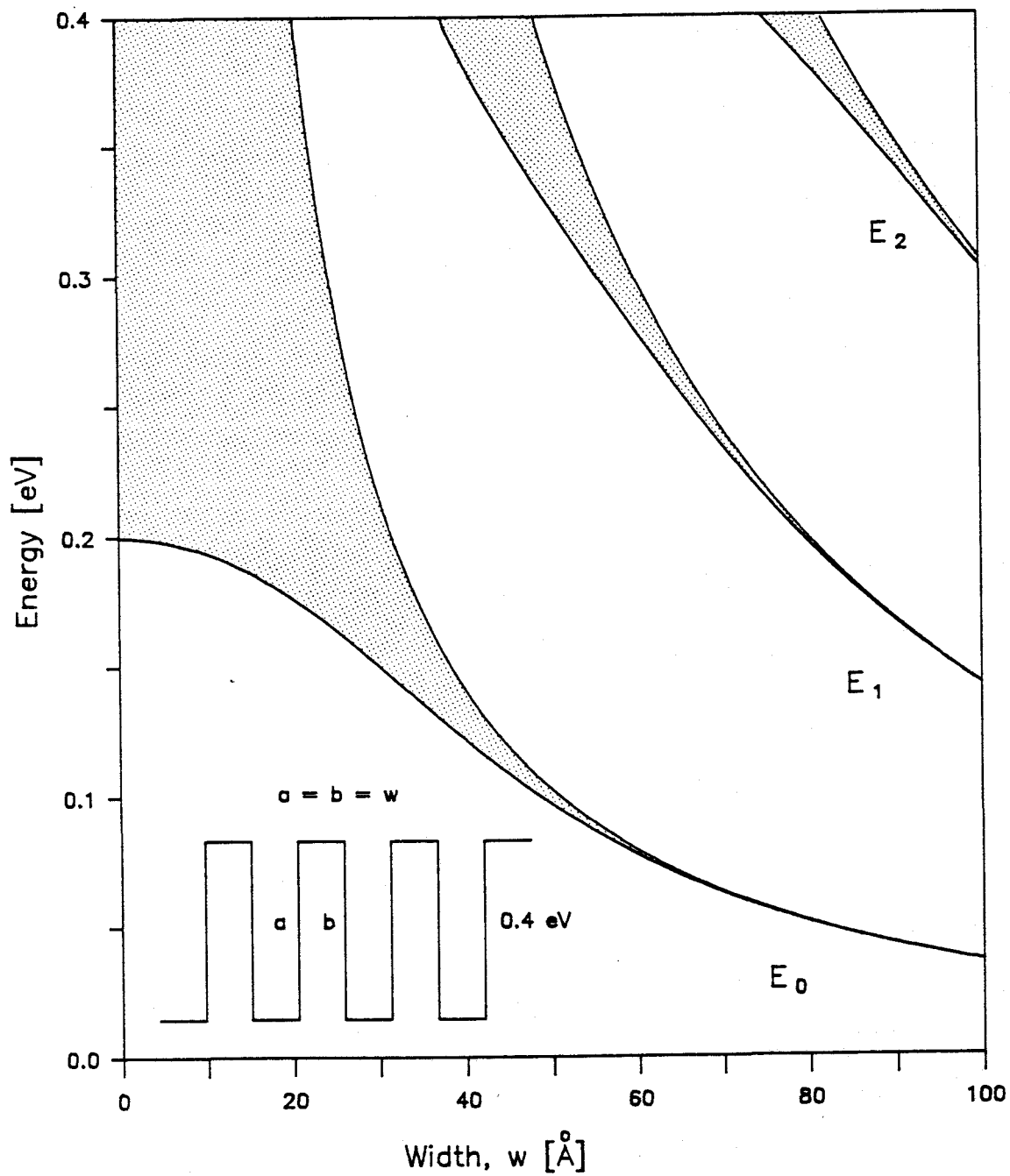


Figure 2.1: Allowed energy bands, E_1 , E_2 and E_3 (dotted area) calculated as a function of well or barrier width, w , in a finite period superlattice.

quadruple barrier shows three unity transmission peaks corresponding to three allowed energies in each allowed state as shown in Figure 2.2 (a). Transmission through a triple barrier as a function of incident carrier energy accordingly shows a doublet as in Figure 2.2 (b). The allowed energy in a SL with a period of two (double barrier) finally becomes a singlet and shows a single unity transmission peak in each band as shown in Figure 2.2 (c).

2.2 Basic Concepts of Tunneling

The tunneling probability through a rectangular barrier as shown in Figure 2.3 (a) was analytically derived by Kane [20] and is repeated here because it provides a physical insight into the name of resonant tunneling. The global transmission rate T , the fraction of incident flux going through the structure, is

$$T = \frac{C_0 T_1 T_r}{C_1 (T_1 T_r)^2 + C_2 T_1^2 + C_3 T_r^2 + C_4} \quad (2.3)$$

where the C_i are numbers of the order of 1, slowly varying with the energy of the incident particles. T_1 and T_r are usually very small and represent transmission probabilities of the left and the right barrier, respectively. The coefficient C_4 vanishes if $k_2 w_2 = k_4 w_4$ and the global transmission becomes $T = T_{\min}/T_{\max}$, where T_{\max} and T_{\min} are the greater and smaller of the transmission T_1 and T_r of left and right barriers, respectively [15]. Thus the transmission of the left and right barriers must be equal at all quasi-eigenstate energies to achieve near unity transmission. Whereas if $C_4 \neq 0$, sequential tunneling is expected and

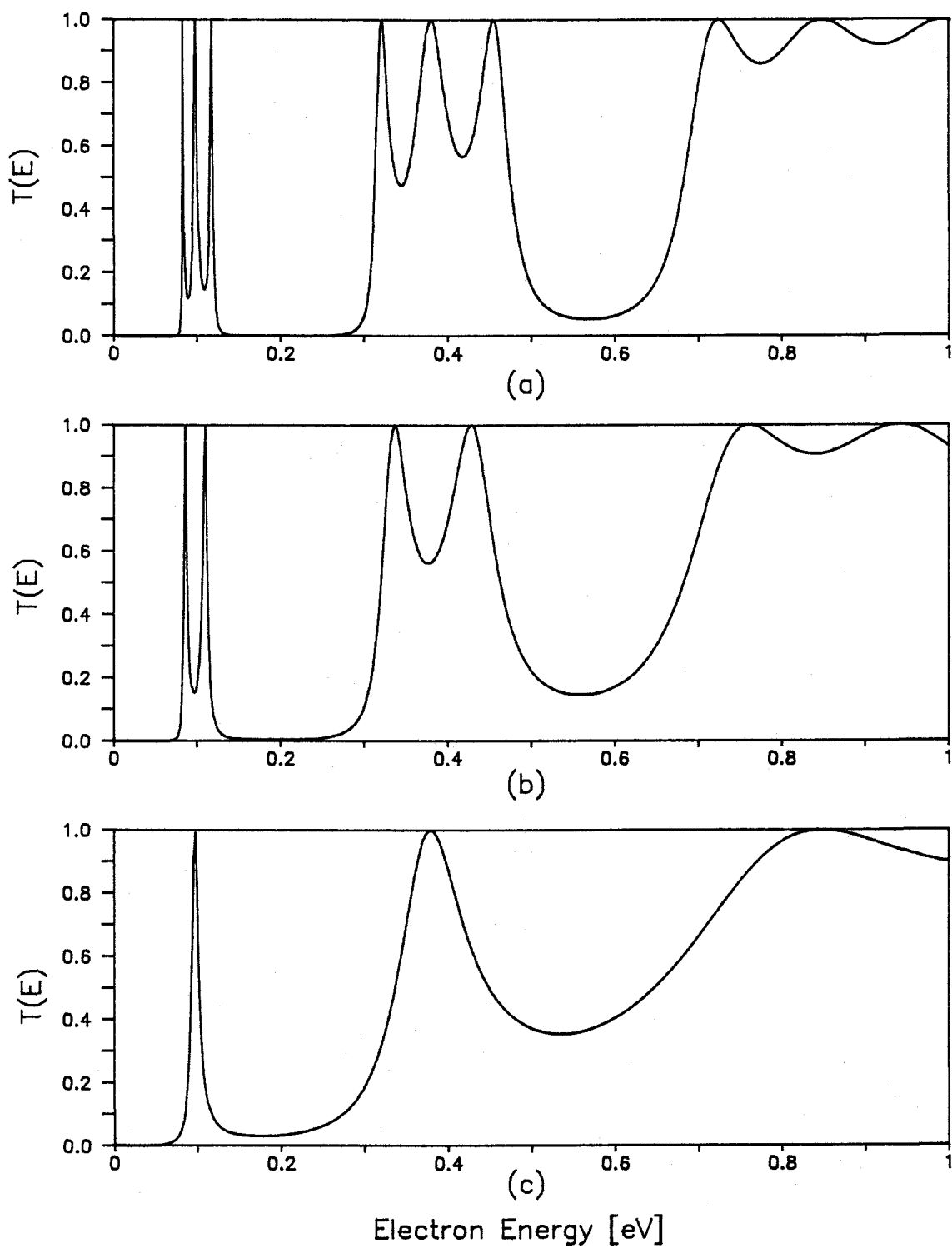


Figure 2.2: Tunneling probability of electrons through a superlattice period of (a) four, (b) three, and (c) two.

the global transmission is of the order of $T_l T_r = T_{\max} T_{\min}$ because both barriers add their effect independently. The condition for unity transmission, $T_l = T_r$ is hardly achievable in a symmetric barrier configuration under bias since T_l usually is bigger than T_r as shown in Figure 2.3 (b). However, this is possible by designing asymmetric barriers, that is, one barrier is much thicker or higher than the other barrier. Then the condition, $T_l = T_r$ is achieved in one direction at a cost of poorer performance in the other bias direction due to extreme asymmetry [10].

The analytical description of resonant tunneling described above provides physical insight; however, the formula developed above is difficult to implement directly into an arbitrary shaped potential profile of a finite length. A systematic solution of the tunneling probability for such a case has been developed by numerous authors [15,21]. All of them lead to the same tunneling probability and the basics of the algorithm are the same: solve Schrodinger's equation in the effective mass approximation with appropriate boundary conditions and propagate the solution across the entire structure. One of the algorithms which describes a transmission of a mono-energetic flow of carriers through a random barrier is discussed in the following section.

2.3 Solution of Schrodinger's Equation

Schrodinger's equation in the effective mass approximation is

$$\frac{\partial}{\partial z} \left[\frac{m(0)}{m(z)} \frac{d\psi(z)}{dz} \right] + \frac{2m(0)}{\hbar^2} \left[E_z - E(z) + E_t \left(1 - \frac{m(0)}{m(z)} \right) \right] \psi(z) = 0 \quad (2.4)$$

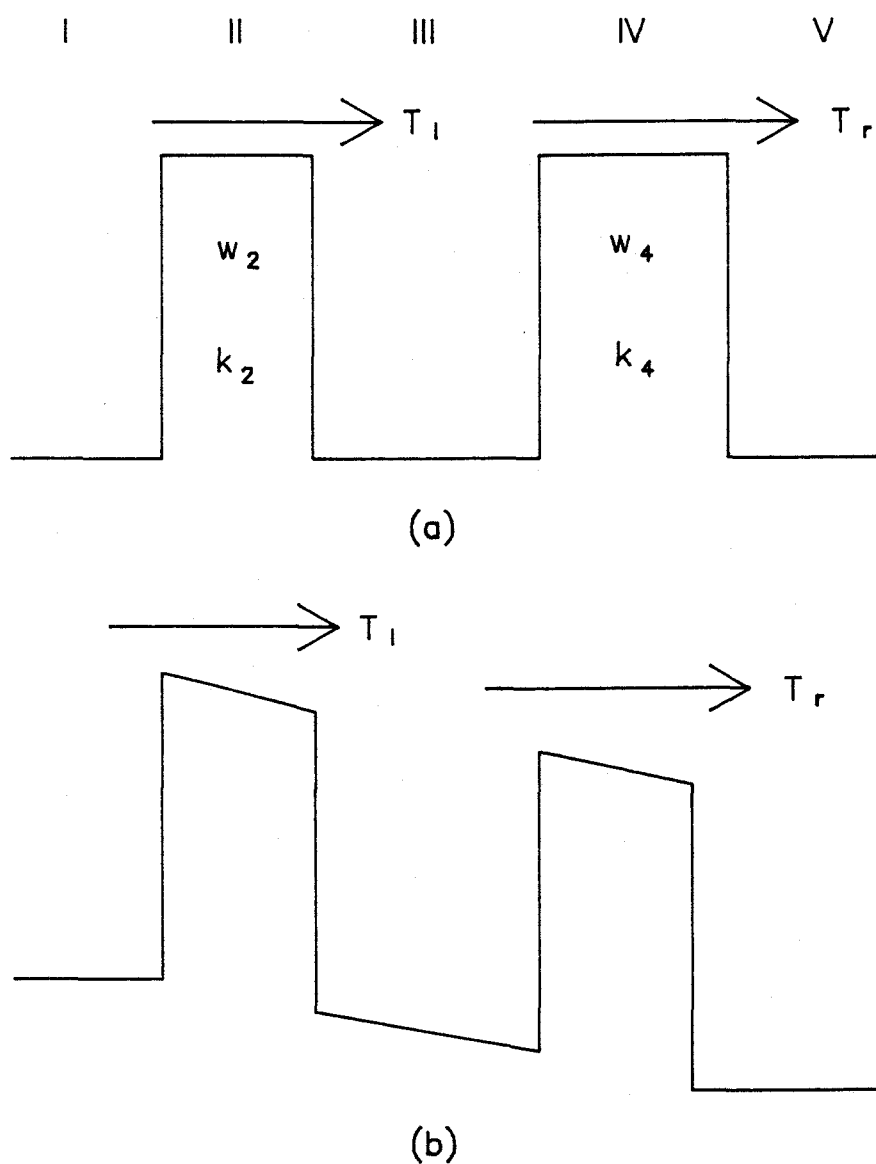


Figure 2.3: Double barrier structure (a) at thermal equilibrium and (b) under bias. T_l and T_r are the tunneling probabilities of the left and the right barrier, respectively. w_i 's and k_i 's represent the width of the barrier and $k_i = \sqrt{2m^*(V_i - E)}/\hbar$.

where $E(z)$ is the energy of the conduction band (CB) edge, $m(z)$ is the effective mass at a position z , and E_t and E_z are the energy of carriers normal and parallel to a barrier direction, respectively. To reduce a quantum mechanical description of carrier transport to a level feasible for numerical calculations, a number of simplifications must be made. First, the material and doping density are assumed uniform in a plane transverse to the direction of electron propagation, thus the conduction band (CB) profile varies only in the growth direction. Second, the semiconductors are assumed to be n-type, so that electrons provide the dominant contribution to both carrier and current densities. Furthermore, holes and electron-hole interactions and electron-electron interactions are assumed to be unimportant, allowing for a single particle approach to transport. Third, an envelope function solution for the electron wavefunction is assumed to apply. The effect of the crystal potential is parameterized by the energy bands and electron effective mass, which change abruptly at material interfaces. Bastard and Brum [22] have demonstrated that this assumption is reasonable, because Bloch wavefunctions differ little from one material to another for the majority of lattice-matched heterostructures.

Finally, devices are assumed to be short, relative to an electron mean free path, so that scattering events are infrequent, and can be neglected. With regard to discussion of resonant tunneling in the introduction, this is a drastic simplification. The dwell time of a multiply reflected electron in a resonant tunneling diode could be much longer than the time between collisions. Presently, much work remains for the incorporation of scattering into the quantum transport theory.

Frenshley has studied Wigner functions which use the quantum Liouville equation to include scattering [23]. However, he reported some numerical instabilities when the time of simulation is large, and the boundary conditions are difficult to implement.

In order to solve Schrodinger's equation within the assumptions stated above in an arbitrary shaped potential with a finite length, the device is segmented into small intervals as shown in Figure 2.4. In each interval, it is assumed that the potential and effective mass are constant, then the solution of Schrodinger's equation is known analytically. Hence, the problem becomes one of matching solutions across the device at interval boundaries with appropriate boundary conditions. Current continuity is adopted as a boundary condition instead of momentum continuity [24]. Thus,

$$\frac{1}{\sqrt{m^*}} \psi_l(z) = \frac{1}{\sqrt{m^*}} \psi_r(z) \quad (2.5a)$$

$$\frac{1}{\sqrt{m^*}} \psi_l'(z) = \frac{1}{\sqrt{m^*}} \psi_r'(z) \quad (2.5b)$$

The wave function $\psi(z)$ which satisfies the Schrodinger's equation at each region is

$$\psi_1(z) = a_1 \exp(jk_1 z) + b_1 \exp(-jk_1 z) \quad (2.6a)$$

$$\psi_2(z) = a_2 \exp(jk_2 z) + b_2 \exp(-jk_2 z) \quad (2.6b)$$

$$\vdots$$

$$\psi_N(z) = a_N \exp(jk_N z) \quad (2.6c)$$

where a_i 's and b_i 's are incident and reflected amplitudes of the wave function. The subscript in Eqs. (2.6) represents region numbers shown

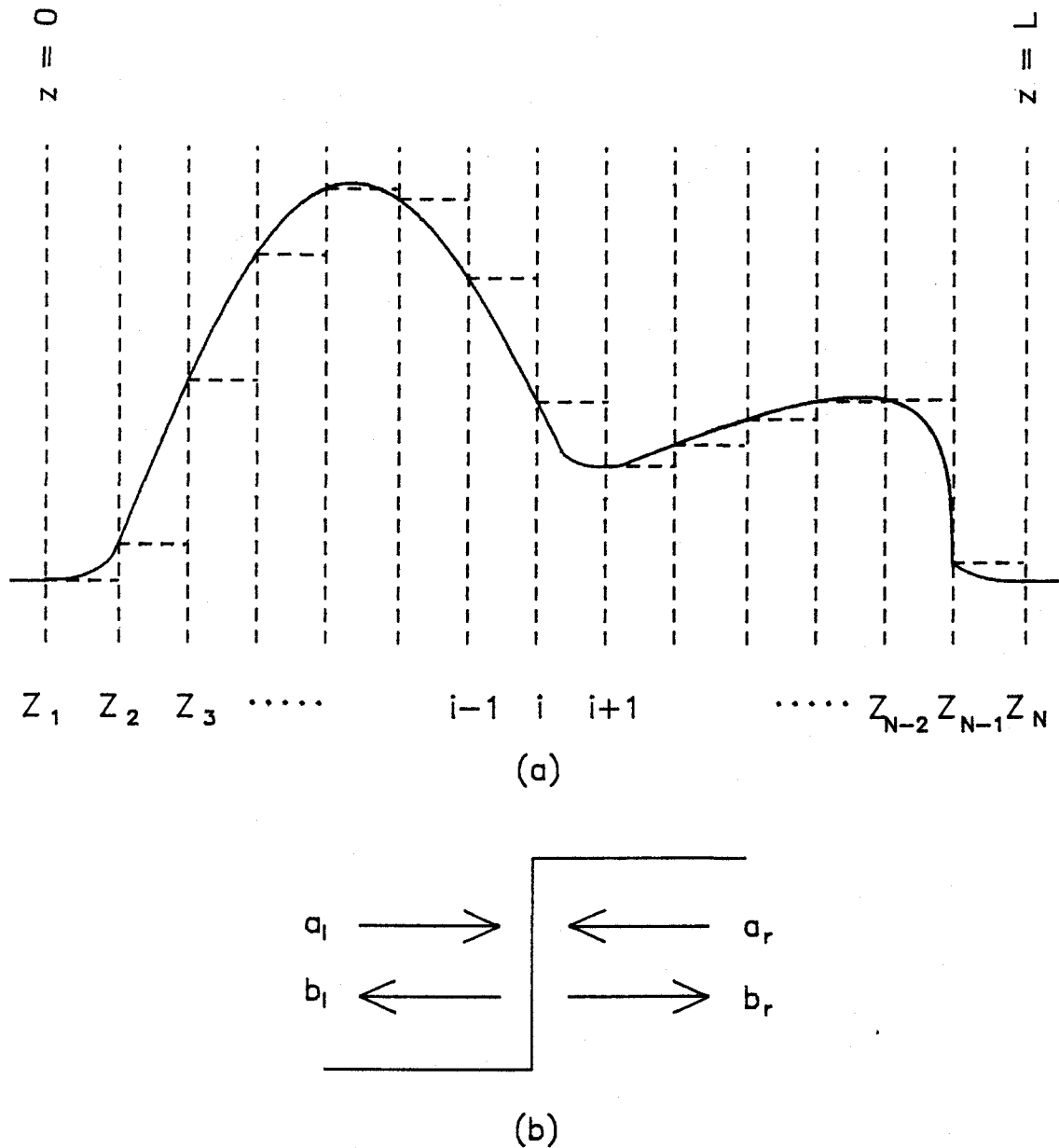


Figure 2.4: (a) Arbitrary tunneling barrier of a finite length is segmented into N regions. Each region is approximated with a constant potential and effective mass. (b) i th interface. a_l and b_l are amplitudes of the incident and reflected flux from the left whereas a_r and b_r are those from the right, respectively.

in Figure 2.4. The relationship between adjacent wave functions is obtained from the boundary conditions and can be generalized as,

$$a_1 = \gamma a_r \frac{k_1 + k_r}{2k_1} e^{j(k_r - k_1)z} + \gamma b_r \frac{k_1 - k_r}{2k_1} e^{-j(k_r + k_1)z} \quad (2.7a)$$

$$b_1 = \gamma a_r \frac{k_1 - k_r}{2k_1} e^{j(k_r + k_1)z} + \gamma b_r \frac{k_1 + k_r}{2k_1} e^{-j(k_r - k_1)z} \quad (2.7b)$$

where

$$\gamma = \sqrt{m_1^*/m_r^*} . \quad (2.7c)$$

The subscript 1 and r respectively mean left and right side of the junction. The Eqs. (2.7) can be expressed in matrix form as,

$$\begin{bmatrix} a_1 \\ b_1 \end{bmatrix} = \begin{bmatrix} M_{11} & M_{12} \\ M_{21} & M_{22} \end{bmatrix} \begin{bmatrix} a_r \\ b_r \end{bmatrix} \quad (2.8)$$

where

$$M_{11} = \gamma \frac{k_1 + k_r}{2k_1} e^{j(k_r - k_1)z} \quad (2.9a)$$

$$M_{21} = \gamma \frac{k_1 - k_r}{2k_1} e^{j(k_r + k_1)z} \quad (2.9b)$$

$$M_{22} = \gamma \frac{k_1 + k_r}{2k_1} e^{j(k_r - k_1)z} \quad (2.9c)$$

$$M_{12} = \gamma \frac{k_1 - k_r}{2k_1} e^{j(k_r + k_1)z} . \quad (2.9d)$$

Thus the matrix representation of potential barriers with a finite length of interval N can be expressed as,

$$\begin{bmatrix} a_1 \\ b_2 \end{bmatrix} = \begin{bmatrix} M_1 \\ M_2 \\ M_3 \\ \cdots \\ M_{N-1} \end{bmatrix} \begin{bmatrix} a_{N-1} \\ b_{N-1} \end{bmatrix} \quad (2.10)$$

whereas at the last barrier,

$$a_1 = \gamma a_r \frac{k_1 + k_r}{2k_1} e^{j(k_r - k_1)z} \quad (2.11a)$$

$$b_1 = \gamma a_r \frac{k_1 - k_r}{2k_1} e^{j(k_r + k_1)z} \quad (2.11b)$$

The reflection terms in Eq. (2.11) are omitted because the potential after $z = z_n$ is assumed constant from which no reflections are present.

The global matrix between input and output is related as

$$\begin{aligned} \begin{bmatrix} a_1 \\ b_1 \end{bmatrix} &= \begin{bmatrix} M_{11} & M_{12} \\ M_{21} & M_{22} \end{bmatrix} \begin{bmatrix} m_{11} & 0 \\ m_{21} & 0 \end{bmatrix} \begin{bmatrix} a_N \\ b_N \end{bmatrix} \\ &= \begin{bmatrix} M_{11}m_{11} + M_{12}m_{21} & 0 \\ M_{21}m_{11} + M_{22}m_{21} & 0 \end{bmatrix} \begin{bmatrix} a_N \\ b_N \end{bmatrix} \end{aligned} \quad (2.12)$$

where the M_{ij} 's are matrix elements for $n = 1$ to $N-1$ and m_{ij} 's are for $n = N$. Hence the global transmission (T) and reflection (R) coefficients derived from Eq. (2.12) are

$$T = \frac{a_N^* a_N}{a_1^* a_1} = \frac{1}{|M_{11}m_{11} + M_{12}m_{21}|^2} \quad (2.13)$$

$$R = 1 - T. \quad (2.14)$$

2.4 I-V Characteristics

Once the tunneling probability of electrons through double

barriers is known, the current density (J) can be obtained from the following equation derived by Tsu and Esaki [1].

$$J = \frac{em^*KT}{2\pi^2\hbar^3} \int_0^\infty T^*T \ln \left[\frac{1 + \exp[(E_f - E_L)/KT]}{1 + \exp[(E_f - E_L - eV)/KT]} \right] dE_L \quad (2.15)$$

I-V characteristics calculated from Eq. (2.15) are compared with measurements in Figure 2.5. However, the fit between the predicted and measured I-V characteristics is very poor as shown in the figure. The predicted RTD parameters such as the peak voltage (V_p) and the peak to valley current ratio (PVCR) do not match the measured values. Calculated peak and valley current densities using Tsu and Esaki's model are usually 10 times higher and 2 - 3 time lower than the measured values, resulting an incorrect peak to valley current ratio. These discrepancies are due to excluding the carrier scattering and to neglecting the effect of band bending and space charges in the quantum well as well as in the accumulation layer. Tsu and Esaki [1] assumed zero voltage drop in the GaAs well and equal voltage drops across the two barriers as shown in Figure 2.6 (a). Thus the first resonance occurs at $qV_{\text{bias}} = 2E_0$, where E_0 is the ground energy level in the quasi-bound well. It can be shown that their assumption is not valid by applying Gauss' equation $\oint_s D dS = Q$. If bias is applied normal to the barrier, and neglecting any spatial variation of epitaxial material parallel to them, Gauss' equation above results in $D_{n2} - D_{n1} = \sigma$, where D_{n2} and D_{n1} are the electric flux densities across the first and second barrier and σ is surface charge density in the well. Using a barrier width of d and material with dielectric constant ϵ_s , the equation above yields $V_2 - V_1 = \sigma d/\epsilon_s$, which implies that the voltage drop across the

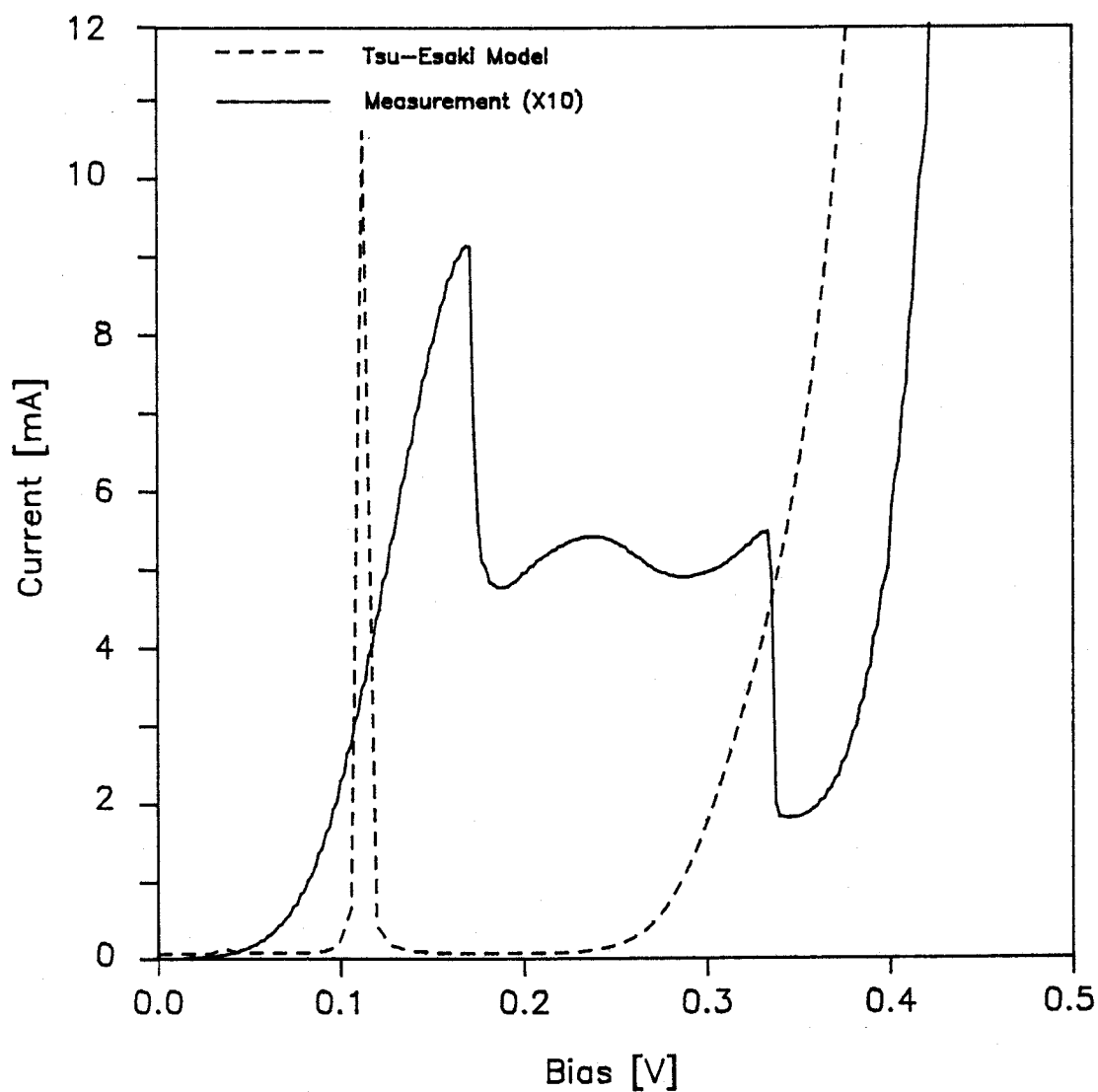


Figure 2.5: A typical I-V characteristics of a RTD measured at 77 K (solid line) and calculated from Tsu and Esaki's model.

second barrier is greater than the first and varies with the amount of charge stored in the well. Goldman *et al.* [25] reported evidence for space charge buildup in the well from a similar analogy and estimated σ to be on the order of $1 \times 10^{11} \text{ cm}^{-2}$ at resonance. They also showed evidence of charge accumulation and depletion, respectively, in the emitter and collector sides which significantly alters the resonant tunneling picture from that of Tsu and Esaki's simple model in Figure 2.6 (a) to that shown in Figure 2.6 (b). Their model is somewhat successful in interpreting the general features of RTD operation but still fails to predict the I-V characteristics correctly. Extensive efforts have been made toward RTD device modeling to improve this poor fit between theory and experiment in the past few years [26-30]. One of the most sophisticated attempts is the self-consistent approach described below.

2.5 Self-Consistent Approach

In order to calculate current-voltage characteristics of the RTD from a self-consistent approach, the mathematical model of the system must satisfy QM and classical boundary conditions, *i.e.* it must satisfy Schrodinger's equation with appropriate boundary conditions and also must satisfy three classical requirements; charge neutrality, current continuity and Poisson's equation. Each of these requirements is discussed in detail below.

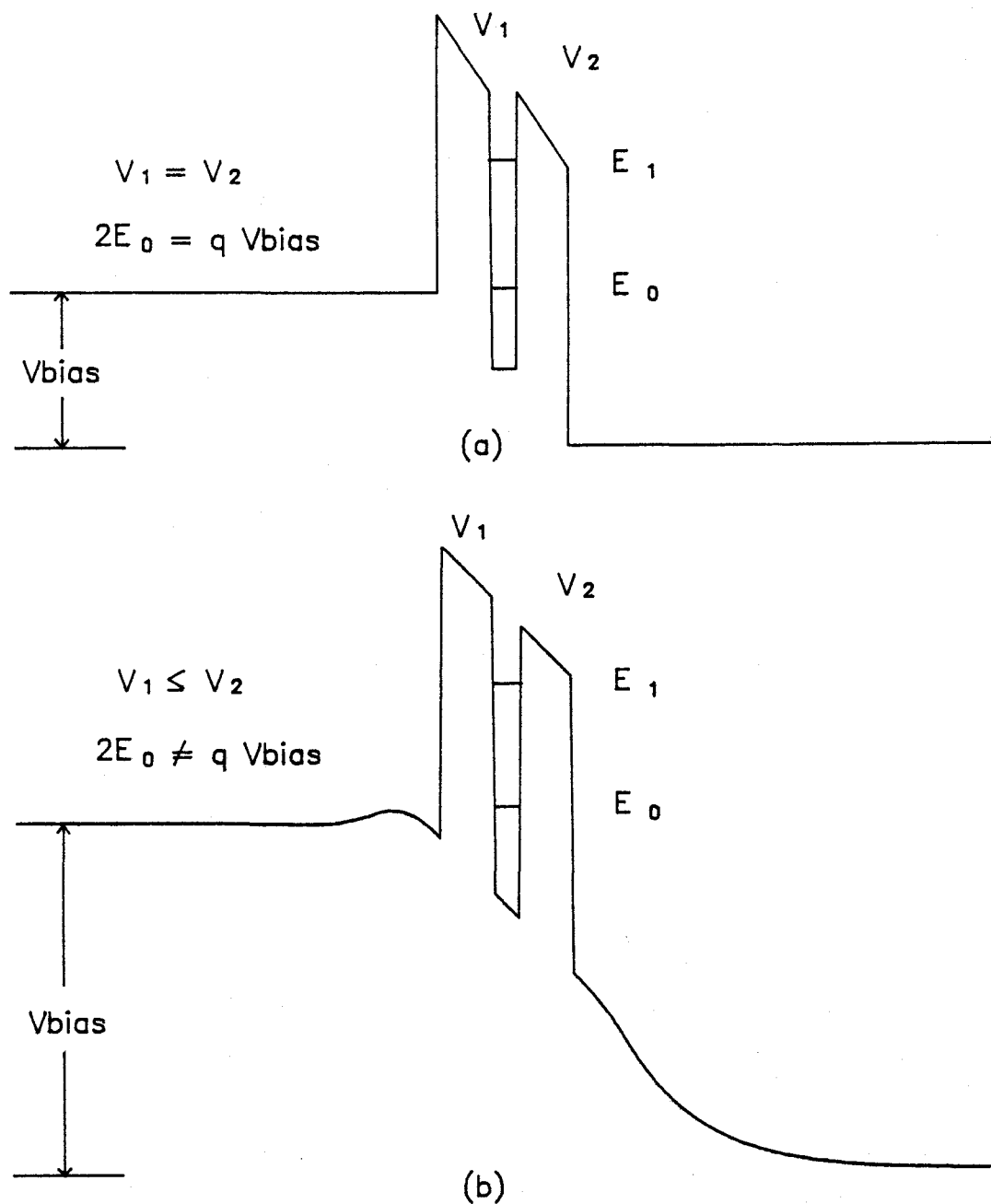


Figure 2.6: RTD under bias. (a) Tsu and Esaki's model. A linear voltage drop between the two barriers was assumed so resonant tunneling occurs at $qV_{bias} = 2E_0$. (b) The modified model which accounts for charge accumulation in accumulation layer adjacent to the emitter tunnel barrier as well as in the well. Resonant tunneling occurs at $qV_{bias} > 2E_0$.

2.5.1 Normalization of Wavefunction

The wavefunction in a closed system (a particle in an infinite well, for example) is normalized by $c_n \int \psi_n(z) dz = 1$ since $\psi(z) \rightarrow 0$ as $z \rightarrow \pm\infty$, where c_n is normalization constant [31]. The RTD, however, is an open system because $\psi(z) \rightarrow 1$ as $z \rightarrow \pm\infty$ and $\psi(z)$ can not be normalized as in a closed system. The concentration of free carriers, $n(z)$ is [28]

$$n(z) = \int_{E_l}^{\infty} \frac{dE}{2\pi\hbar v_l(E)} f(E-\mu_l) \psi_l(z) \psi_l^*(z) + \int_{E_r}^{\infty} \frac{dE}{2\pi\hbar v_r(E)} f(E-\mu_r) \psi_r(z) \psi_r^*(z) \quad (2.15)$$

where, $v_{l,r}(E)$ is the velocity of an electron of energy E at the respective boundary, $\psi(z)_l$ and $\psi(z)_r$ are wave functions incident from the left and right with an amplitude weighted by the Fermi-Dirac distribution function. Here $f(E)$ is the Fermi-Dirac distribution function integrated over the transverse momenta:

$$f(E) = \frac{m^*KT}{\pi\hbar^2} \ln(1 + e^{-E/KT}) \quad (2.16)$$

Figure 2.7 is a plot of the carrier distribution in a typical double barrier structure at 77 K without bias. An electron concentration of $1 \times 10^{18} \text{ cm}^{-3}$ in the contact region is assumed, hence the Fermi level in that region is 50 meV above CB minimum. The solid line in the figure shows a double barrier structure with barrier heights on the left ordinate. The singly broken line represents $n(z)$ with its concentration in the right ordinate and the doubly broken line is a magnified $n(z)$ away from the barrier with an arbitrary scale. $n(z)$

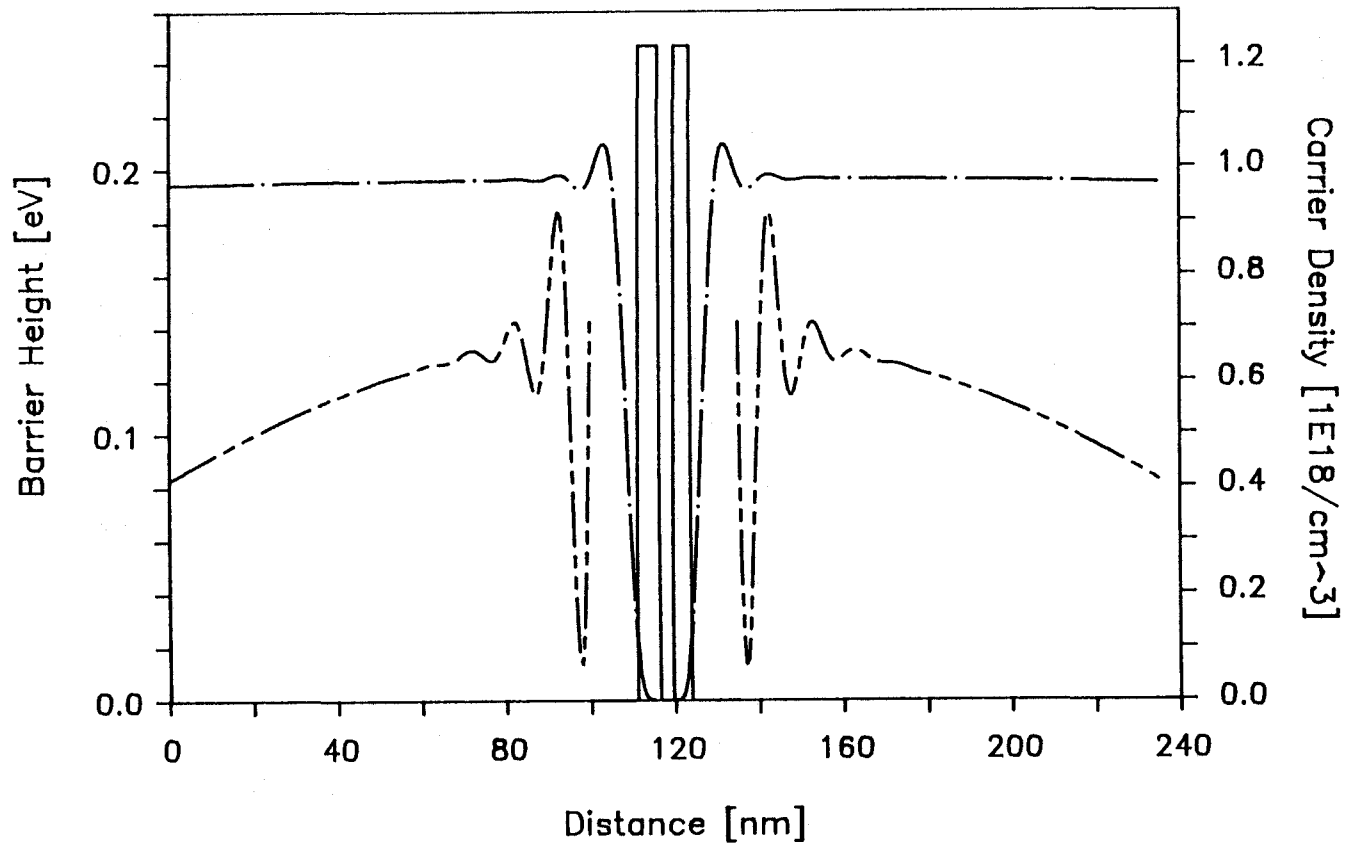


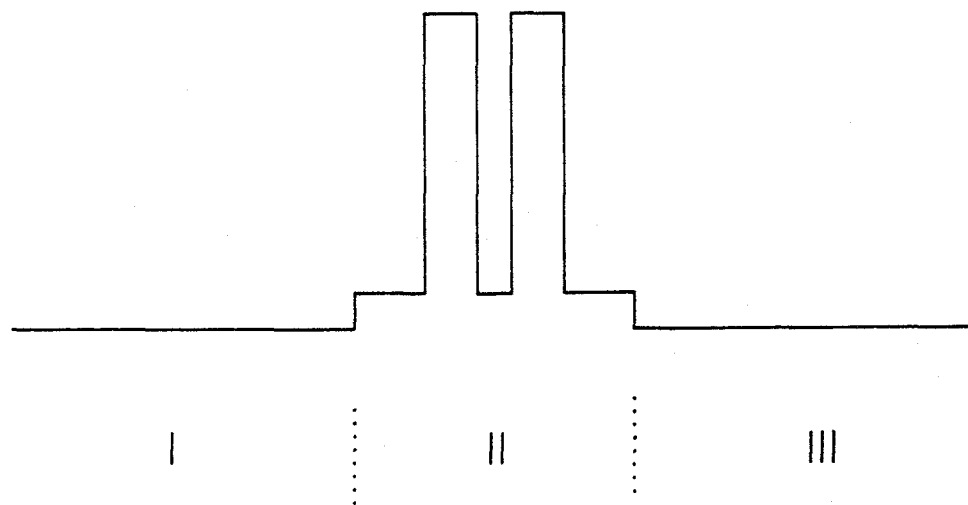
Figure 2.7: Solid line in the figure shows a conduction band profile at zero bias and singly broken line represents a carrier concentration $n(z)$. Doubly broken line depicts magnified $n(z)$ away from the tunnel barrier.

is obtained from a numerical integration of Eq. (2.16) from 0 to $3E_F$ in 2000 steps. $n(z)$ in the figure shows two interesting features. It shows an oscillatory behavior near to the barrier and an asymptotically decaying behavior away from the barrier. The former is due to a reflection from the barrier and the latter is the result of a pure quantum mechanical description of carrier distribution.

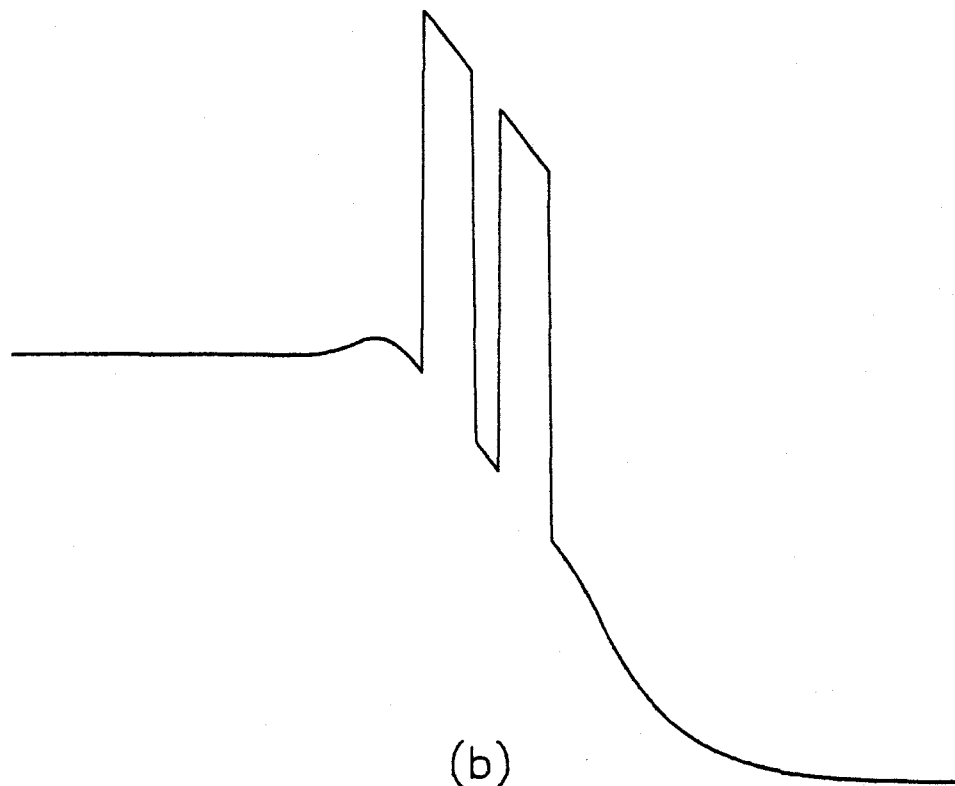
A single electron distribution $n_i(E)$ is proportional to $\psi_i(E)\psi_i^*(E)$ in the contact region from Schrodinger's equation and has the form of a standing wave due to reflection from the barrier. The amplitude of the standing wave due to a single electron shows oscillatory behavior with its oscillation period λ , where $\lambda = 2\pi/k$ and $k = \sqrt{2m^*E}/\hbar$. Electrons with minimum and maximum energies in the contact region of the above example have λ of 5463 Å and 122 Å, respectively. The distribution of electrons at lower energy or longer wavelength has more weight due to the Fermi-Dirac distribution function. Thus the resulting carrier density, $n(z)$ in the contact region shows oscillatory behavior which becomes more pronounced as E_F decreases or the doping concentration becomes smaller. This unphysical phenomena is due to a pure QM description of the carrier distribution and does not persist if carrier scattering and/or diffusion process are included. New boundary conditions have been imposed on the RTD in order to account for carrier scattering as well as diffusion.

2.5.2 Implementation of Boundary Conditions

The RTD is segmented into three region as shown in Figure 2.8 in order to incorporate scattering in a self-consistent solution. The



(a)



(b)

Figure 2.8: RTD is segmented into three regions to include carrier scattering and diffusion in a heavily doped contact region. Region I and III are classical regimes and region II is a QM regime.

boundaries of each region are chosen at the edge of the spacer layer and defined as z_1 and z_r . The carrier concentrations in region I and III are assumed to be governed by a classical description, while that in region II is purely QM. The ohmic contact is assumed to be perfect and the carrier concentration, $n(z)$ is described by an equilibrium Fermi-Dirac distribution. Then, $n(z)$ can be expressed as

for $z \leq z_1$,

$$n_1(z) = \{[n'(z_1) - N_D^+] \exp [(z-z_1)/L_{n1}] + N_D^+\} f[\eta(z)/\eta(0)] \quad (2.17a)$$

for $z_1 \leq z \leq z_r$,

$$n_2(z) = n(z) \quad (2.17b)$$

for $z \geq z_r$,

$$n_3(z) = \{[n'(z_r) - N_D^+] \exp [(z_r-z)/L_{n2}] + N_D^+\} f[\eta(z)/\eta(L)] \quad (2.17c)$$

where,

$$f[\eta(z)/\eta(L)] = \frac{F_{1/2}[(E_F - E_c(z))/KT]}{F_{1/2}[(E_F - E_c(L))/KT]} \quad (2.18)$$

$F_{1/2}$ in Eq. (2.18) are Fermi-Dirac integral of order 1/2. As the carrier concentration at each boundary must be continuous, $n_1(z_1) = n_2(z_1)$ and $n_2(z_r) = n_3(z_r)$. Thus,

$$n'(z_1) = n_2(z_1) f[\eta(0)/\eta(z)] \quad (2.19a)$$

$$n'(z_r) = n_2(z_r) f[\eta(L)/\eta(z)]. \quad (2.19b)$$

The electric field and CB potential profile as a function of z can be obtained numerically by solving the following equations,

$$\varepsilon(z) = \frac{q}{\epsilon_s} \int^z n(z) dz \quad (2.20)$$

$$V(z) = - \int^z \epsilon(z) dz. \quad (2.21)$$

The characteristic lengths, L_{n2} and L_{n1} in the collector and emitter sides, are determined by the condition $\epsilon(z = L) = 0$ and $V(z = L) = V_a$, respectively. The procedure described above provides a unique value of L_{n2} and L_{n1} since L_{n2} is a boundary condition due to charge neutrality and L_{n1} is that due to Poisson's equation.

Figure 2.9 is an energy diagram of a typical double barrier structure under bias V_a . The origin of energy is taken as the Fermi energy at $z = 0$, and the Fermi level at $z = L$ is shifted by V_a . If perfect ohmic contacts are assumed at $z = 0$ and L , the carrier distribution at these limits follows equilibrium Fermi-Dirac distributions. Then $n(z)$ has to be same as $N_D^+ - N_A^-$, where N_D^+ and N_A^- are the ionized donor and acceptor concentration, respectively. The free carrier concentration, $n(z)$ resulting from this calculation close to resonance is shown as a dashed line in Figure 2.9, and it displays several interesting features. Small peaks are centered in the well and in an accumulation layer adjacent to the front barrier which corresponds to charge build up in each region. Frensley [28] also reported carrier accumulation at the accumulation layer and the well but described slightly different features in the contact layer, viz, the carrier concentration in the left contact was slightly lower and was higher in the right contact. He explains that this is due to the resonant transmission of a part of the electron distribution incident from the left, which leaves a deficit in the distribution of reflected

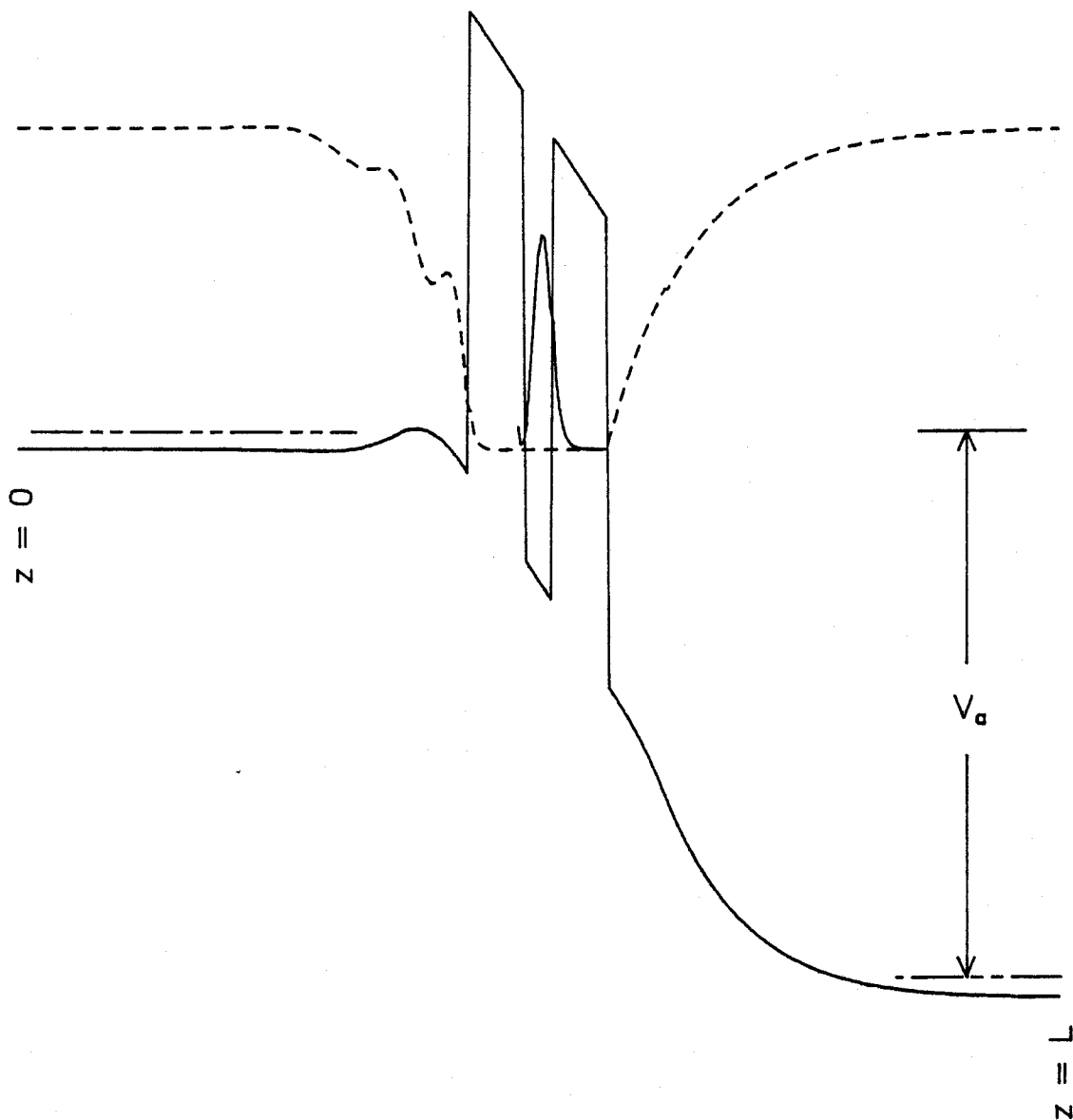


Figure 2.9: RTD under bias V_a . The solid line in the figure is the CB profile and the dotted line is the carrier concentration, $n(z)$ obtained from the new boundary condition. The solid line in the well is $n(z)$ magnified.

electrons on the left, and an excess on the right. Poetz [27] also reported results similar to those of Frensley and suggested a flexible boundary condition to account for a higher carrier concentration in a collector side of the RTD. However, they showed a uniform carrier concentration in both contact layers, which is desirable but questionable because of the reason explained in chapter 2.5.1. and shown in Figure 2.7.

Most of the other published results lack credibility since they contain at least one or more unreasonable assumptions. Development of theory in this area has not kept up with experiment since Tsu and Esaki's contribution. Problems arise from some of the questionable assumptions made in the previous section 2.3. The emitter and collector contact layers which are usually heavily doped and thicker than the DeBroglie wavelength have been treated in a QM picture. However, tunneling of carriers and energy quantization can not be explained in a classical framework. Thus a new assumption has been made; carriers in the heavily doped contact region behave classically whereas those in the active region of the RTD (barriers and well) are described by a QM picture. This approach is not totally satisfactory since it has not been proven theoretically. A rigorous mathematical proof of this model must be left for further work.

2.5.3 Solution of the Self-consistent Model

The self-consistent algorithm for calculation starts by invoking a wave function $\psi_n(z)$ from an arbitrary shaped CB profile $E_n(z)$. A new $E_{n+1}(z)$ is obtained by solving Poisson's equation from $n(z)$ which is

calculated by $\psi_n(z)\psi_n'(z)$ in Eq. (2.15). Next, generate a new wave function $\psi_{n+1}(z)$ at each point from $E_{n+1}(z)$ and repeat the above procedure until $|E_n(z) - E_{n+1}(z)|$ at every point is smaller than a given error tolerance.

The tunneling current through the double barrier structure finally calculated by the following equation.

$$J = \frac{em^*KT}{2\pi^2\hbar^3} \int_0^\infty T^*T \ln \left[\frac{1 + \exp[(E_f - E_L)/KT]}{1 + \exp[(E_f - E_L - eV)/KT]} \right] dE_L \quad (2.22)$$

Figure 2.10 is a plot of published results of I-V characteristics based on an $\text{Al}_{0.3}\text{Ga}_{0.7}\text{As}/\text{GaAs}$ RTD from three different self-consistent approaches [30]. The device consists of 40 Å thick barriers and 40 Å thick well with 45 Å spacer layers adjacent to tunnel barriers. The calculated I-V characteristics show discrepancies between authors even though the device structure is the same. Disagreement of the predicted I-V characteristics between different authors is not unusual, and results are sometimes very difficult to compare due to different structures used in their calculation and, occasionally, the lack of critical information in their publications. Much work still remains to overcome these inconsistencies.

2.6 Device Applications

A growing interest in the RTD is due to device applications as well as to theoretical novelty. There have been numerous proposals in addition to oscillators and mixers. Among them, two devices (one with two and the other with three terminals) are discussed because they

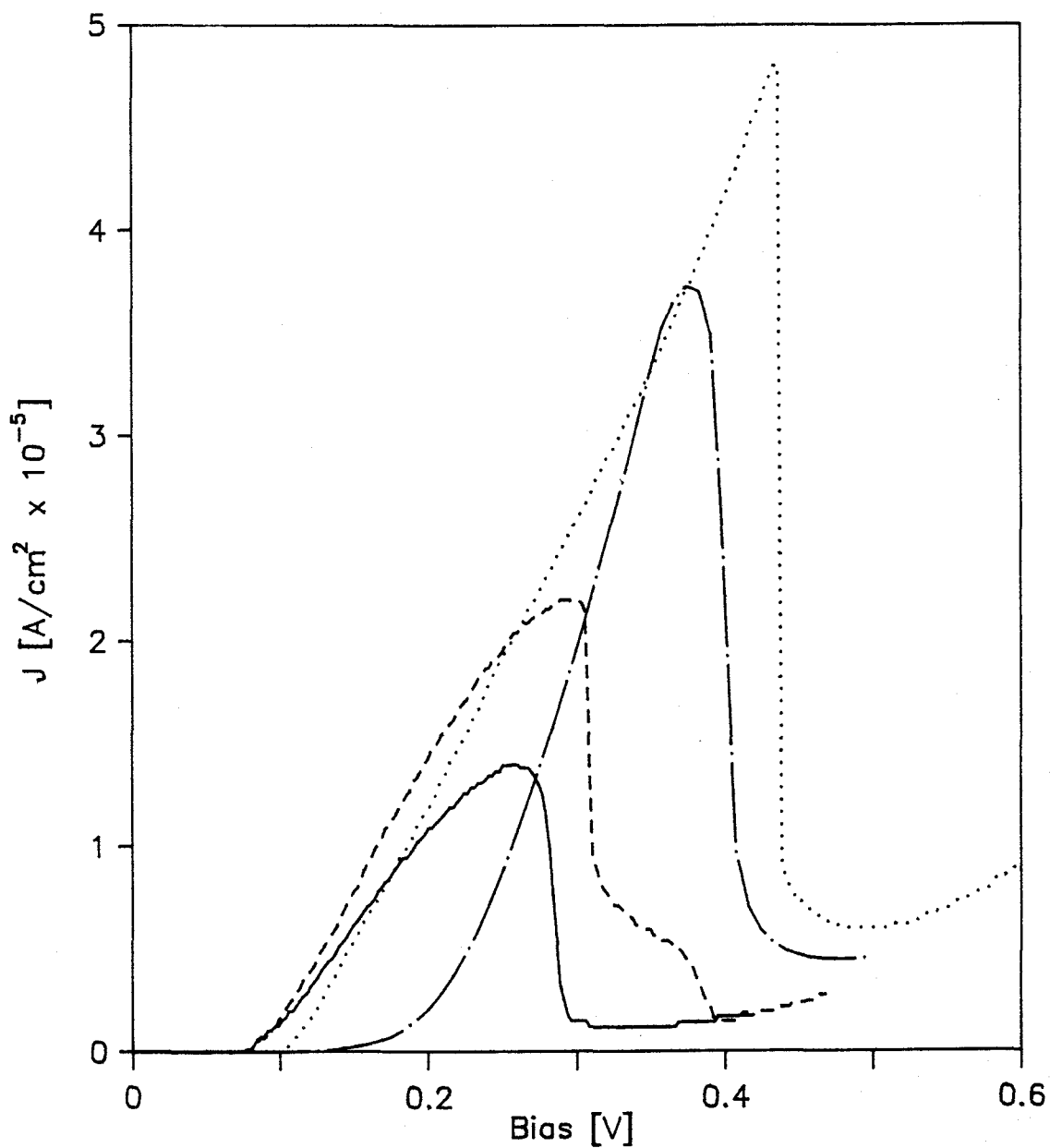


Figure 2.10: I-V characteristics obtained from four different self-consistent approaches. Solid line: Cahay *et al.*, broken line: Landheer *et al.*, dotted line: Ohnishi *et al.*, and dash and dot line: present work.

contain the most subtle and novel idea. These two device applications are included in this section since they help to further the understanding of vertical transport.

One of the two terminal devices proposed by Capasso *et al.* is a photoconductor described as an effective mass filter [32]. Since the tunneling probability through a potential barrier depends exponentially upon the effective mass, heavy holes face a narrower intrinsic resonance width than electrons. In a SL, assuming collision broadening energies for both carriers are nearly equal, the photogenerated electrons can tunnel through the structure by phonon assisted tunneling or miniband conduction, while heavy holes remain relatively localized in quantum wells since their hopping probability is negligible. SL's thus can be used to filter the transport of carriers, allowing electrons to propagate while impeding heavy holes. Applying this effect to photodetectors, Capasso *et al.* demonstrated a device with a large photoconductive gain, which could be tuned by altering the SL design parameters such as the SL period and/or duty factor [33]. In conventional photodetectors, the current gain is determined by the ratio of electron and hole velocities, if the hole lifetime exceeds the hole transit time [34]. These properties are uncontrollable for conventional photodetectors using bulk semiconductors. In SL quantum photodetectors, however, the gain is controlled by the ratio of the lifetime of hole to the transit time of electron since holes are localized in the wells. This allows greater freedom in the design of photodetectors.

One of the three terminal devices proposed by Capasso is the resonant tunneling transistor (RTT) shown in Figure 2.11 with a double

barrier structure in the base region [34,35]. Collector current is determined by the number of minority carriers injected from the emitter, which traverse the base region. The presence of the resonant tunneling structure in the base restricts transmission of electrons to those with energies near resonance. As the base-emitter potential is controlled, peaks in collector current appear when the quasi-bound state in the well aligns with the energy at which the maximum flux of electrons injected (Figure 2.11 (b)). Unlike RTDs under bias, bias is applied only to the base (QW) of the device, the symmetry of the barriers are preserved and the transmission through the structure remains close to unity if the collision broadening is smaller than the intrinsic resonance widths. The device can be used for multiple valued logic applications due to energy quantization in the well (see Figure 2.11 (b) and (c)) with ultra high speed operations [35]. The advantage of high speed operation over a p-n junction device originates from an inherent feature; it is an unipolar device so the maximum operating frequency f_{\max} is not limited by the minority carrier lifetime unlike a conventional p-n junction device.

Among other proposals in addition to the devices introduced above are a negative resistance stark effect transistor proposed by Bonnefoi *et al.* [36] and the resonant electron transfer triode (RETT) with a metal-insulator in the base by Nakata *et al.* [37]. Other proposed device applications [38-41] are not fundamentally different from the ones presented above and will not be discussed.

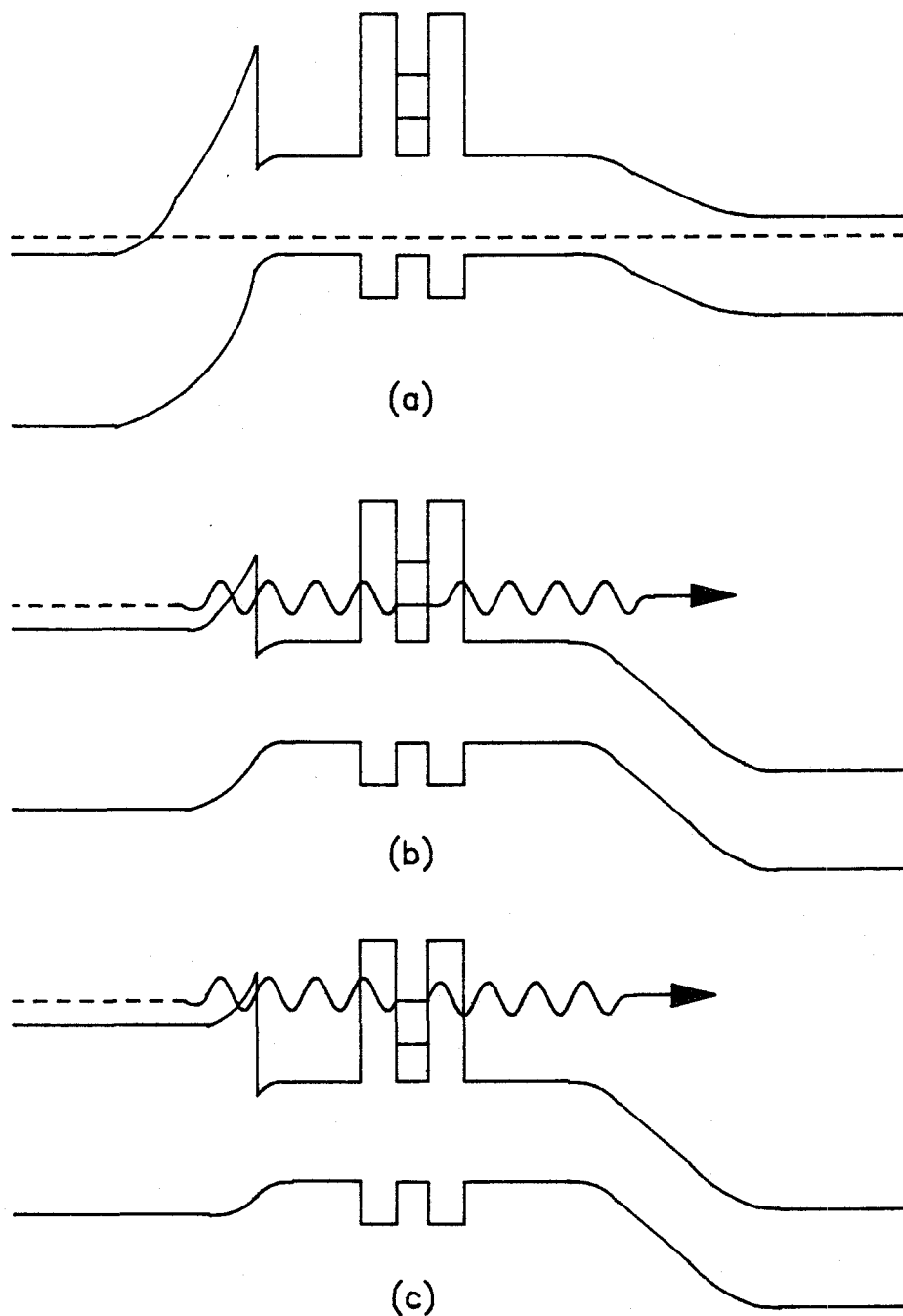


Figure 2.11: Resonant tunneling transistor (RTT) proposed by Capasso *et al.* (a) RTT at thermal equilibrium. (b) RTT biased for ground energy level tunneling. (c) RTT biased for the first excited state tunneling.

3. Experimental Technique

The experimental work in this thesis involved the fabrication of a series of $\text{Al}_x\text{Ga}_{1-x}\text{As}/\text{In}_y\text{Ga}_{1-y}\text{As}$ RTDs with various structural configurations and their subsequent electrical characterization. The effort to achieve these goals was directed into four major areas: (1) growth of the epitaxial crystal layers, (2) device fabrication, (3) device testing in electric and (4) high magnetic fields. Each of these topics will be discussed separately.

3.1 Molecular Beam Epitaxy

Molecular beam epitaxy is a versatile thin film growth technique which emerged from the three temperature method of Gunther [42] in the 1950s. The research was initiated by Arthur's kinetic study of Ga and As_2 molecular beam on GaAs surfaces in 1968 [43]. In 1974, Cho and Casey demonstrated the first double-heterostructure (DH) laser grown by MBE with quality was comparable to liquid phase epitaxy (LPE) grown material [44]. Esaki *et al.* reported the first transport measurements on superlattices grown by MBE [45]. MBE related research has grown exponentially since these initial demonstrations and a review of related publications has been well documented by Ploog and Graf up to 1983 [46].

MBE growth is in essence an ultra high vacuum deposition process which is controlled by opening or closing shutters in front of thermally heated sources. Molecular beams generated from thermal

Knudsen sources interact on a heated crystalline substrate under clean ultra high vacuum (UHV) conditions to produce a single crystal layer. Two important aspects of successful MBE growth are substrate preparation and the surface structure during layer deposition. The growth of good RTD epitaxial material involves a number of difficult choices concerning growth conditions. Many of these decisions can benefit from reference to the literature but experimentation is required to establish the correspondence between published growth conditions and those specific to a particular MBE system. To grow a high quality epitaxial film consistently, the growth parameters have to be optimized as well as reproducible. A discussion of method to optimize MBE growth parameters is well described by Ebner [47]. The two essential requirements for good RTD epitaxial material are a sharp hetero-interface and a low unintentional (background) doping. The materials involved in this research are $\text{Al}_x\text{Ga}_{1-x}\text{As}$, $\text{In}_y\text{Ga}_{1-y}\text{As}$, and GaAs. The optimum growth conditions of these three materials are similar except for the substrate temperature. Thus the problem is reduced to determining the influence of the epitaxial growth temperature on the epitaxial layer quality and finding the optimum growth temperature for the RTD structure. The growth conditions used for the three materials in this work are described briefly in the following section.

3.1.1 GaAs

Four 1 μm thick undoped GaAs epitaxial layers were grown on a semi-insulating (SI) GaAs substrate to study the effect of substrate temperature during growth. All four samples were grown in a single day

to insure the same MBE system performance during growth. All the growth parameters were identical except for the substrate temperature (500, 550, 600 and 650 C). The post growth surface morphology of all 4 epitaxial layers was comparable. Photoluminescence (PL) spectra of the samples taken at 16 K are plotted in Figure 3.1 and show two distinctive peaks at $\approx 8225 \text{ \AA}$ (1.508 meV) and $\approx 8335 \text{ \AA}$ (1.488 meV). The peaks at $\approx 8335 \text{ \AA}$ and $\approx 8225 \text{ \AA}$ are believed to be due to transitions associated with carbon acceptors and excitonics, respectively [48]. The exact transitions associated with these peaks could not be determined due to limited resolution of the PL system. Higher resolution can be obtained below liquid helium (LHe) temperature. Experiments performed at OSU showed a linear relationship between the PL intensity and the Hall mobility (μ_H), and an inverse relationship between the carbon related peak height and μ_H . The stronger the excitonic transition peak at $\approx 8225 \text{ \AA}$, the better the μ_H whereas the higher the PL intensity $\approx 8335 \text{ \AA}$ (which is the carbon related peak), the worse the μ_H . The PL spectrum of sample (a) which was grown at 500 C was magnified four times. The spectrum demonstrates a general trend of increasing carbon incorporation with increasing substrate temperature. Carbon atoms in GaAs preferentially substitute on arsenic sites and act as acceptors whose binding energy is 25 meV, and degrade the electrical and optical properties of the epitaxial material. Thus, it can be concluded that the optimum GaAs growth temperature is $\approx 550 \text{ C}$.

3.1.2 AlAs and AlGaAs

$\text{Al}_x\text{Ga}_{1-x}\text{As}$ is one of the most extensively studied III-V ternary

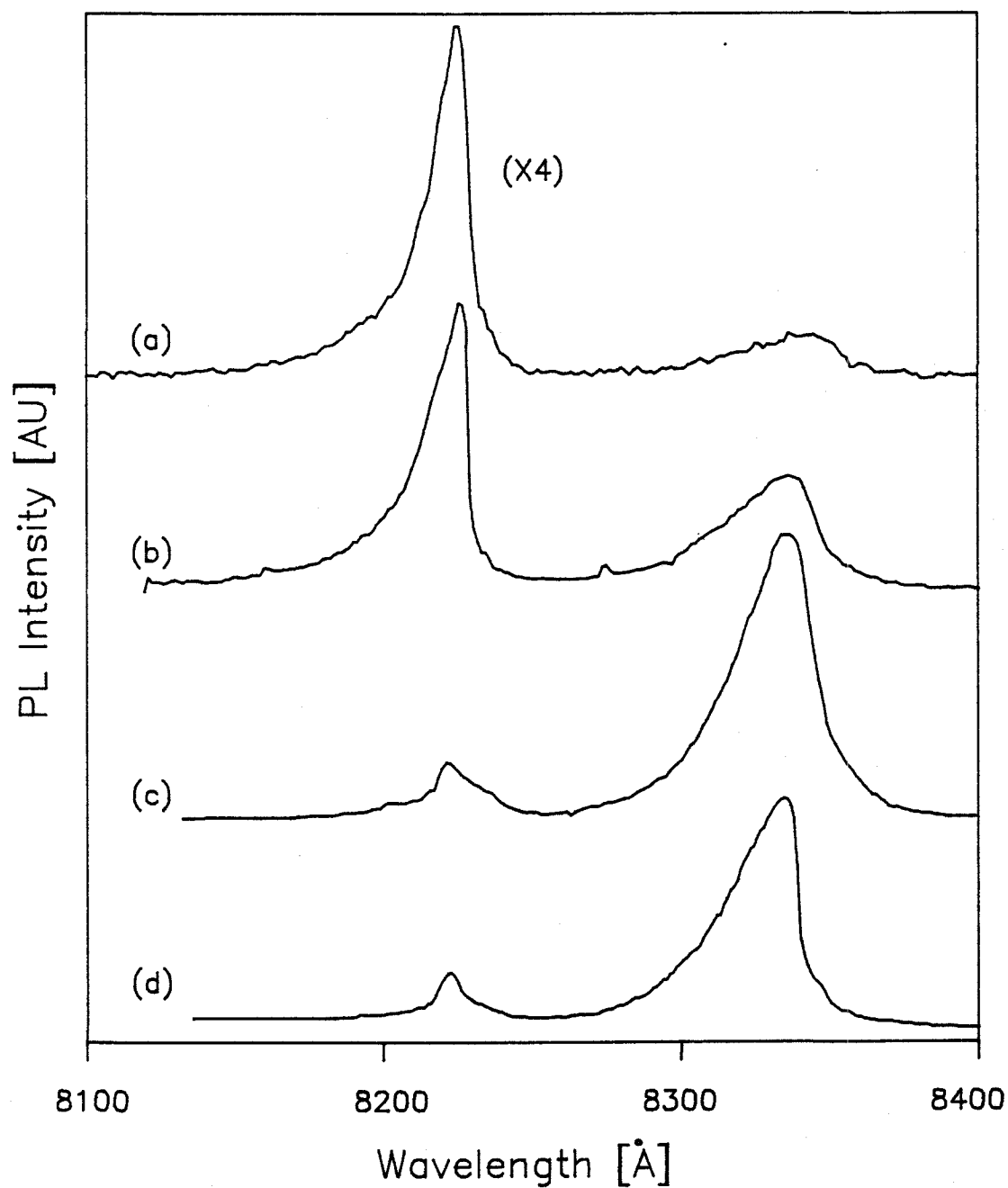


Figure 3.1: Photoluminescence (PL) of i-GaAs epi-film grown by MBE at different substrate temperature. Substrate temperatures are (a) 500 C, (b) 550 C, (c) 600 C, and (d) 650 C. PL intensity in (a) is magnified 4 times. The peaks at ~ 8355 and 8255 Å are due to transitions associated with carbon and exciton, respectively.

alloys; its lattice constant closely matches that of GaAs (0.16 % mismatch when $x=1.0$). The optimum growth temperature appears to be ≈ 680 C based on morphological and PL studies of AlGaAs [49]. However, the $\text{Al}_x\text{Ga}_{1-x}\text{As}$ barriers for RTDs used in this study were grown at 560 C for the following reasons. The AlGaAs layers are thinner than 100 Å and the substrate temperature cannot be changed rapidly from 560 C to 680 C during the brief growth time of the AlGaAs. The growth rate and composition of the AlGaAs layer are monitored from reflection high energy electron diffraction (RHEED) in molecular beam epitaxy. Usually the growth rate and Al concentration are calibrated at substrate temperature below 600 C since AlGaAs layers grown at elevated temperature do not show any measurable RHEED oscillations. This is due to preferential desorption of gallium that leads to uncertainties of alloy composition and layer thickness. Another problem in growing AlGaAs at elevated temperatures is the formation of an atomically rough hetero-interface due to the preferential desorption of gallium. The loss of gallium from AlGaAs at elevated temperature also influences the alloy composition and the layer thickness [50]. Thus a substrate temperature of 560 C for AlGaAs growth is chosen to obtain a sharp hetero-interface and a precise alloy composition.

3.1.3 Pseudomorphic InGaAs

There is a 7.2 % lattice mismatch between GaAs and InAs. However, a high quality strained pseudomorphic (pm) $\text{In}_y\text{Ga}_{1-y}\text{As}$ epitaxial layer with a mirrorlike surface can be grown on GaAs substrates within a very narrow window of growth conditions. The two critical parameters for

growth of a high quality strained pm-InGaAs layer are substrate temperature and the maximum layer thickness which varies with indium composition. For InGaAs grown on GaAs with layers thicker than a certain critical thickness (h_c), misfit dislocations are generated as the layer strain due to lattice mismatch relaxes [51]. Depending on the dislocation density, transport and optical properties can be degraded. The highest indium composition used in this study is 20 % and the well width of the RTD is 50 Å. The h_c of a single strained GaAs/ $\text{In}_y\text{Ga}_{1-y}\text{As}$ quantum well (QW) is found to be 190 Å with $y \approx 0.2$ [52]. Thus the InGaAs layer contained in the RTD used in this study is assumed to be a strained pm-layer and misfit dislocation free. Pseudomorphic InGaAs grown on GaAs substrates was also found to have a strong growth temperature dependence on surface segregation and evaporation of indium [53]. The segregation and reevaporation of indium becomes insignificant at growth temperature below 540 C [54]. PL studies of single strained pm-InGaAs/GaAs QWs performed at OSU gave the best results at a substrate temperatures of 520 C. The Hall measurement of strained pm-InGaAs layers also appears to be best at substrate temperatures of 520 C [55]. Thus the substrate temperature of 520 C is chosen for the pm-InGaAs layer growth in the present study.

3.1.4 Dopant

Silicon has been used as an n-type dopant in GaAs grown by MBE because it incorporates predominantly as an n-type shallow donor (≈ 5.8 meV below E_c) on Ga sites in GaAs. Silicon on the (100) surface of GaAs is believed to be non-amphoteric (occupying predominantly Ga sites) and

has a unity incorporation coefficient. The silicon oven temperature must be calibrated to obtain a specific doping level. In order to do this calibration, a series of four GaAs samples were grown at four different silicon oven temperatures (1200, 1130, 1075, and 1055 C). The free carrier concentration (n) was obtained from the four samples utilizing Hall measurements at room and liquid nitrogen temperature [56].

3.1.5 RTD Growth

Prior to the growth of each RTD structures, the molecular beam fluxes of the group III metals (aluminum, gallium and indium) were calibrated on a separate substrate. The group III source oven temperature was calibrated by measuring the temporal oscillations in the RHEED pattern subsequent to opening the group III element oven shutter under group V (arsenic) fluxes. Electron diffraction measurements were performed using a 10 KeV incident beam at a glancing angle of $1/2$ degrees. The diffracted intensity was monitored by direct measurement of the light intensity produced by the beam using a photomultiplier tube (PMT) that was coupled to the phosphor screen via a moveable optic fiber bundle.

The epitaxial layers of the RTDs shown in Figure 3.2 were grown in a Perkin-Elmer 425B MBE system. The RTD substrate material used in the epitaxial growth was a silicon $2 \times 10^{18} \text{ cm}^{-3}$ doped $\langle 100 \rangle$ GaAs. The substrates were prepared, prior to being introduced into the MBE system, by a standard cleaning and etching procedure: namely, immersion in room temperature, static, baths of trichloethane (TCA), acetone,

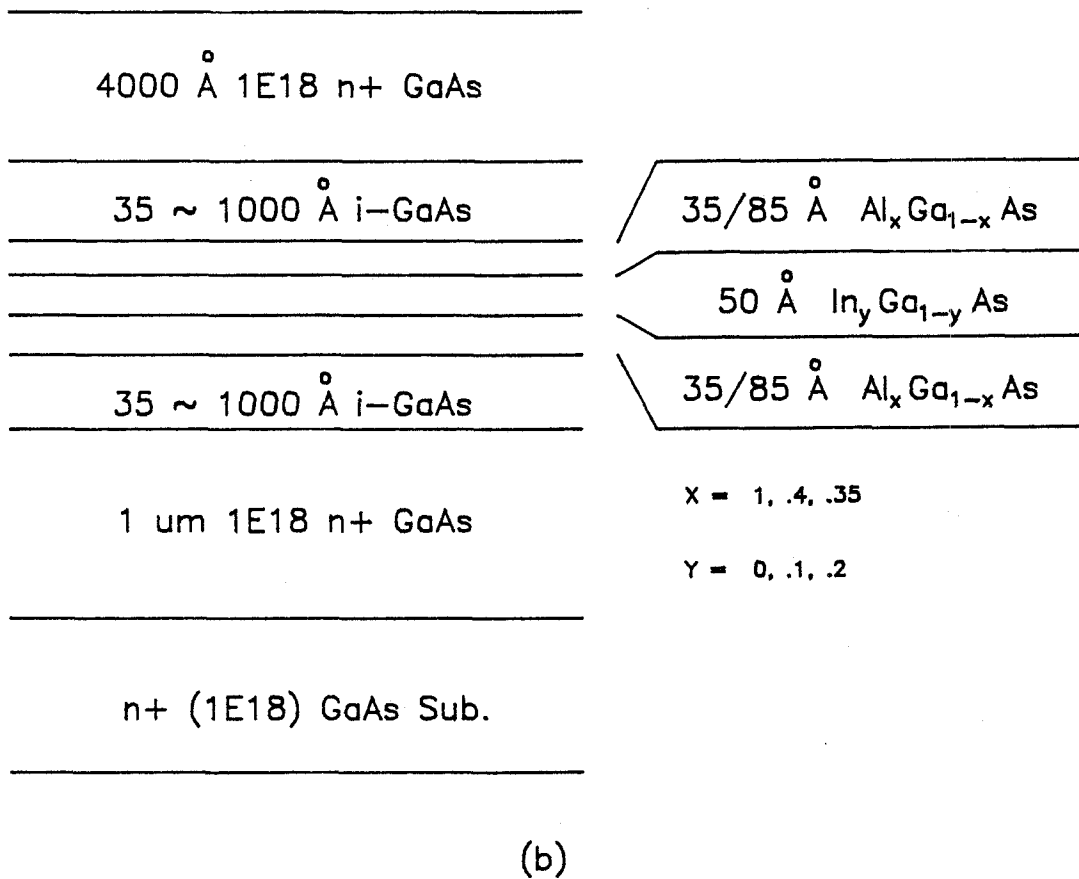
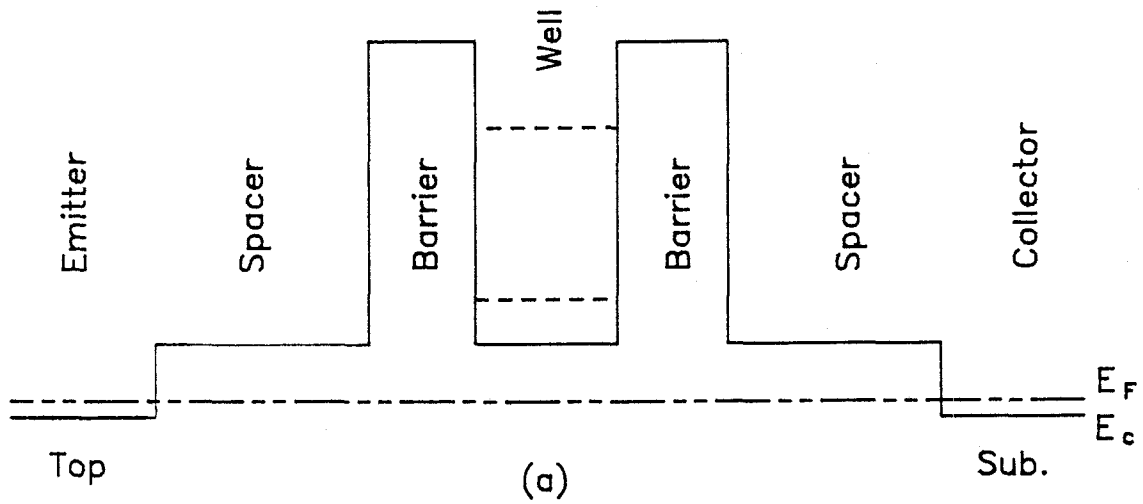


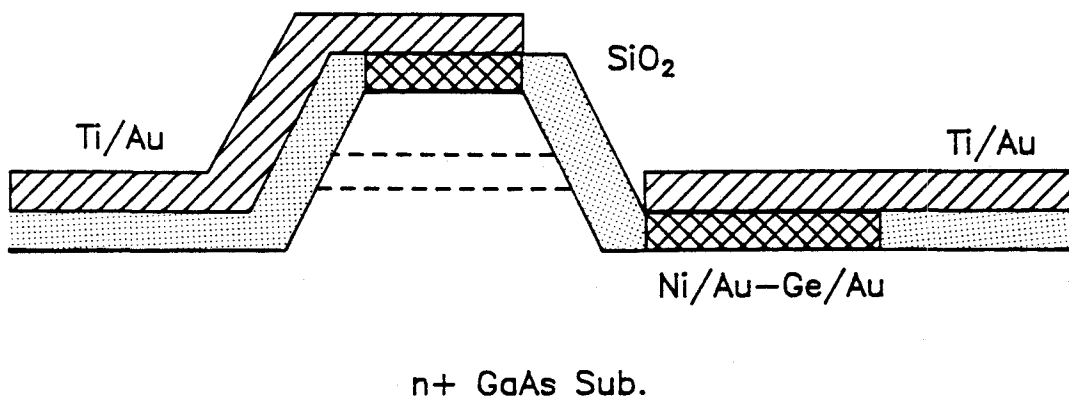
Figure 3.2: RTD structures used in the present work. (a) The CB profile of the metallurgical junction. (b) Vertical structures.

methanol and de-ionized (DI) water, 30 seconds each in sequence. A chemical etch in a solution of 5 % choline in water was then done, statically, at room temperature for 1 hour. The substrates were rinsed for 10 minutes in running DI water, spun dry and finally attached to molybdenum blocks using an indium soldering technique.

Epitaxial layers comprising the RTD were grown using a 30 second growth interruption technique between every hetero-interface under continuous arsenic flux. The interrupted growth improves the interface sharpness although it also increases impurity accumulation there. Thus the trade-off between a continual and an interrupted growth depends on the importance of the unintentional background doping level. The background doping of the MBE grown epitaxial layer was monitored regularly by Hall and PL measurements. It appeared to be below $5 \times 10^{15} \text{ cm}^{-3}$ during the RTD growth period. The more abrupt interface was chosen rather than a lower unintentional doping level in order to achieve a high performance RTD based on consideration of the well known silicon dopant segregation problem as well as to achieve low unintentional doping during the period. According to Schubert *et al.* [58], Si atoms in GaAs tends to outdiffuse during MBE growth due to surface Fermi level pinning. Thus, the entire RTD structure was grown at 560 C except for the indium compound layer. The substrate temperature for the InGaAs layer was adjusted to its optimum growth temperature of 520 C during growth interruption and raised to 560 C for the rest of the structure growth.

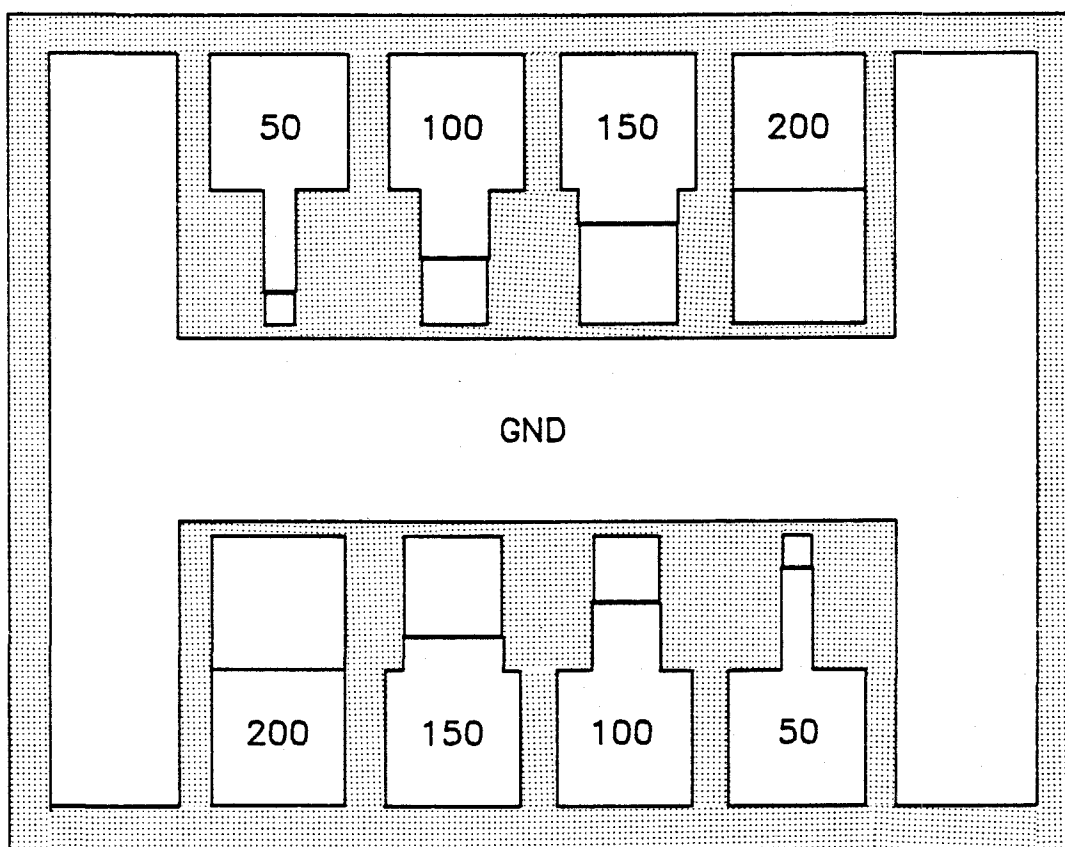
3.2 Device Fabrication

The process developed to construct RTDs from the MBE grown epitaxial material consists of 4 photolithographic steps. Figure 3.3 (a) is a schematic side view after final device processing. Figure 3.3 (b) is a top view of the final metalization mask used to construct the RTDs and the numbers in the figure represent the device dimensions in micrometers. After epitaxial growth of the RTD structure, the bottom ohmic contact area was etched using conventional photolithography; 100 Å thick Ni, 1200 Å thick Au-Ge and 1500 Å thick Au layers were then sequentially evaporated utilizing a lift-off procedure [59]. The contact area was chemically etched using a 2 minute HCl dip to remove the native oxide from the GaAs surface prior to depositing the ohmic contact metalization. The Ni/Au-Ge/Au ohmic contact were annealed at 420 C for 5 minutes in a tube furnace. Ohmic contacts serve as an etch mask during mesa etching for device isolation. Mesas were etched using a solution of $\text{NH}_4\text{OH}(1) + \text{H}_2\text{O}_2(1) + \text{H}_2\text{O}(5)$ followed by SiO_2 deposition for device passivation using plasma enhanced chemical vapor deposition (PECVD). The ohmic contact areas under the SiO_2 were etched and 100 Å of Ti and 1500 Å of Au were sequentially evaporated for bonding pads. Finally, the RTDs were mechanically diced and wire bonded in an integrated circuit (IC) package for measurements.



n^+ GaAs Sub.

(a)



(b)

Figure 3.3: (a) Side view of the RTD after final processing. (b) The final metalization mask. The numbers in the figure represent lateral device dimensions in micrometers.

3.3 Current-Voltage Characteristics

Current-voltage (I-V) characteristics of the RTD were taken using an experimental setup shown in Figure 3.4. The setup consists of a programmable constant voltage source and a precision digital volt meter (DVM) rather than a standard curve tracer in order to control bias voltage sweep speed. The RTDs exhibited a current bistability in the negative differential resistance (NDR) region of the I-V curve that is believed to be due to either an intrinsic bistability of the device or an external loading effect from the measurement system [60]. Foster *et al.* removed the current bistability by placing a suitable capacitor across the device [61]. However, this technique was not adopted since the I-V characteristics obtained with a capacitor parallel to the RTD smears out the detailed structures in the NDR region. The magnitude of the hysteresis was found to be a function of a bias sweep speed; *i.e.* the I-V curve of the RTD does not show a current bistability if the bias sweep speed is slow enough. Thus the standard curve tracer was not used and the bias sweep speed for the measurement was set such that the RTD did not show current bistability in the valley region of I-V curve.

3.4 High Field Magneto-Transport

Application of a magnetic field B in the z direction (growth direction) causes circular orbits for electrons in the xy plane with angular frequency $\omega_0 = eB_z/m^*$, where m^* is an electron effective mass. Application of magnetic field normal to the barriers, B_z , has two

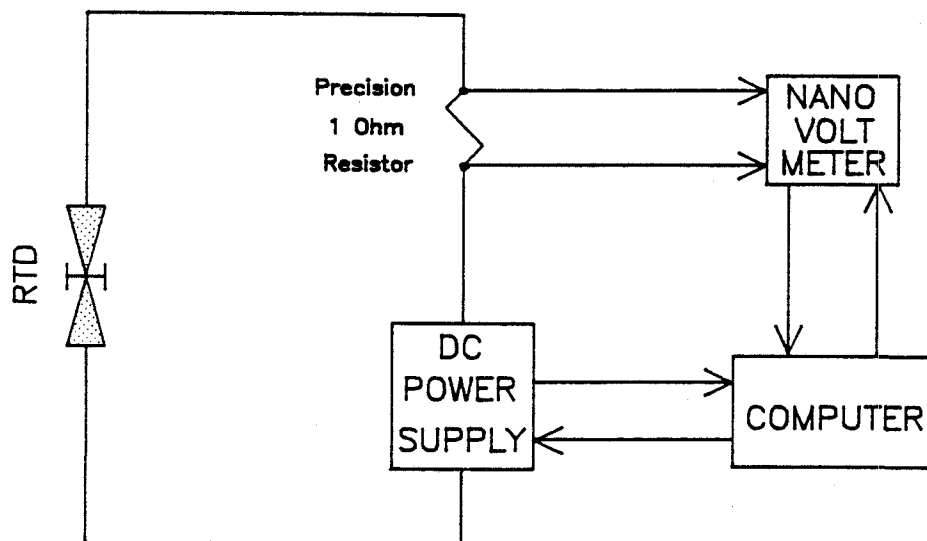


Figure 3.4: Experimental setup for I-V characteristic measurements.

effects; first it diamagnetically increases the energy levels and secondly, it changes the density of states. At high magnetic fields, the cyclotron frequency of electrons in an accumulation layer or quantum well becomes comparable to the scattering rate, and thus magnetic quantization may become important. A quantum mechanical (QM) treatment shows that the only permitted orbits would have radii corresponding with an angular momentum which is a multiple of \hbar . The energy levels of the system are

$$E = E_i + \frac{\hbar^2 k_z^2}{2m^*} + (n+1/2) \hbar\omega_c \quad (3.1)$$

where E_i is the bottom of the i th subband, and n is the n th Landau level index; $n = 0, 1, 2, \dots$. The electron is free in z direction, but for directions normal to the magnetic field, it is trapped in an effective harmonic oscillator potential. This quantization affects the description of the permitted energy states and their locations in k -space. The E - k dispersion relationship in a magnetic field shows a series of magnetic subbands and the allowed energy levels in conduction band diagram of RTD are correspondingly modified as shown in Figure 3.5. The dotted and solid lines in the figure represent the energy levels with and without magnetic field.

The energy levels in the accumulation layer (E_a) and the well (E_q) under a quantizing magnetic field are given by

$$E_a = \hbar eB/m^* (n+1/2) + E_{a0} \quad (3.2a)$$

$$E_q = \hbar eB/m^* (s+1/2) + E_{q0} \quad (3.2b)$$

where n and s are Landau level indices in the accumulation layer and the well, respectively. E_{a0} and E_{q0} are the quantized energy levels in

the accumulation layer and the well without magnetic field. Tunneling which is not allowed in the absence of the magnetic field becomes possible if the condition $E_a = E_q (+\hbar\omega_L)$ is satisfied. The conservation of k_z momentum for $B = 0$ corresponds to conservation of Landau level index $n = s$ in the presence of a quantizing magnetic field [62]. The $\hbar\omega_L$ in the parentheses allows for transition in which k_z is not conserved ($n \neq s$) and corresponds either to a longitudinal optical (LO) phonon or an acoustic phonon emission. Thus some tunneling features which were not allowed without a magnetic field become apparent by application of a magnetic field. This phenomenon is observable in pure specimens only at low temperatures in a strong magnetic field because the quantization of the electron orbits is blurred by collisions and the population oscillations are averaged out by the thermal population of adjacent orbits at higher temperatures.

The current through the RTD at a fixed bias as a function of magnetic field applied normal to the barrier shows oscillatory behavior. The oscillation period in $1/B$ becomes periodic in theory. The origin of the oscillations comes from either the bulk, an accumulation layer or quasi-bound state in the well [63]. The oscillations show different features depending upon their origin. The oscillation originating from the bulk have a three-dimensional nature which can be distinguished from the others by a lack of angular dependence of the oscillation period on field direction. Oscillations associated with Landau levels in the accumulation layer passing through the Fermi energy E_F of the contact layer are given by $E_F = E_a$. The oscillations due to the electrons tunneling into Landau levels in the well and scattering into another Landau level, possibly with LO phonon

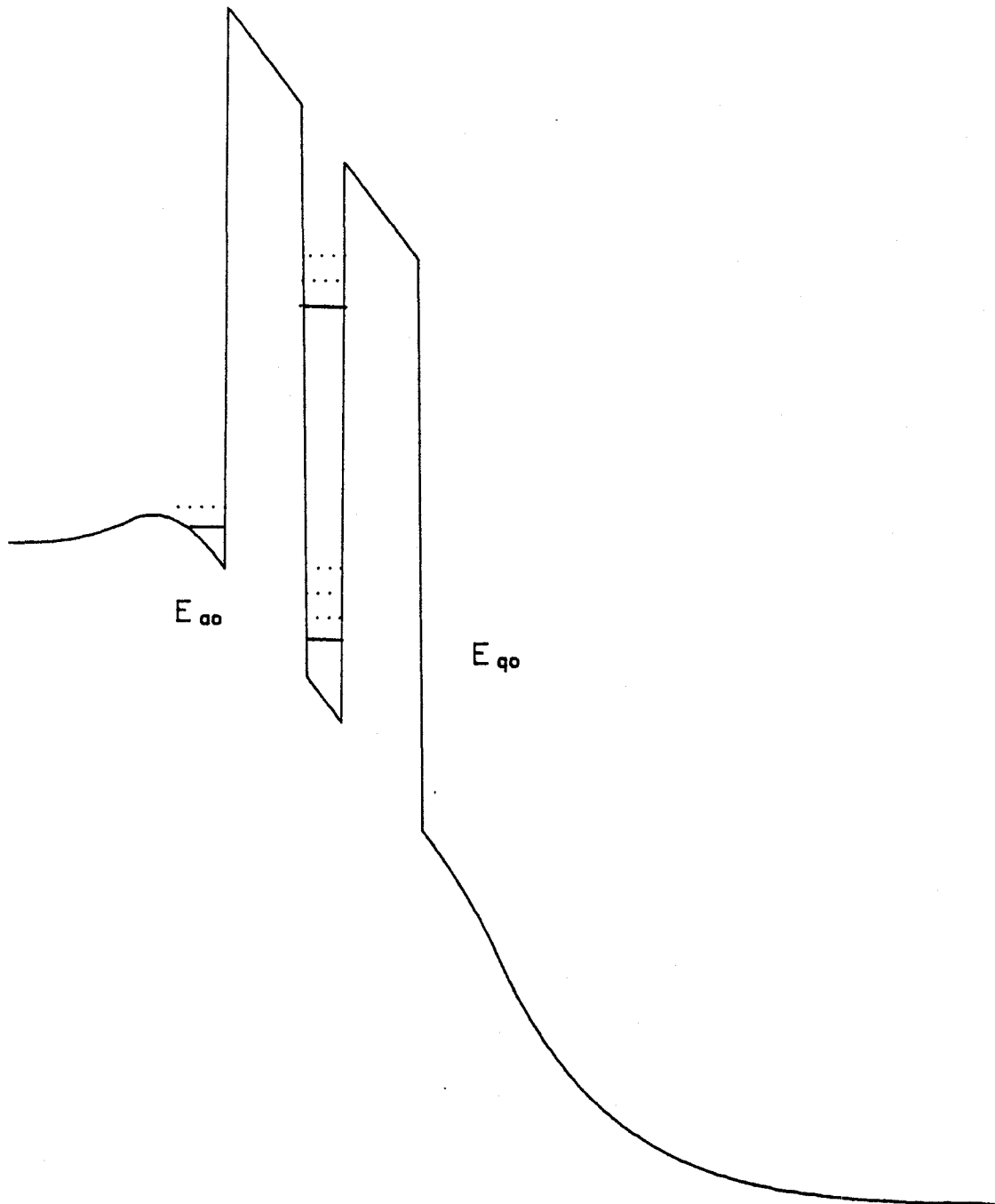


Figure 3.5: Conduction band profile under the influence of a quantizing magnetic field. The magnetic field is assumed to be normal to the barrier ($B \parallel J$). The energy levels denoted by the dotted and the solid lines are with and without magnetic field, respectively.

emission, are given by $E_a = E_q + \hbar\omega_L$. The oscillation period, $\Delta(1/B)$, of the former case is given by $\hbar e/m^*(E_F - E_{a0})$, while the period for the latter is $\hbar e/[m^*(E_{a0} - E_{q0}) - \hbar\omega_L]$. If the origin of oscillations is the accumulation layer, the periods are directly related to the two-dimensional (2D) carrier density by $n_{2d} = 2eB_f/h$, where $1/B_f = \Delta(1/B)$ and n_{2d} is a 2D carrier density [64].

I-V characteristics of the devices in high magnetic field and Shubnikov-de Haas (SdH) measurements were performed using an Oxford Vertical 9/11 Tesla Spectromag 2 system at temperatures as low as 1.8 K. The maximum field obtainable from the magnet is 9 Tesla at 4.2 K and 11 Tesla at 2.2 K. The sample holder in the magnet is designed in a way that the magnetic field is applied normal to the RTD barriers, *i.e.* parallel to epitaxial growth direction. The SdH oscillations were obtained using a small AC modulation technique [65] utilizing an experimental setup shown in Figure 3.6.

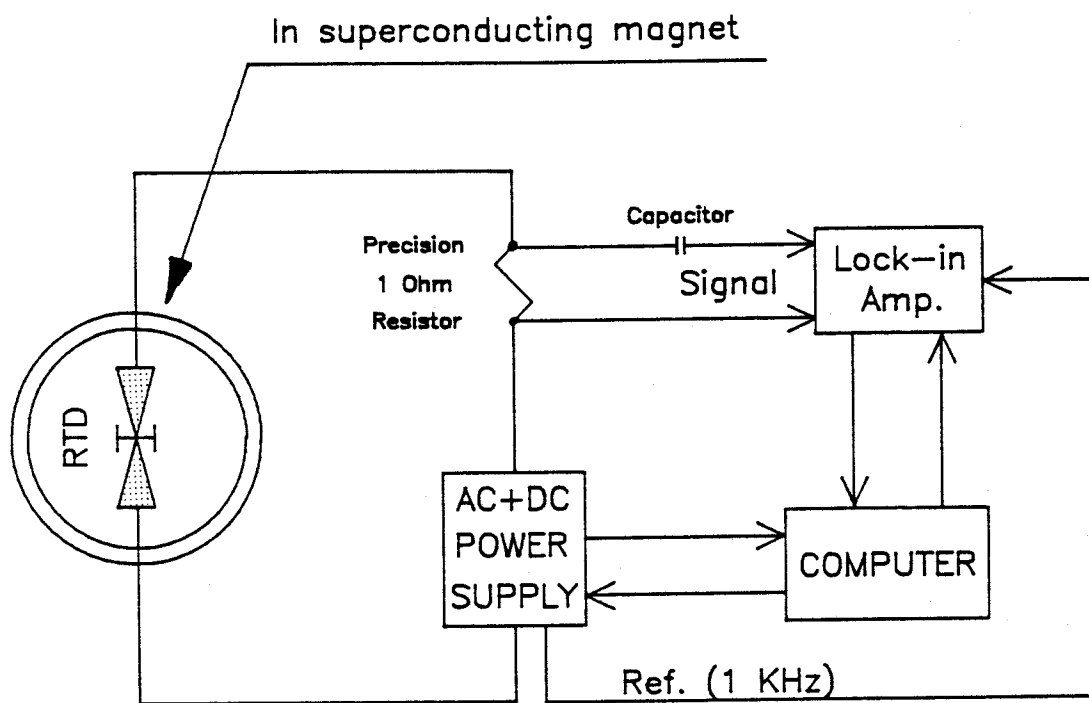


Figure 3.6: Experimental setup for Shubnikov-de Haas type measurements.

4. Experimental Results and Analysis I

In this chapter, the performance of the lattice matched and pseudomorphic (pm) RTDs are compared via electric and magnetic field measurements. The fabricated RTDs were tested at cryogenic temperature with and without a magnetic field. The lattice matched RTD is fabricated from AlAs/GaAs layers and the pseudomorphic (pm) RTD consists of $\text{Al}_{0.4}\text{Ga}_{0.6}\text{As}$ barriers and an $\text{In}_{0.1}\text{Ga}_{0.9}\text{As}$ well.

The measured current-voltage characteristics of the lattice matched RTD show a strong phonon assisted tunneling peak at voltages higher than the first resonance. SdH oscillations obtained from these device exhibit more than one fundamental oscillation frequency as a function of magnetic field. A further discussion regarding this device is continued in section 4.1 followed by an analysis of the pm-RTD in section 4.2. The pm-RTD shows different characteristics, with a resonant peak that is much wider and a valley region that is much narrower than that observed from lattice matched RTDs. These differences are produced by the presence of the ternary alloy InGaAs in the well which increases various kinds of scatterings, such as alloy and interface roughness scattering.

4.1. Lattice-Matched AlAs/GaAs RTD

The lattice matched AlAs/GaAs RTDs were comprised of the following layers, in order of growth from the n^+ GaAs substrate : 1.0 μm of $n = 2 \times 10^{18} \text{ cm}^{-3}$ GaAs buffer layer, 250 Å of $n = 2 \times 10^{18} \text{ cm}^{-3}$ to

$1 \times 10^{16} \text{ cm}^{-3}$ linearly graded GaAs, 150 Å of undoped GaAs spacer layer, 35 Å undoped AlAs barrier, 85 Å undoped GaAs well, 35 Å undoped AlAs barrier, 150 Å of undoped GaAs spacer layer, 250 Å of $n = 1 \times 10^{16} \text{ cm}^{-3}$ to $2 \times 10^{18} \text{ cm}^{-3}$ linearly graded GaAs layer and 0.5 μm of $n = 2 \times 10^{18} \text{ cm}^{-3}$ GaAs top contact.

4.1.1 I-V Characteristics

Figure 4.1 (a) and (b) respectively are a schematic of the CB profile of the AlAs/GaAs RTD and a plot of its I-V characteristics measured at three different temperatures (RT, 77K, and 1.8K). The I-V characteristics in this figure show a general trend of increasing peak current (I_p) and valley width (W_v) but decreasing valley current (I_v) at lower temperature. The peak to valley current ratio (PVCRs) of the RTD are 1.36, 7.5, and 11.2 for RT, 77, and 1.8 K. An improved PPCR at lower temperature is due to increased I_p (198, 228, 278 μA) and decreased I_v (145, 30.2, 24.7 μA). This is due to the narrowing of the carrier distribution function and the decreasing scattering rate at lower temperature. As the temperature decreases, the carrier concentration (n) is reduced while at the same time the mobility (μ) increases so the product $n\mu$ remains relatively constant. Thus changes in n or μ do not severely affect the magnitude of the current. When the device is biased near resonance, the current increases at lower temperature since the spreading of the carrier distribution associated with the thermal energy (kT) becomes smaller. Thus the number of carriers available for resonant tunneling increases, resulting in a higher current. Broadening of the valley width at lower temperatures is

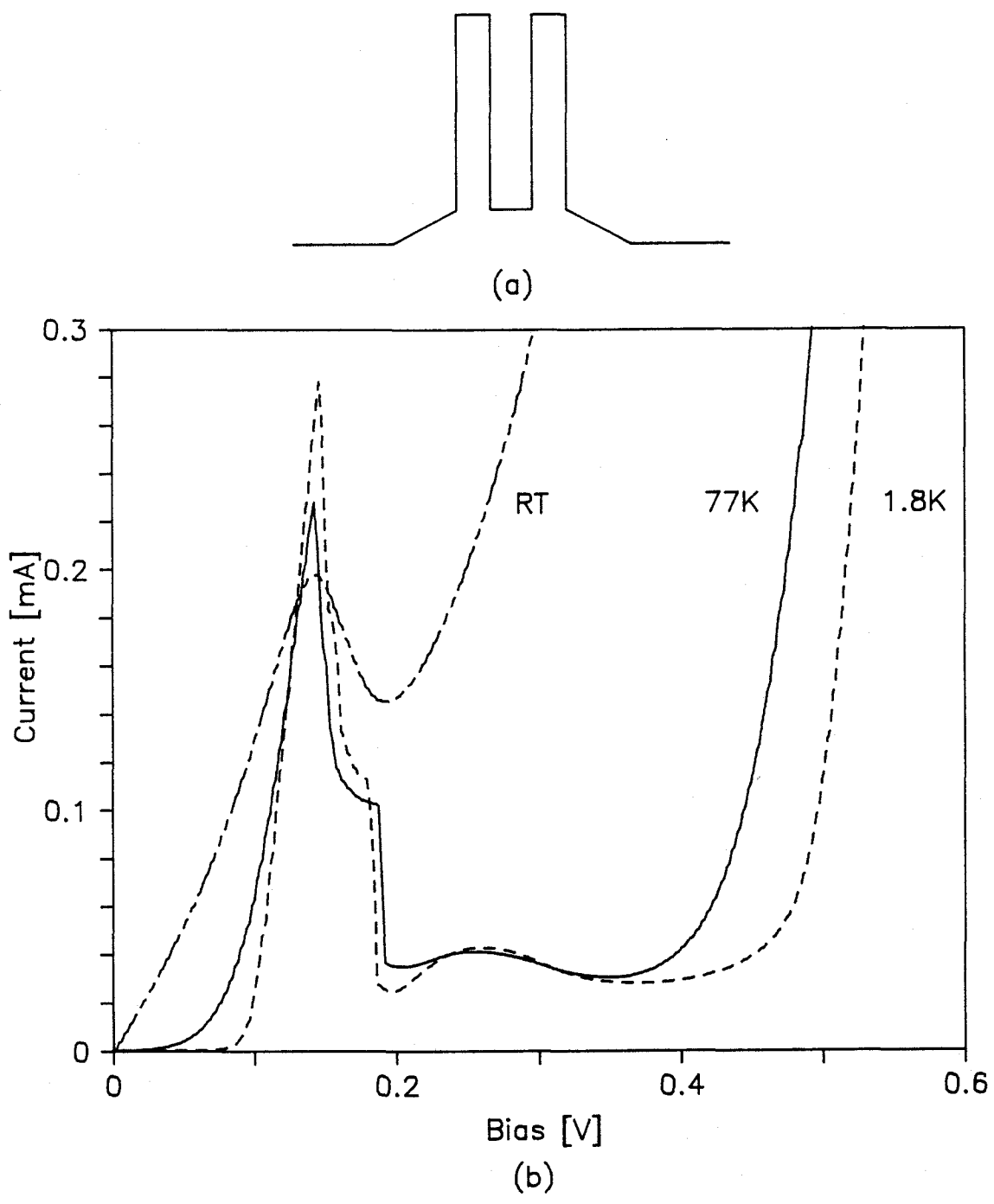


Figure 4.1: AlAs/GaAs RTD. (a) Conduction band profile. (b) I-V characteristics measured at RT, 77K, and 1.8 K.

also expected from the narrowing of the carrier distribution function since it reduces thermionic emission off resonance. At lower temperature, an improved ratio of coherent to incoherent resonant tunneling also results in a higher PVCR as discussed in chapter 1. Thus, the overall performance improves at lower temperature.

Another noticeable feature is the enhancement of satellite peaks in the valley region of the I-V curve at lower temperature. Goldman et al. [66] have attributed these subsidiary peaks to tunneling assisted by LO phonon emission. This assumption is justified from studying the I-V characteristics obtained in a magnetic field. Data in Figure 4.2 show the influence of a magnetic field applied normal to the barriers. The dashed and the solid lines are the I-V curves obtained when the magnetic field perpendicular to the barrier is 0 and 8 Tesla, respectively. The peak to valley current ratio (PVCR) of the RTD at 1.8 K is 11.2:1 with ($B = 8$ Tesla) and 10.8:1 without magnetic field, respectively. The inset of the Figure 4.2 shows the forward (the top side is biased negatively with respect to the substrate side) I-V characteristics of the RTD in the valley region under different magnetic fields.

The RTD exhibits a main resonant peak (V_p) at 144 mV and a first subsidiary peak marked as LO at 245 mV. The phonon related peak and the valley current due to inelastic scattering are revealed more clearly by applying a magnetic field B perpendicular to the barrier ($B \parallel J$) as shown in the inset of Figure 4.2. The LO phonon related first subsidiary peak after the main resonance splits into two peaks as the applied magnetic field becomes greater than 6 Tesla. The first subsidiary peak does not shift while the other peaks move to higher bias as the magnetic field

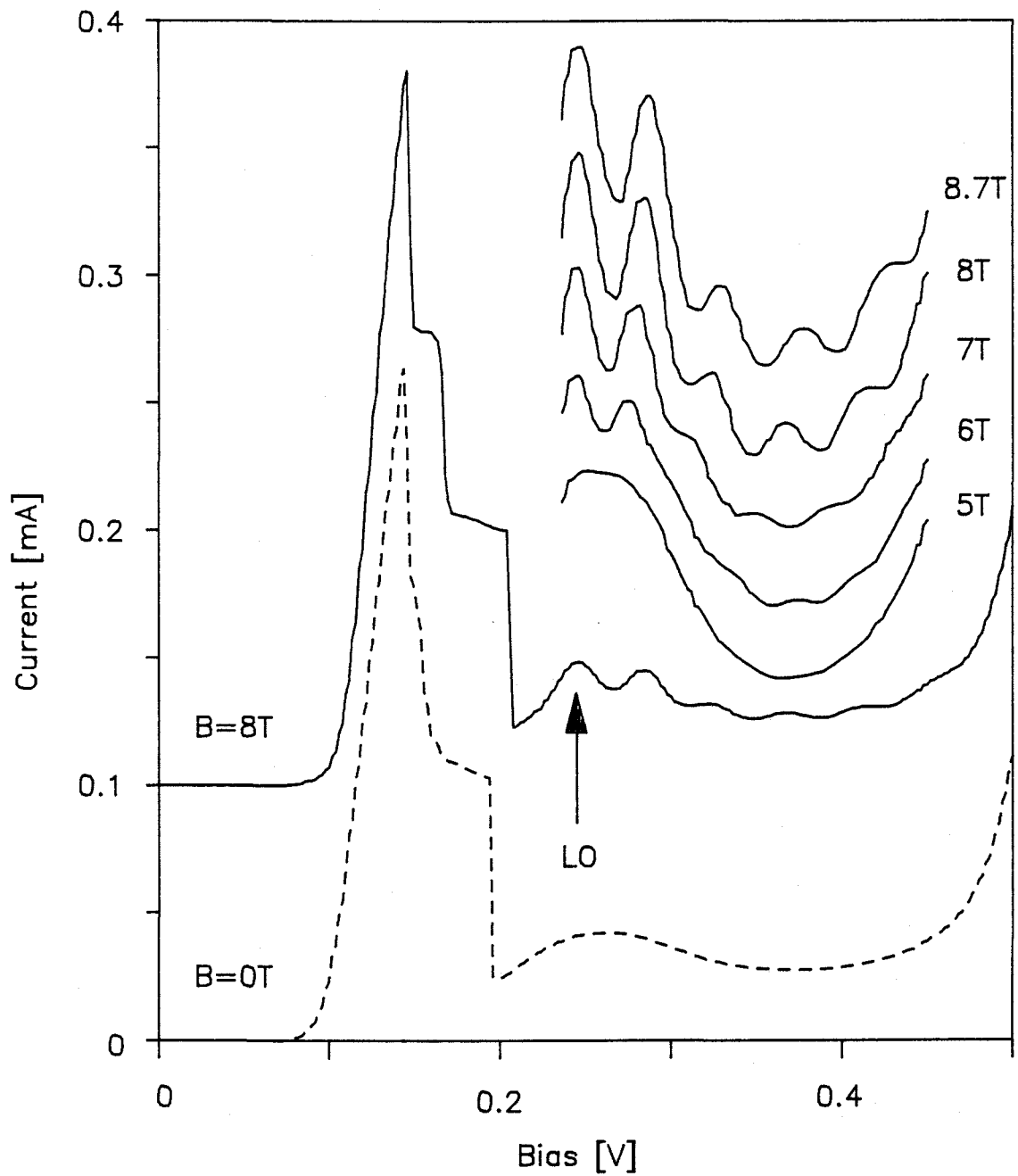


Figure 4.2: I-V characteristics of the AlAs/GaAs RTD at 1.8 K. The solid and the dashed lines are for $B = 8$ Tesla ($B \parallel J$) and 0 field, respectively. The additional curves show the valley region of the I-V curve at different magnetic fields ($B \parallel J$).

increases.

The application of a magnetic field perpendicular to the barrier quantizes the energies of electrons in the quantum well and in the accumulation layer. The energy levels in the accumulation layer (E_a) and the quantum well (E_q) in an applied magnetic field are given by Eq. (3.2) are repeated here for convenience.

$$E_a = \hbar e B / m^* (n+1/2) + E_{a0} \quad (4.1a)$$

$$E_q = \hbar e B / m^* (s+1/2) + E_{q0} \quad (4.1b)$$

where m^* is an effective mass and n and s are the Landau level indices in the accumulation layer and the quantum well, respectively. E_{a0} and E_{q0} are the quantized energies in the accumulation layer and the quantum well without magnetic field. The energy selection rule for tunneling is $E_a = E_q (+\hbar\omega_L)$ and the conservation of k_{\perp} momentum for $B = 0$ corresponds to Landau level indices $n = s$ in the presence of the quantizing magnetic field. The $\hbar\omega_L$ in the parenthesis allows for transitions in which k_{\perp} is not conserved ($n \neq s$). The $\hbar\omega_L$ can correspond either to an LO phonon or acoustic phonon emission.

The fan chart of the Figure 4.3 shows the evolution of the measured magneto-quantum peaks in the presence of the quantizing magnetic field. Electron transitions in the presence of the magnetic field with LO phonon emission are given by

$$\Delta N \times B = [\Delta E - \hbar\omega_L] m^* / \hbar e \quad (4.2)$$

where $\Delta N = (s - n)$, $\Delta E = (E_{a0} - E_{q0})$ and the rest of the symbols have the same meaning as before. The squares and the triangles are the

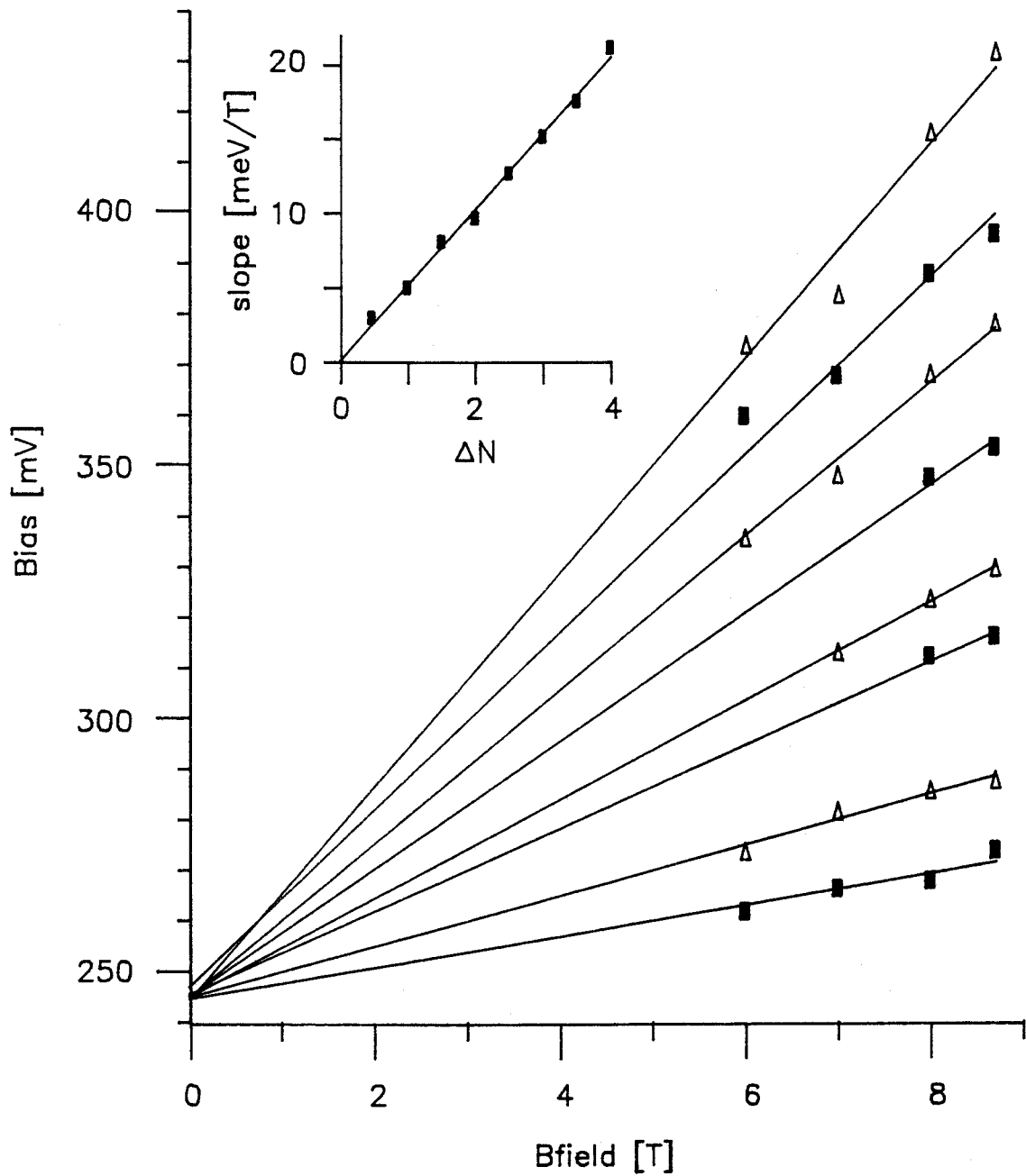


Figure 4.3: Evolution of the magneto-quantum peaks as a function of applied magnetic field ($B_{\parallel J}$). The squares and triangles correspond to the maximum and minimum of the magneto-quantum peaks, respectively. The inset figure is a plot of the slope of a least square fit as a function of Landau level index.

maximum ($\Delta N = \text{integer}$) and the minimum ($\Delta N = \text{half integer}$) of the magneto-quantum peaks, respectively and the solid lines are the results of the least squares fit of these peaks. The extrapolation of the least squares fit intersects the bias point at 245 mV marked as LO in Figure 4.2. Thus, the magneto-quantum peaks in the valley region of the I-V curve are assumed to be a result of a tunneling current through different Landau levels ($\Delta N = 1,2,3,4$) via a GaAs LO phonon emission.

The inset of Figure 4.3 is a plot of the slope of the least squares fit as a function of Landau level index, ΔN . The slope of the inset figure is 5.07 meV/T which corresponds to $\hbar e/m^* \delta$ where δ is the ratio of the voltage drop between the lowest bound state in the accumulation layer of the emitter and the half well width. $\delta = 0.34$ is obtained when the device is biased in the valley region of the I-V curve. The voltage difference between the main and the LO phonon satellite peak is 101 mV so the phonon energy measured is $101 \text{ mV} \times 0.34 = 34.3 \text{ meV}$ which is in good agreement with the LO phonon energy of GaAs, 36.25 meV [67].

The dependence of the peak positions on magnetic field enables one to distinguish direct tunneling between Landau levels from that due to phonon assisted tunneling. The former changes its peak position while the latter does not as a function of magnetic field.

4.1.2 Shubnikov-de Haas Measurement

Another experiment carried out under magnetic fields is the Shubnikov-de Haas (SdH) measurement. This measurement is a powerful technique to study the 2-dimensional (2-D) nature of electrons in an

accumulation layer or in a quasi-bound well state. Figure 4.4 (a) is an example showing the differential conductance of the RTD at a fixed bias as a function of the magnetic field ($B_{\parallel J}$). The sample does not show magneto-oscillations when biased below resonance in contrast to Mendez *et al.* [62]. The three sets of oscillations shown in this figure are taken in the valley region of the I-V curve. The oscillations may possibly originate from the bulk, the accumulation layer or quasi-bound state in the well. Oscillations originating from the bulk can be distinguished from the others by the angular dependence of magnetic field [66]. The oscillations from the bulk do not change period as a function of magnetic field direction while those from the accumulation layer or well do. The latter oscillations are either due to the Fermi energy of the accumulation layer passing through the Landau levels in that region or due to inelastic tunneling of electrons into a Landau level in the well with the emission of an acoustic or LO phonon. For simplicity, the former and the latter are identified as the accumulation and the inelastic oscillation, respectively, through this thesis. These oscillations theoretically become periodic, if plotted against $1/B$ and their theoretical description also changes depending upon the origin. The oscillations in Figure 4.4 (a) will show periodic behavior if plotted against $1/B$. They show multiple periodicity - one period below ~ 4 Tesla and another period above ~ 5 Tesla with a transition region. In the present work, the bulk has been eliminated as a possible source of oscillations since the RTD shows oscillations only after the first resonance and RTDs with very thin spacer layer do not show any.

Multiple periodicity in the magneto-quantum oscillations has been

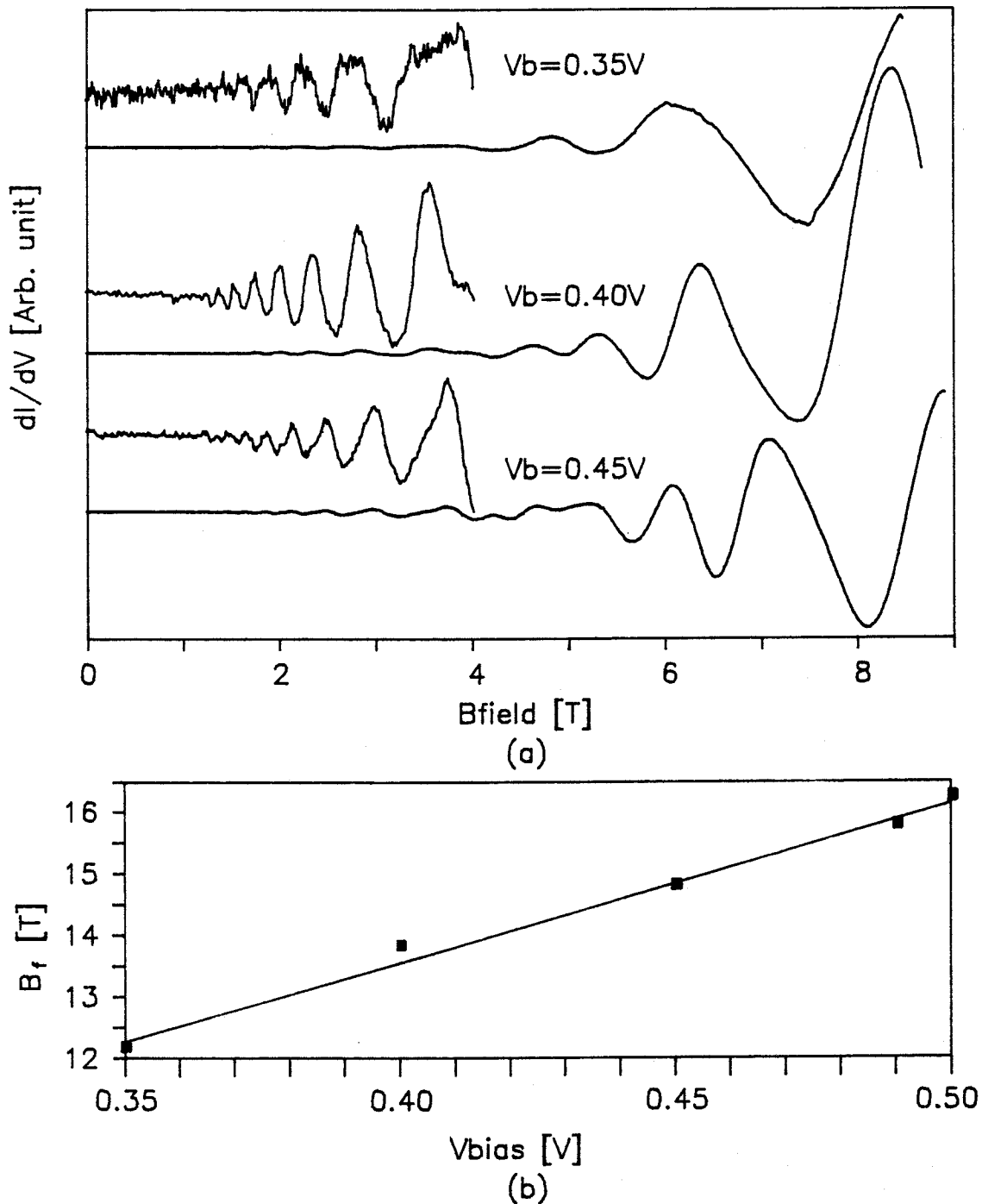


Figure 4.4: (a) Differential conductance of the AlAs/GaAs RTD as a function of magnetic field ($B_{||J}$). The inset figures are the magnified differential conductance at low magnetic field. (b) The lower series of magneto-quantum oscillation periods as a function of bias.

reported by Payling *et al.* with 1000 Å thick spacer layers adjacent to the (AlIn)As barriers on lattice matched InP substrates [68]. They interpret the multiple periodicity as due to two occupied 2D bound states in the emitter accumulation layer and tunneling into two quasi-bound states in the well with LO phonon emission. The oscillations in reference [64] seem to be a combination of multiple periods while this device shows a clear separation between the low and the high periods. In this work a single quasi-bound state in the accumulation layer of the emitter seems to be a better assumption based on comparison with the oscillation features from Eaves *et al.* [64] and also because of the use of a much thinner spacer layers on the present RTD. Magneto-oscillation periods, B_f , related to the accumulation and inelastic tunneling effects are easily derived from Eq. (4.1a) and (4.1b) and expressed as

$$B_f = \frac{m^*}{\hbar e} \left[E_F - E_{ao} \right] = \frac{m^*}{\hbar} \alpha V_a \quad (\text{accumulation}) \quad (4.3a)$$

$$B_f = \frac{m^*}{\hbar e} \left[E_{ao} - E_{qo} - (\hbar\omega_L) \right] = \frac{m^*}{\hbar e} [\beta eV_a - (\hbar\omega_L)] \quad (\text{inelastic}) \quad (4.3b)$$

where $B_f = [\Delta(1/B)]^{-1}$, α is the ratio of $(E_F - E_{ao})/eV_a$ for an accumulation layer and β is the ratio of $(E_{ao} - E_{qo})/eV_a$ in the well, and the rest of the symbols have the same meaning as before. The lower series of magneto-quantum oscillations are shown in Figure 4.4 (b) as a function of bias. The exact periodicity of the higher series oscillations cannot be determined since there are only two periods up to a magnetic field of 8 Tesla. The straight line is a least square fit of the measured oscillation period. The slope of the curve is 26 meV/T

which yields $\alpha = 0.0449$ and results in $E_F - E_{a0}$ of 20.2 meV at V_a of 0.45 V. The lower series oscillations can not be a result of inelastic tunneling since for phonon emission $E_{a0} - E_{q0}$ has to be at least greater than $\hbar\omega_L$ which is 36 meV. Thus, the lower series of oscillations are believed to be a result of the Fermi energy of the accumulation layer passing through the Landau levels of the quasi-bound state of the emitter. In this case the two-dimensional carrier density associated with oscillations is $n_{2d} = 2eB_f/h$. The lower series of B_f 's ranging from 13 to 16 Tesla gives an equivalent 3D density of $5 \sim 7E17 \text{ cm}^{-3}$ which agrees reasonably well with the emitter doping concentration.

The higher series of oscillations are assumed to be due to electrons tunneling into a Landau level in the well and scattering into another Landau level with a LO phonon emission.

4.2 Pseudomorphic $\text{Al}_{.4}\text{Ga}_{.6}\text{As}/\text{In}_{.1}\text{Ga}_{.9}\text{As}$ RTD

One of the pm-RTD structures studied in this research is presented and its performance is compared to the lattice matched RTDs using the same experimental approach discussed in the previous section. The pm-RTD consists of the following layers, in order of growth from the n^+ GaAs substrate : 1.0 μm of $n = 2E18 \text{ cm}^{-3}$ GaAs buffer layer, 500 Å of undoped GaAs spacer, 85 Å of $\text{Al}_{.4}\text{Ga}_{.6}\text{As}$ barrier, 50 Å of undoped $\text{In}_{.1}\text{Ga}_{.9}\text{As}$ well, 85 Å of undoped $\text{Al}_{.4}\text{Ga}_{.6}\text{As}$ barrier, 500 Å of undoped GaAs spacer and 0.4 μm of $n = 2E18 \text{ cm}^{-3}$ top contact layer.

4.2.1 I-V Characteristics

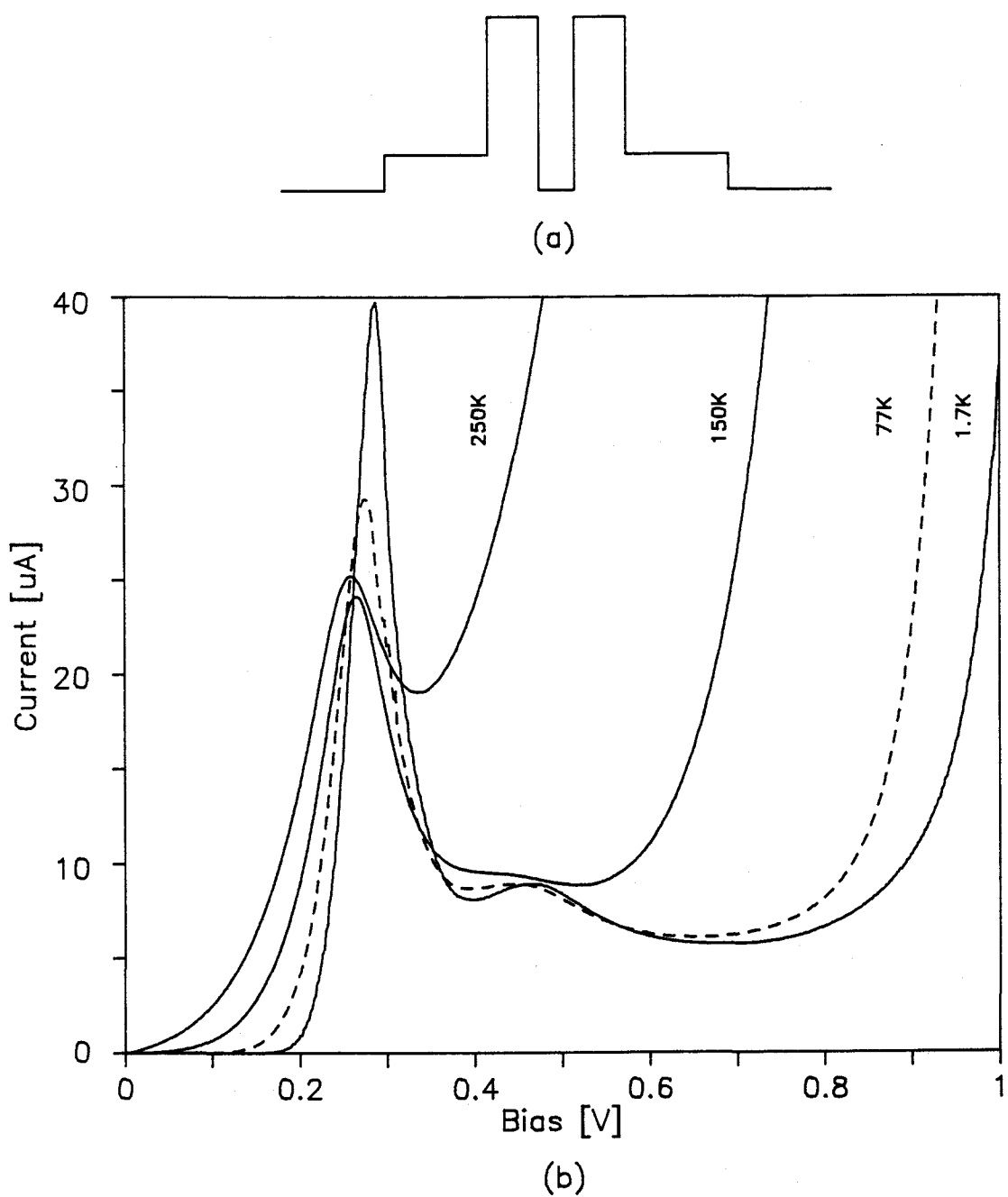


Figure 4.5: Pseudomorphic $\text{Al}_{0.4}\text{Ga}_{0.6}\text{As}/\text{In}_{0.1}\text{Ga}_{0.9}\text{As}$ RTD. (a) Conduction band profile. (b) I-V characteristics measured at 250, 150, 77, and 1.7 K.

Figure 4.5 (a) and (b) respectively show the CB edge and the I-V characteristics of the pm-RTD measured at several different temperatures. This RTD shows similar trends to the previous lattice matched AlAs/GaAs RTD. The PVCRs of the RTD are 7, 5, 2.7, and 1.3 with corresponding (I_p, I_v) of (39.8, 5.7), (29.2, 6), (24.1, 8.8), and (25.2, 19) μA 's at temperatures of 1.8, 77, 150, and 250 K, respectively. The peak voltage, V_p shifts slightly towards a higher value at lower temperature, which was not observed in the AlAs/GaAs RTD. This is due to a 1000 Å thick spacer layer which increases the series resistance at lower temperature. This RTD also exhibits phonon assisted tunneling features in the valley region of the I-V curve.

Figure 4.6 displays the I-V characteristics of the pm-RTD measured at 1.8 K for $B = 8$ T (solid line) and 0 (dashed line) field. It is interesting to compare the I-V characteristics of the pm-RTD with the lattice matched AlAs/GaAs RTD discussed previously. Similar trends are observed such as the enhancement of the POCR at higher magnetic field and the existence of an LO phonon satellite peak in the valley region of the I-V curve whose peak height is also enhanced with increased magnetic field. In the pseudomorphic case however, no additional peaks in the valley region of the I-V curve were observed up to 8.5 Tesla.

The POCR's of the RTD are 8:1 and 7:1 at 8 T and 0 field, respectively. The magnetic field applied perpendicular to the barrier gives rise to sharp peaks in the density of states. The sharp density of states increases the electron population in the well at resonance and in the accumulation layer of the emitter off resonance [69]. This explains the enhancement of the POCR and LO phonon satellite peak under

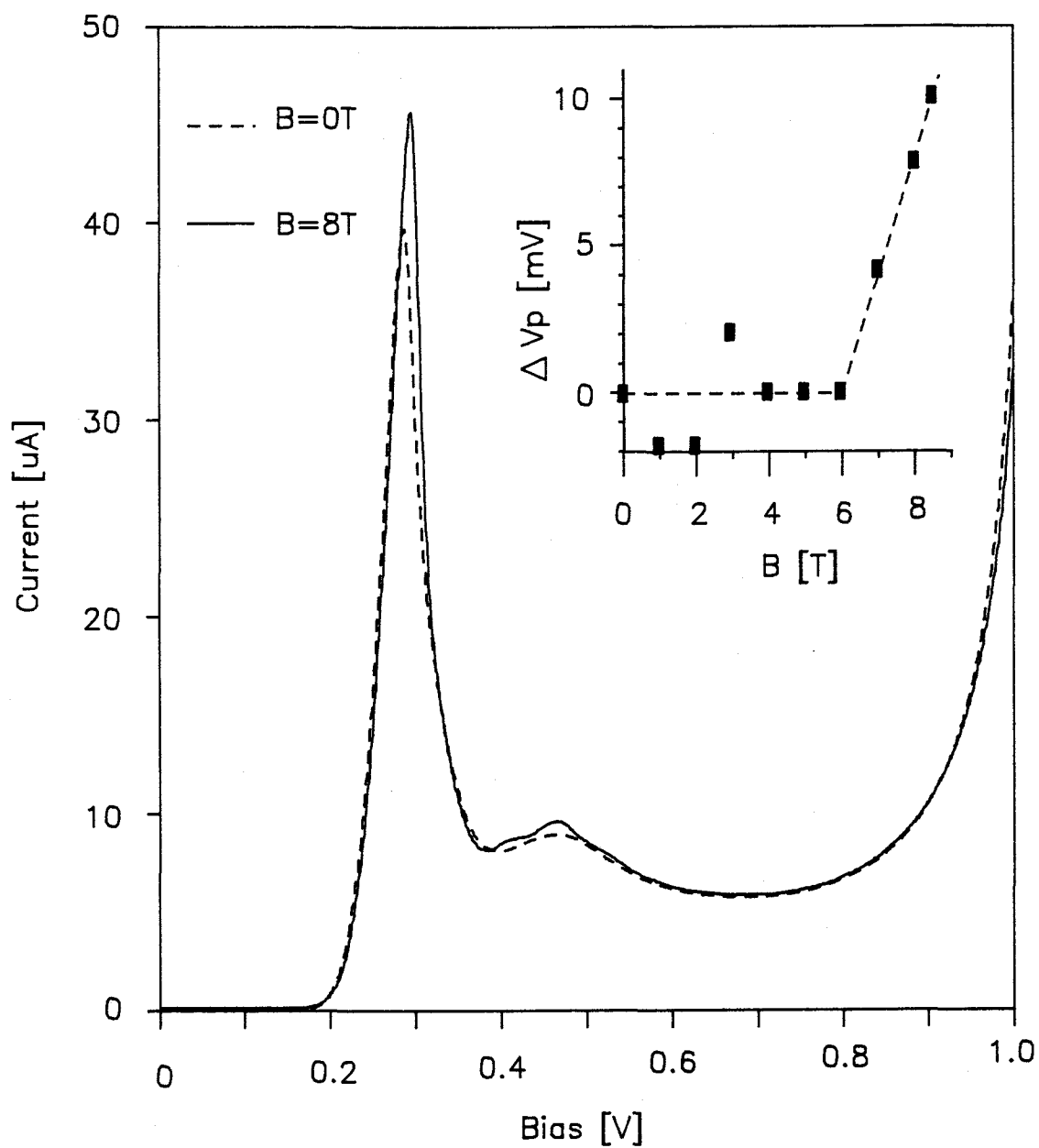


Figure 4.6: I-V characteristics of the pseudomorphic $\text{Al}_{0.4}\text{Ga}_{0.6}\text{As}/\text{In}_{0.1}\text{Ga}_{0.9}\text{As}$ RTD at 1.8 K. The solid and the dashed lines are for $B = 8$ Tesla ($B \parallel J$) and 0 field, respectively. The inset figure shows ΔV_p as a function of magnetic field. $\Delta V_p = V_p(B) - V_p(B=0)$.

magnetic field. The same phenomenon was also reported by Eaves [64].

The occurrence of no additional subsidiary peaks except the LO phonon peak in the valley region of the I-V curve is believed to be due to the presence of the InGaAs in the well. InGaAs grown on GaAs substrates tends to increase the random alloy scattering due to surface segregation and interface roughness scattering due to evaporation of indium [53]. Scattering in the InGaAs well makes the mean free path of an electron smaller than the cyclotron orbital length, which makes the energy separation between the Landau levels in the InGaAs well unresolvable. Thus, there are no additional peaks present even at 8 Tesla.

The separation in bias voltage between the V_p and the LO phonon peak is 167 mV and the LO phonon energy of the $\text{In}_{0.1}\text{Ga}_{0.9}\text{As}$ is 36 meV [70]. Thus the ratio of the voltage drop between the lowest bound state in the accumulation layer of the emitter and the half well width, δ , is 0.22. The smaller δ of this device compared to the previous lattice matched AlAs/GaAs RTD is due to the much wider spacer and barrier thicknesses causing a smaller portion of the applied voltage to drop across the two layers.

The non-linear behavior of the V_p shift and stationary behavior of the LO phonon satellite peak as a function of magnetic field are observed in both samples. The main resonance peak changes nonlinearly while the LO phonon peak does not change with the magnetic field applied perpendicular to the barrier. The inset of Figure 4.6 shows the main resonance peak change of the $\text{pm-Al}_{0.4}\text{Ga}_{0.6}\text{As}/\text{In}_{0.1}\text{Ga}_{0.9}\text{As}$ RTD as a function of the magnetic field. The closed squares are the measured values of $\Delta V_p (= V_p(B) - V_p(0))$ and the dashed line is a result of a two

step piecewise linear fit. The peak voltage, V_p of the pm-Al_{0.4}Ga_{0.6}As/In_{0.1}Ga_{0.9}As RTD increases linearly above 6 Tesla and shows oscillatory behavior below 6 Tesla. Similar behavior was also observed in the lattice matched AlAs/GaAs RTD. The interesting behavior of ΔV_p as a function of magnetic field is not well understood at present.

4.2.2 Shubnikov-de Haas Measurement

Magneto-quantum oscillations of the pm-Al_{0.4}Ga_{0.6}As/In_{0.1}Ga_{0.9}As RTD at three different biases are shown in Figure 4.7. The oscillations are measured in the same way as for the lattice matched AlAs/GaAs RTD described previously. The oscillations show a single period in $1/B$; B_f 's are 13.2, 14.3, and 16.2 Tesla for applied biases of 0.90, 0.95, and 1.0 volts. The oscillations are due to the Fermi level of the emitter contact passing through the Landau levels of the accumulation layer of the emitter side. These oscillations are thought to be evidence of a two dimensional quasi-bound state in the accumulation layer of the emitter.

The oscillation periods, which are comparable to those of the AlAs/GaAs RTD, suggest that the doping concentration at the emitter contact of the two RTDs are comparable which is consistent with the fabrication parameters. The increased scattering in the InGaAs well broadens the density of state and makes the energy separation between the Landau levels unresolvable. Thus, the LO phonon assisted tunneling features in magneto-quantum oscillations are suppressed [71].

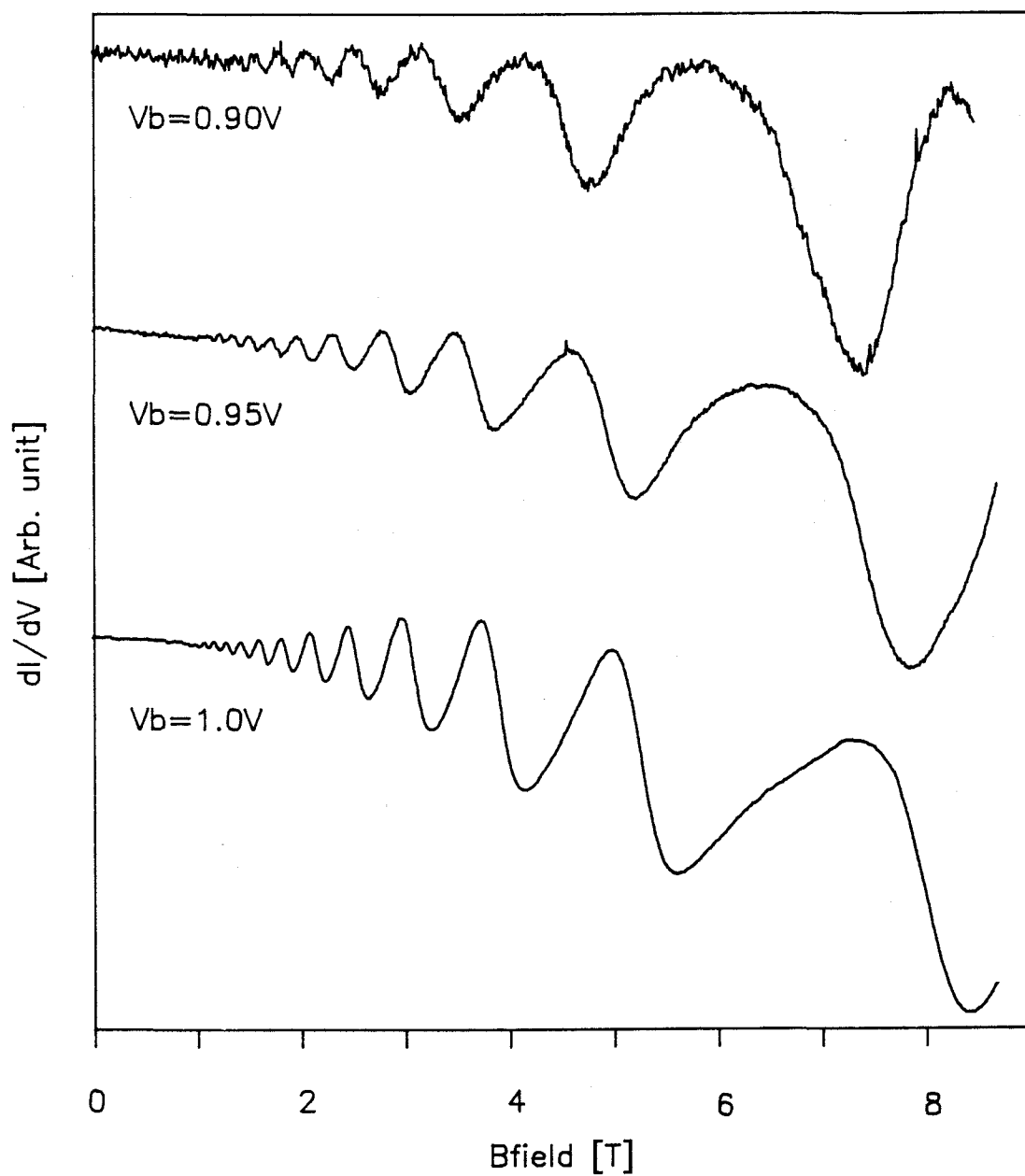


Figure 4.7: Differential conductance of the pseudomorphic $Al_{0.4}Ga_{0.6}As/In_{0.1}Ga_{0.9}As$ RTD as a function of magnetic field ($B||J$) at $V_{bias} = 0.90, 0.95,$ and 1.0 V.

5. Experimental Results and Analysis II

In this chapter, the effect of increasing spacer layer thickness on both lattice-matched AlGaAs/GaAs and pm-AlGaAs/InGaAs RTDs is discussed. It is generally believed that a thick spacer layer adjacent to the barrier improves the peak to valley current ratio (PVCR) by reducing ionized impurity scattering; however, as shown here, the performance of the AlGaAs/GaAs RTDs degrades for spacer layers greater than a certain critical width. The thickness of the symmetric spacer layers in the pm-AlGaAs/InGaAs RTDs was found to have a strong influence on tunneling currents which can be explained by space charge effects at the leading and trailing edges of the diode.

5.1 Analysis of the Spacer Layer

The influence of the spacer layers in equilibrium is considered theoretically by solving the n^+ - n homojunction model as shown in Figure 5.1 (a). Electrons thermally generated from the heavily doped n^+ contact layer diffuse into the undoped layer until the electro-static potential balances the carrier diffusion process. The continuity equation at thermal equilibrium is

$$J = nq\mu\epsilon + qD_n \frac{dn}{dz} = 0. \quad (5.1)$$

From the Einstein relationship, $D/\mu = KT/q$, Eq. (5.1) yields

$$-\frac{q}{KT} \epsilon = \frac{1}{n} \frac{dn}{dz} \quad (5.2a)$$

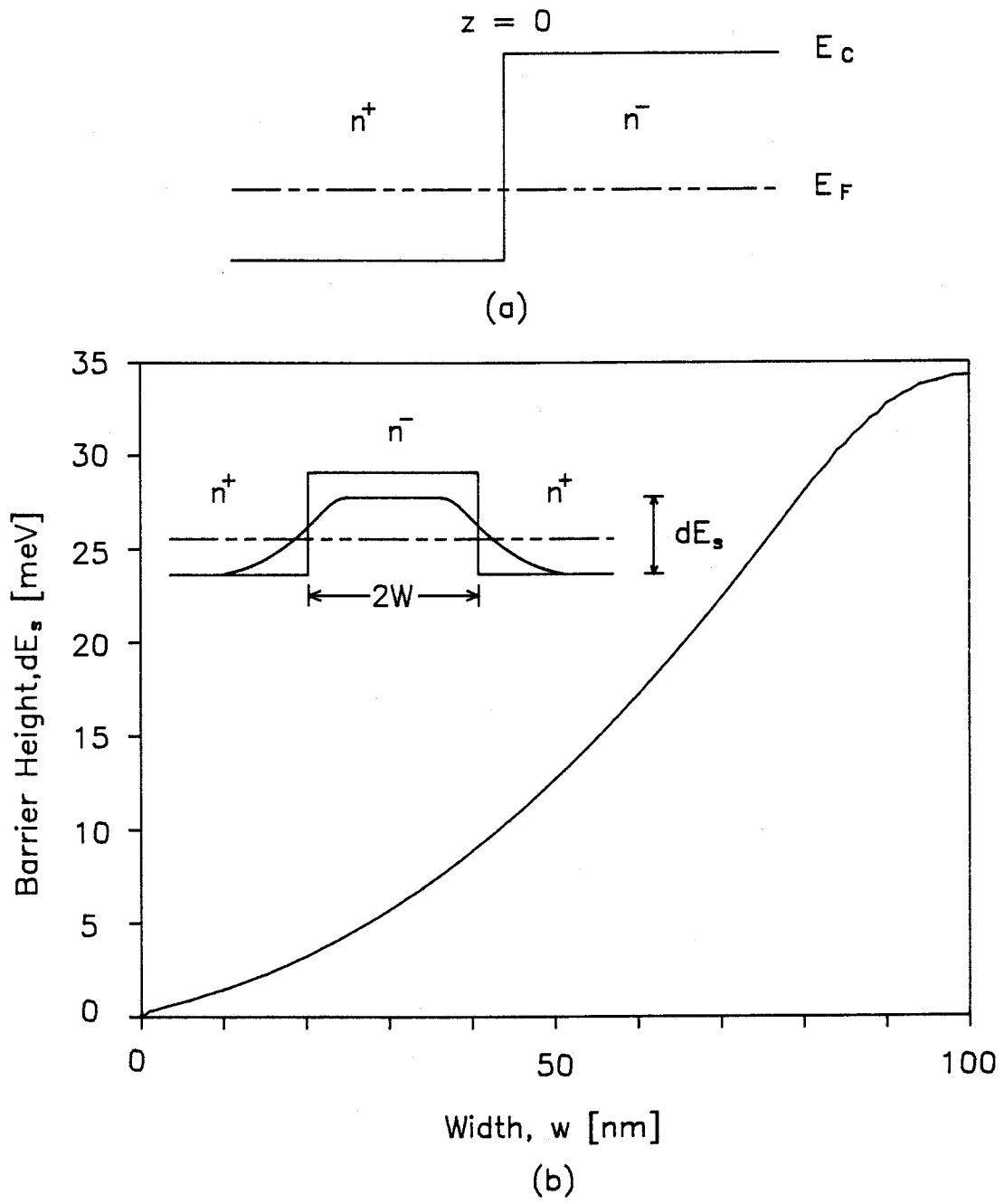


Figure 5.1: Analysis of the spacer layer. (a) $n^+ - n^-$ homojunction. (b) Spacer barrier height, dE_s in an $n^+ - n^- - n^+$ homojunction.

$$-\frac{q}{KT} \int^z \epsilon dz = -\frac{q}{KT} \int^z \frac{dV}{dz} dz = -\frac{q}{KT} V(z) \quad (5.2b)$$

$$\int^z \frac{1}{n} \frac{dn}{dz} dz = \int^{n(z)} \frac{1}{n} dn = \ln [n(x)] + C. \quad (5.2c)$$

Thus,

$$n(z) = C \exp [-qV(z)/KT]. \quad (5.3)$$

The constant C in Eq. (5.3) is determined to be N_1 because $n(-\infty) = N_1 = C$. The net charge $\rho(z) = [N(z) - n(z)]$, where $N(z)$ and $n(z)$ are fixed charges (from intentional or unintentional dopant) and free charges at position z , respectively. The electric field $\epsilon(z)$ expressed in terms of the net charge density $\rho(z)$ is

$$\epsilon(z) = \int^z \frac{\rho(z)}{\epsilon_s} dz. \quad (5.4)$$

After some rearrangement of Eq. (5.4),

$$\epsilon d\epsilon = \frac{dV}{dz} \frac{\rho(z)}{\epsilon_s} dz = \frac{\rho(z)}{\epsilon_s} dV. \quad (5.5)$$

Integration of Eq.(5.5) yields,

$$\begin{aligned} \frac{1}{2} \epsilon^2(z) &= \frac{q}{\epsilon_s} \int_{V=0}^{V(z)} \left[N(z) - N_1 \exp\left(-\frac{qV(z)}{KT}\right) \right] dV \\ &= \frac{q}{\epsilon_s} \left[A(z) + \frac{KT}{q} N_1 \left\{ \exp\left[-\frac{qV(z)}{KT}\right] - 1 \right\} \right] \end{aligned} \quad (5.6a)$$

where

$$A(z) = \begin{cases} N_1 V(z) & z \leq 0 \\ N_1 V(0) + N_2 [V(z) - V(0)] & z \geq 0 \end{cases} \quad (5.6b)$$

The boundary conditions at $z = \infty$ are $V(z) = V_{bi}$ and $\epsilon(z) = 0$, where $V_{bi} = (KT/q) \ln(N_1/N_2)$. Thus potential $V(z)$ at the junction is

$$V(0) = \frac{1}{N_1 - N_2} \left[\frac{KT}{q} N_1 \left\{ 1 - \exp\left(-\frac{qV_{bi}}{KT}\right) \right\} - N_2 V_{bi} \right] \quad (5.6c)$$

The CB profile $V(z)$ is obtained by solving Eq. (5.6) for an entire range which satisfies $\epsilon^2(z) \geq 0$. The carrier concentration $n(z) = N_1 \exp[-qV(z)/KT]$. The CB profile with a $n^+ - n - n^+$ double homojunction width of w can be solved by a similar procedure. However, V_{bi} is expressed as in Eq. (5.7) in analogy to the metal-semiconductor-metal (MSM) structure [73], instead of $(KT/q) \ln(N_1/N_2)$,

$$V_{bi} = \frac{qN_1^+}{8\epsilon_s} w^2. \quad (5.7)$$

The spacer barrier, dE_s at thermal equilibrium is obtained by solving Eq. (5.4) numerically. The resulting conduction band barrier, dE_s at 77 K with N_1 of $1 \times 10^{18} \text{ cm}^{-3}$ and N_2 of 5×10^{15} is plotted in Figure 5.1 (b). As shown in the figure, dE_s becomes increasingly important as the undoped spacer layer thickness increases and it will be shown that its effect also cannot be neglected in device analysis. The primary effects of increasing the spacer layer thickness are a shift in the peak voltage position due to increasing series resistance of the device and reduction in the current through the device. Experimental results of spacer layer thickness effects on the lattice matched and pseudomorphic RTDs are discussed in the following.

5.2 Lattice Matched RTD

The lattice-matched configuration used in this work consists of $\text{Al}_{.35}\text{Ga}_{.65}\text{As}/\text{GaAs}$ RTDs with symmetric 50, 500 and 1000 Å spacer layers. All three RTDs have the same structural parameters except for the spacer layer thickness. The RTDs consist of the following layers in order of growth from the n^+ GaAs substrate: 1.0 μm of silicon $1 \times 10^{18} \text{ cm}^{-3}$ doped GaAs buffer layer, an undoped GaAs spacer layer (50, 500, or 1000 Å), 85 Å of undoped $\text{Al}_{.35}\text{Ga}_{.65}\text{As}$ barrier, 50 Å undoped GaAs well, 85 Å undoped $\text{Al}_{.35}\text{Ga}_{.65}\text{As}$ barrier, an undoped GaAs spacer layer (50, 500, or 1000 Å), and finally a silicon $1 \times 10^{18} \text{ cm}^{-3}$ doped 4000 Å top contact layer.

5.2.1 I-V Characteristics

The CB profile, including the spacer layer at zero bias, is shown in the left inset of Figure 5.2, where the dashed line indicates the metallurgical junction. The I-V characteristics shown in the figure are for $\text{Al}_{.35}\text{Ga}_{.65}\text{As}/\text{GaAs}$ RTDs with 3 different spacers at 77 K. The PVCR of these devices are 5, 11 and 10:1 for spacer layers of 50, 500 and 1000 Å, respectively. Increasing the spacer layer thickness results in higher series resistance which shifts the peak and valley voltage (V_p , V_v) to higher values. The smaller PVCR in the 50 Å spacer RTD is believed to be due to ionized impurity scattering from the emitter and collector regions. Such scattering decreases the peak transmission probability and broadens the resonance energy, thus lowering the PVCR.

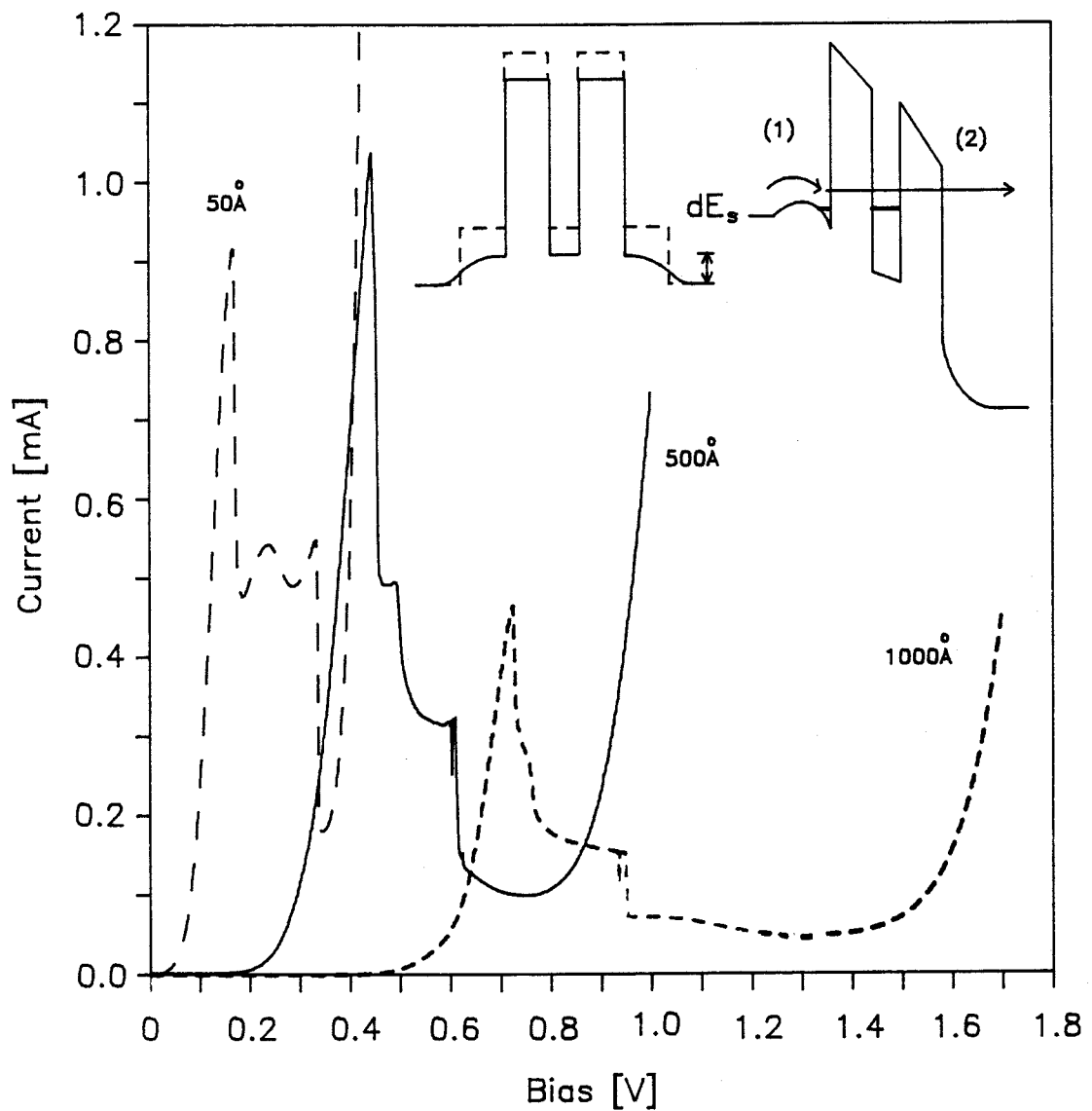


Figure 5.2: I-V characteristics of lattice matched AlGaAs/GaAs RTDs with 50, 500, and 1000 Å thick spacer layers measured at 77K. The solid and dashed lines in the left inset signifies the CB profile at thermal equilibrium and metallurgical junction, respectively. The right inset figure shows a two step conduction process for electrons with below spacer barrier height energy dE_s .

The current density through the RTD expressed in Eq. (4.15) is repeated here for convenience.

$$J = \frac{em^*KT}{2\pi^2\hbar^3} \int_0^\infty T^*T \ln \left(\frac{1 + \exp[(E_f - E_L)/KT]}{1 + \exp[(E_f - E_L - eV)/KT]} \right) dE_L \quad (5.8)$$

As the spacer layer becomes thicker, the effective spacer barrier height, dE_s , increases, and the tunneling probability of an electron, $T(E)$, with its energy below dE_s becomes smaller. Thus the lower limit of integration in Eq. (5.8) increases from 0 to ϵ below which $T(\epsilon)$ is negligible because of the formation of a triple barrier. A two step conduction process is required for electrons below ϵ to reach the collector contact from the emitter contact. The first step is either thermionic emission over or tunneling across the emitter spacer barrier, followed by tunneling through the rest of the double barrier structure as the second step as shown in the right inset of Figure 5.2. Thus, current through the RTD with a 1000 Å spacer layer is smaller than that with a 500 Å while the PVC's of the two RTDs are comparable.

If it is assumed that the spacer layer is thick enough so that ionized impurity scattering is negligible in the tunneling region of the device, and that inelastic (LO or acoustic phonon) scatterings are infrequent, then current through RTDs with a different spacer layer thickness can simply be compared by the following equation.

$$J_1/J_2 \approx \frac{\int_{\epsilon_1}^\infty T^*T \ln \left(\frac{1 + \exp[(E_f - E_L)/KT]}{1 + \exp[(E_f - E_L - eV)/KT]} \right) dE_L}{\int_{\epsilon_2}^\infty T^*T \ln \left(\frac{1 + \exp[(E_f - E_L)/KT]}{1 + \exp[(E_f - E_L - eV)/KT]} \right) dE_L} \quad (5.9)$$

where J_1/J_2 is a ratio of current density between the two different spacer layer thicknesses and ϵ_1 and ϵ_2 are the lowest electron energies needed for tunneling through the spacer barrier width of w_1 and w_2 , respectively. Eq. (5.9) can be further reduced to the following if $E_f - eV$ is larger than 3 ~ 4 times KT .

$$J_1/J_2 \approx \frac{\int_{\epsilon_1}^{\infty} T^* T \ln \{1 + \exp[(E_f - E_L)/KT]\} dE_L}{\int_{\epsilon_2}^{\infty} T^* T \ln \{1 + \exp[(E_f - E_L)/KT]\} dE_L} \quad (5.10)$$

Figure 5.3 shows the normalized I-V characteristics of the $Al_{.35}Ga_{.65}As/GaAs$ RTDs. The I-V characteristics are normalized in such a way that each V_p and I_p are aligned. The RTD with a 500 Å spacer layer showed ~ 2.8 times more peak and valley current than that with a 1000 Å spacer layer. The normalized I-V characteristics in Figure 5.3 show a linear scaling of the peak and valley currents between two RTDs with 500 (broken line) and 1000 Å (solid line) thick spacer layer that show comparable PVCs. Thus the current through RTDs with the same structural parameters except for the spacer layer thickness can be estimated using Eq. (5.10) if the previous assumptions are valid.

There exists a critical spacer layer width, above which thermionic emission over the emitter spacer layer barrier becomes the rate limiting transport process leading to suppression of the tunnel current. The reduction in the peak current density depends on the barrier which exists when the structure is biased at resonance, and hence the critical width depends on dE_s and the position of the resonance energy in relation to the Fermi energy at zero bias. Since

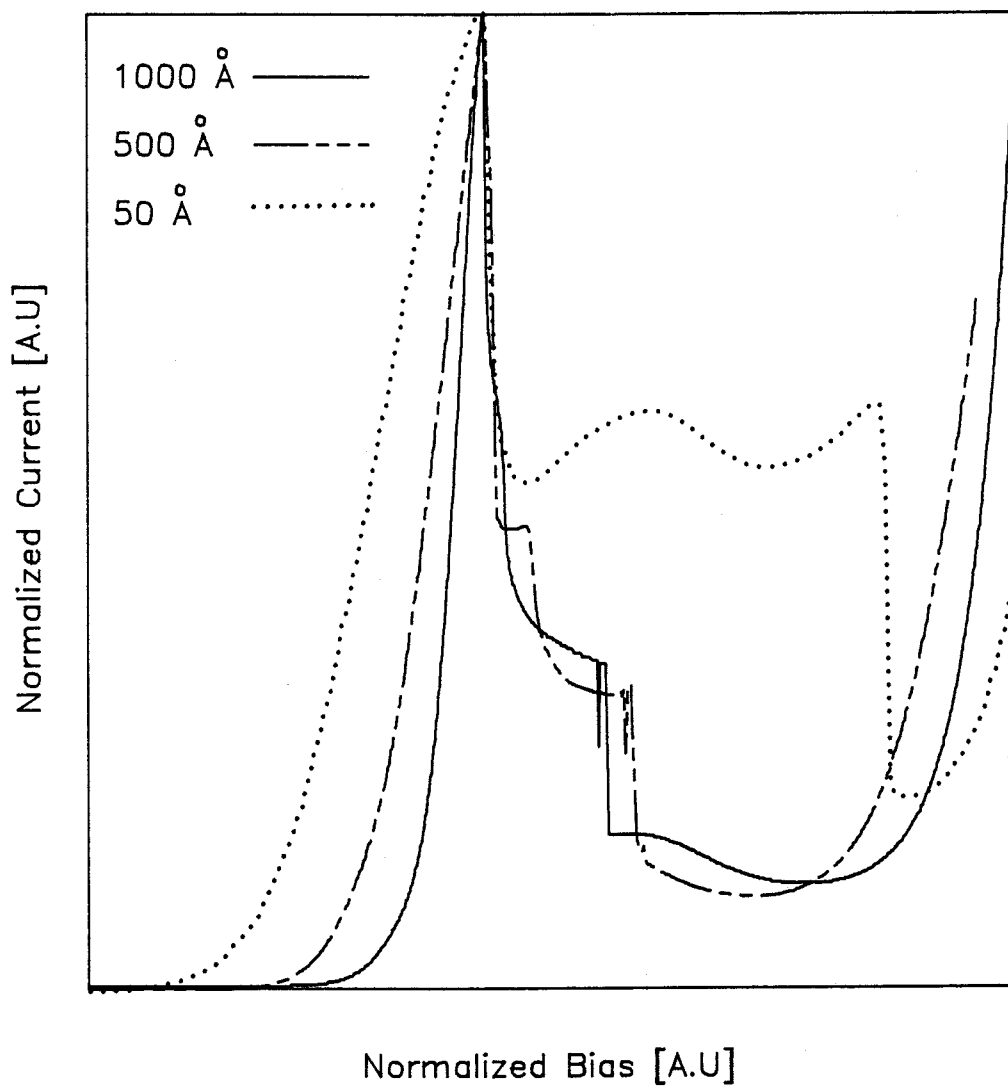


Figure 5.3: Normalized I-V characteristics of the lattice matched AlGaAs/GaAs RTDs. The I-V curves are normalized in a way that the peak voltage and the peak current of all RTDs are aligned at one point.

the emitter spacer barrier height is reduced in forward bias, a higher resonance energy implies a greater reduction in the effective barrier at resonance, and thus the critical spacer width is increased. Below the critical width, the current density and PVCR continue to improve with increasing spacer layer thickness. Above this critical width, the current is reduced, which is evident in the comparison of the I-V characteristics between the 500 Å and the 1000 Å spacer RTDs although the PVCRs are comparable. The exact determination of the optimum spacer layer thickness for maximum PVCR is complicated by the trade-off between improved performance due to the reduction in impurity scattering and to decreased performance through suppression of the tunnel current due to the emitter spacer barrier.

The role of the spacer layer becomes more dramatic when the allowed state(s) in the well lie far below the Fermi level in the contact layer, since electrons from the contact layer can tunnel into a quasi-bound state in the well even at thermal equilibrium. This situation can be realized by placing an InGaAs layer in the well since it has a negative CB offset.

5.2.2 Magnetic Field Analysis

Application of a magnetic field normal to the barrier quantizes the energy levels in the plane parallel to the barrier as discussed in the previous chapter. Figure 5.4 shows data illustrating the influence of the magnetic field on lattice matched RTDs with 500 Å symmetric spacer layers adjacent to the tunnel barriers. The RTDs with 50 Å thick spacer layers did not show any noticeable difference in I-V

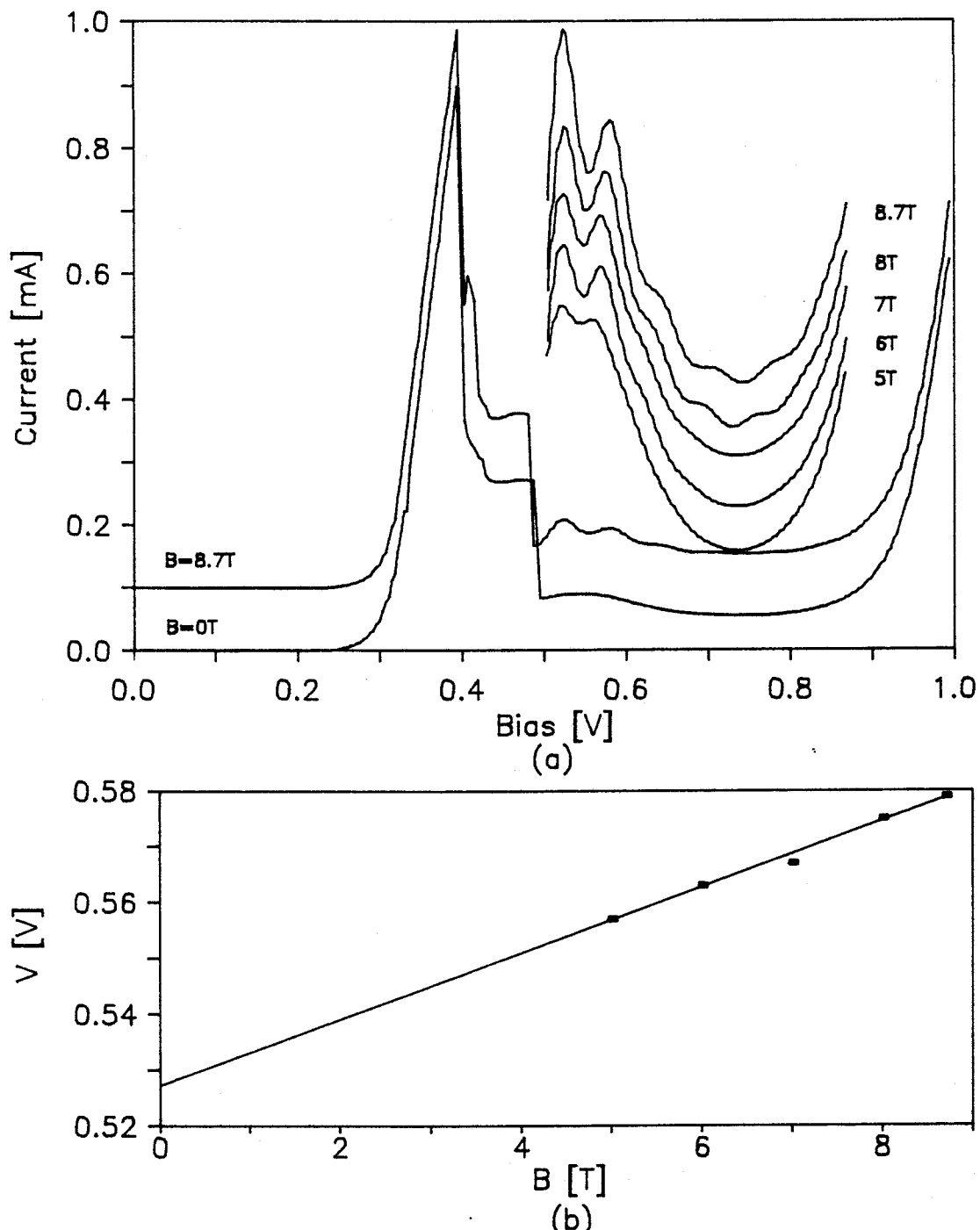


Figure 5.4: Influence of the magnetic field on lattice matched AlGaAs/GaAs RTD with 500 Å thick spacer layer. (a) I-V characteristics measured at 1.8 K with ($B = 8.7T$) and without magnetic field ($B \parallel J$). The inset figure shows magnified I-V curves in the valley region with different magnetic fields. (b) Change of the second satellite peak position in (a) as a function of magnetic field. The straight line is a result of a least-squares fit.

characteristics up to a magnetic field of 8.7 Tesla; that is believed due to the high scattering rate in the active region of the RTD.

The RTD with a 500 Å spacer layer shows a number of satellite peaks which become stronger with increasing magnetic field in the valley region of the I-V curve as shown in Figure 5.4 (a). The inset of Figure 5.4 (a) shows magnified I-V characteristics in the valley region at different magnetic fields. The first satellite peak does not change its peak position as the magnetic field changes whereas the rest of the peaks do. The first peak is believed to be due to LO phonon assisted tunneling and the rest of the peaks are due to electron tunneling into one of the Landau levels in the well with LO phonon emission. The straight line in Figure 5.4 (b) is a least-squares fit of the second satellite peak position as a function of magnetic field ($B \parallel J$). The line intercepts at 0.527 V for $B = 0$, which closely matches the LO phonon peak position at 0.523 V. This result is good evidence of inelastic tunneling with emission of an LO phonon between the two different Landau levels.

The density of states function in the presence of a quantizing magnetic field is given by [74]

$$g(E)dE = \frac{1}{4\pi^2} \left(\frac{2m^*}{\hbar^2} \right)^{3/2} \frac{\hbar eB}{m^*} \sum_{n=0}^{n_{\max}} \left[E - (2n+1) \frac{\hbar\omega_o}{2} \right]^{-1/2} dE \quad (5.11)$$

where $g(E)dE$ gives the number of states lying between E and $E + dE$ and n_{\max} is defined by

$$(2n_{\max}+3)\hbar\omega_o/2 > E > (2n_{\max}+3)\hbar\omega_o/2. \quad (5.12)$$

The variation of $g(E)$ with E in Eq. (5.11) is illustrated in the solid line of Figure 5.5, whereas the dotted line represents the density of

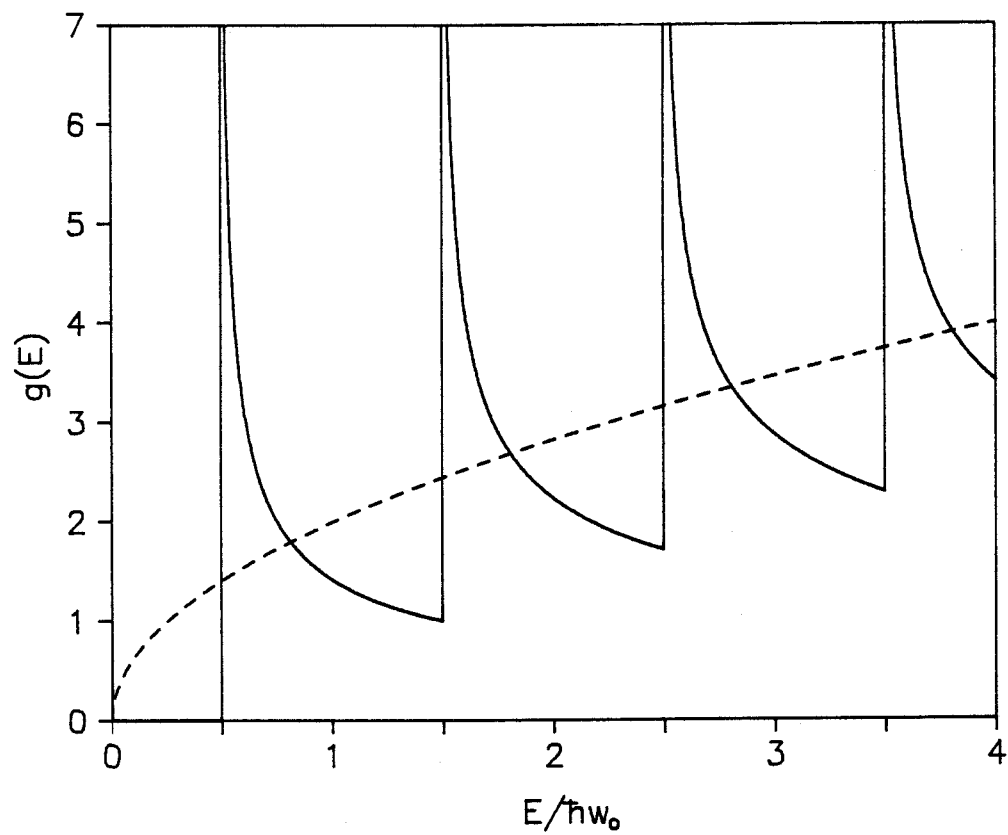


Figure 5.5: Density of states under a quantizing magnetic field. The dashed line represents a density of states in the absence of a magnetic field.

states without an applied magnetic field. It is seen from Eq. (5.11) that the density of states function is zero for values of E up to $\hbar\omega_0/2$ and becomes infinity at the points $E = (2n+1)\hbar\omega_0/2$. The periodic increase in the value of the density of states is the origin of the various oscillatory phenomena at high magnetic field as well as the observed enhancements of the satellite peaks. If the magnetic field is sufficiently weak such that $\hbar\omega_0$ is less than E_F , then the relative position of E_F from the CB minimum can be assumed to be the same as in the case without magnetic field. Then the number of occupied Landau levels below E_F decreases while total number of electrons must remain constant, and there is an enhancement of electrons in each level with higher magnetic field. Thus the satellite peaks in the valley region of the I-V curve become stronger with increasing magnetic field.

In magnetic fields, the RTD with a 1000 Å thick spacer layer shows similar but less pronounced effects than that with a 500 Å spacer. Figure 5.6 shows the influence of a magnetic field applied normal to the barriers ($B \parallel J$) on an RTD with 1000 Å symmetric spacer layer adjacent to tunnel barriers. The data in Figure 5.6 (b) show oscillations in the differential conductance in a valley region of I-V curves. Similarities between the two samples (Fig. 5.4 and 5.6) under a quantizing magnetic field are observed in the stationary and non-stationary behavior of the first and subsequent satellite peaks. The straight line in the inset of Figure 5.6 (a) is a least-squares fit of the second satellite peak position in Figure 5.6 (b) as a function of magnetic field ($B \parallel J$). The line intercepts at 0.956 V when $B = 0$ T which is the LO phonon peak position. The similarity in behavior of this device to the 500 Å spacer RTD under the influence of a quantizing

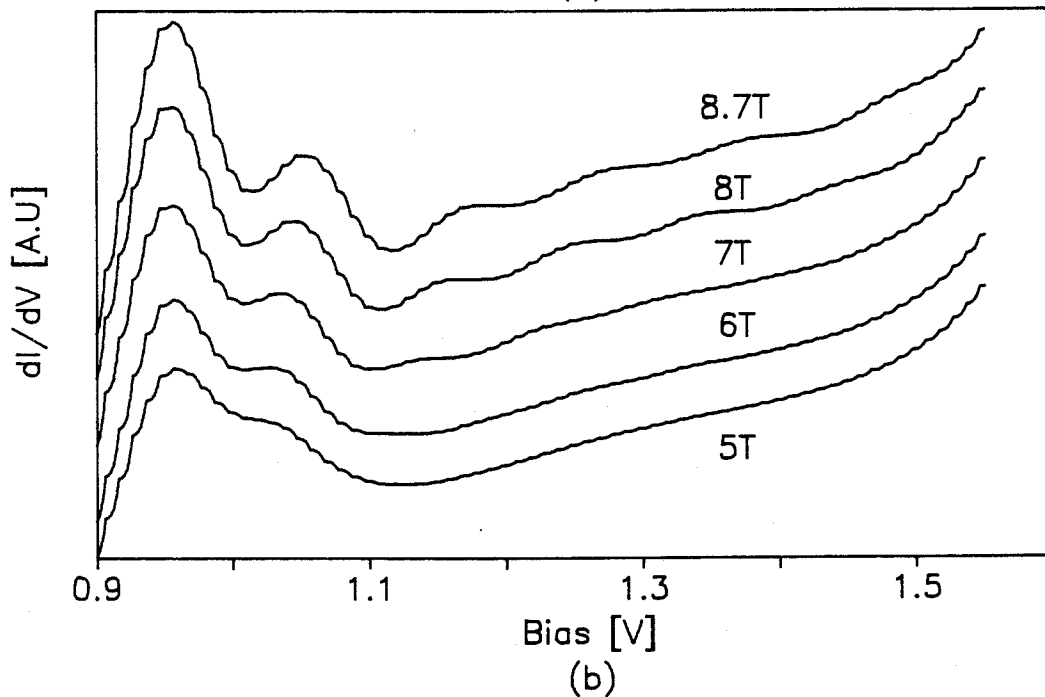
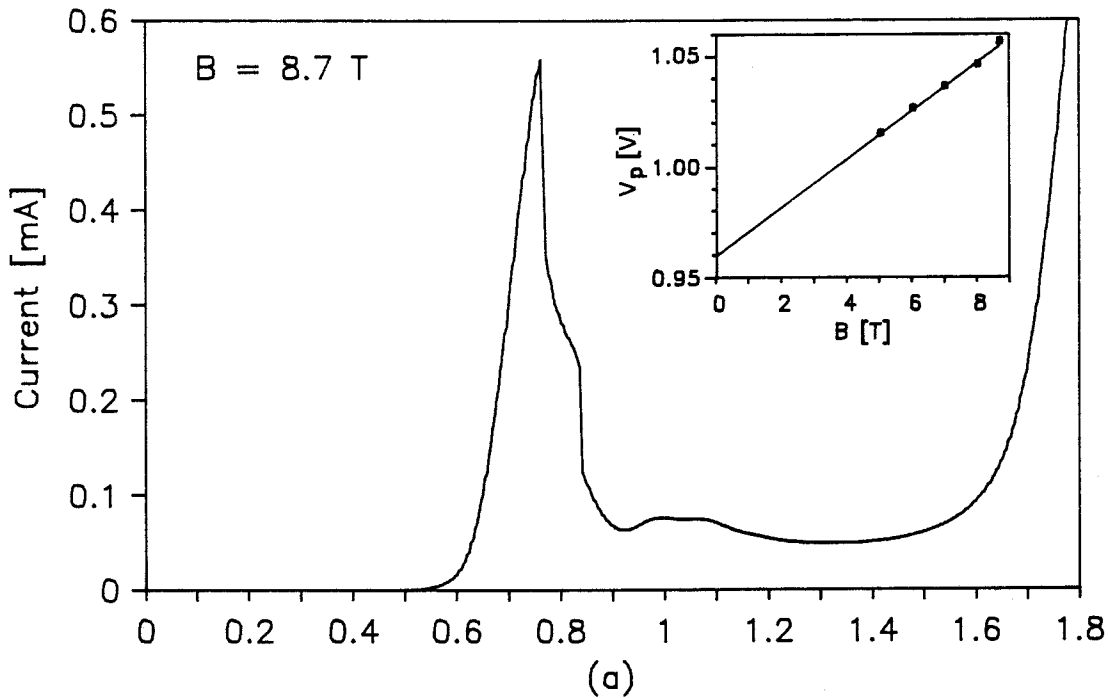


Figure 5.6: (a) I-V characteristics of the AlGaAs/GaAs RTD with a 1000 Å thick spacer layer measured at 1.8 K with a magnetic field $B = 8.7$ Tesla ($B \parallel J$). The inset figure shows the second satellite peak position as a function of magnetic field shown in (b). (b) Differential conductance of the RTD in the valley region of the I-V curve with magnetic field.

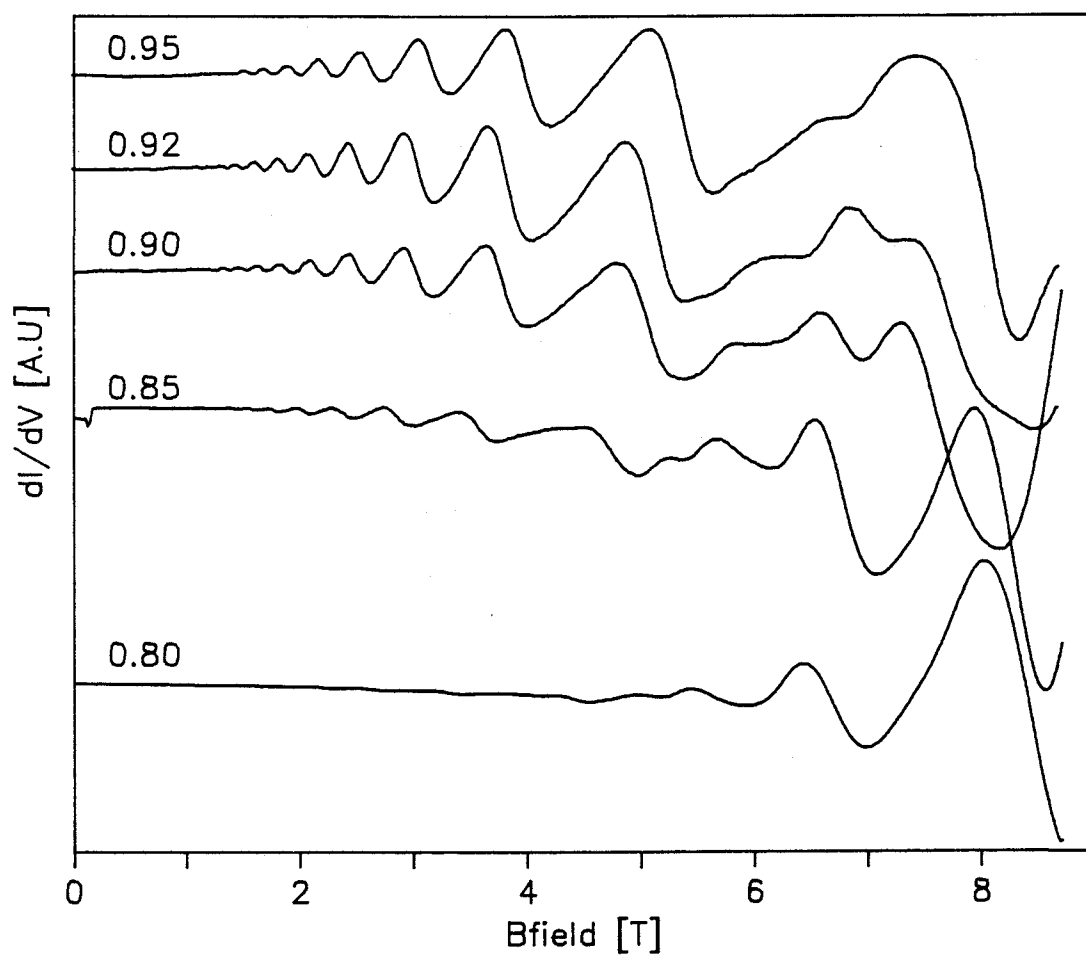
magnetic field can be explained in the same manner.

The effect of the increasing spacer layer thickness on device performance under magnetic field is similar to that described for the electric field alone. The I-V characteristics of the RTD in the valley region shows a significant enhancement of structural features as the spacer layer thickness changes from 50 to 500 Å. These features are reduced for 1000 Å spacer layers for the following reason. The mean free time between scattering events in tunneling region of the RTD is γ , then the mean free path length is $L = v\gamma$, where v is the velocity of electron. The probability that an electron has not made a collision at time t is given by $\exp(-t/\gamma)$ [75]. The average value of time $\langle t \rangle$ between collisions is given by

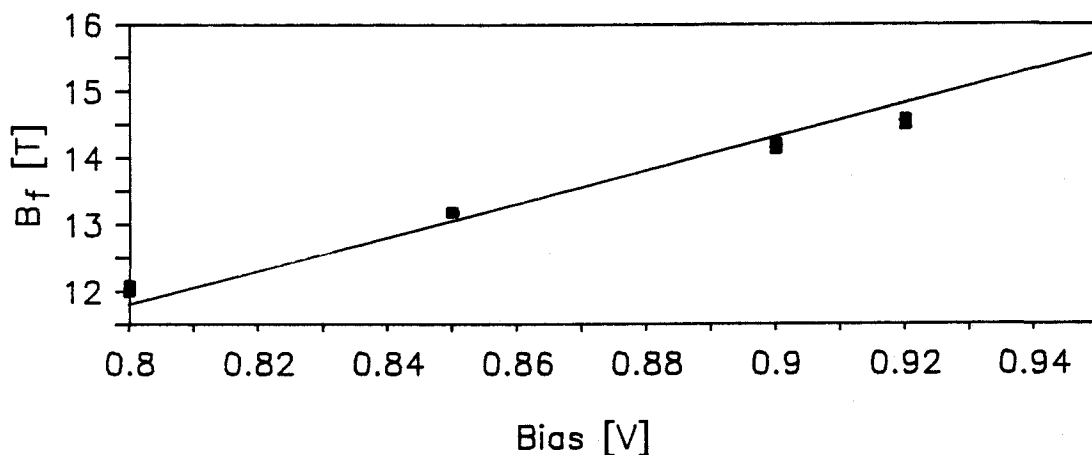
$$\langle t \rangle = \gamma^{-1} \int_0^{\infty} t \exp[-t/\gamma] dt = \gamma \quad (5.13)$$

Eq. (5.13) shows γ is just the mean free time as defined above. The mean free path L is given by $L(v) = v\gamma(v)$. Then the probability that an electron experiences a collision while traveling the tunneling region width of L_T is given by $1 - \exp[-L_T/v\gamma]$. Enhancement of magneto-tunneling features from the 50 to 500 Å thick spacer layer devices is due to a substantial reduction of scattering in the tunneling region of the RTD. If the same values of v and γ are assumed for RTDs with a 500 and 1000 Å spacer layer thickness, electrons in the latter have a higher probability of scattering before completing the tunneling process which will reduce the magnitude of the magneto-tunneling features. Scattering in the tunneling region smears the magnetic energy quantization and results in undetectable features in the extreme limit.

Figures 5.7 (a) and (b) show the SdH oscillation data and the



(a)



(b)

Figure 5.7: (a) Shubnikov-de Haas oscillations obtained from the AlGaAs/GaAs RTD with a 500 Å thick spacer layer. Numbers in the figure represent the applied bias. (b) SdH oscillation period, B_f , as a function of applied bias. $B_f = [\Delta(1/B)]^{-1}$.

corresponding periodicity in $1/B$ ($B_f = [\Delta(1/B)]^{-1}$) obtained from RTDs with 500 Å spacer layers. The device was biased in the valley region of the I-V characteristics. The RTD with a 1000 Å spacer layer showed much weaker oscillations than that with a 500 Å spacer and the period could not be determined.

SdH oscillations of the RTD with a 500 Å spacer layer show similar trends to those from the AlAs/GaAs RTD in chapter 4. They also exhibit multiple oscillations in $1/B$; one series of B_f below ~ 5 Tesla and another periodicity above ~ 7 Tesla with some transition region in between. The slope of lower series B_f as a function of bias voltage shown in Figure 5.7 (b) is 25.1 Tesla/Volt. The periodicity of the higher series B_f is not resolved up to magnetic fields of 8.7 Tesla because it shows less than one period under a given bias condition. If one assumes that, as before, the origin of the lower and the higher series B_f 's are due to the Fermi level in an accumulation layer of the emitter passing through successive Landau levels and resonant tunneling of electrons from one Landau level in the accumulation into another Landau level in the well with the emission of an LO phonon, B_f in each case is from Eq. (4.3)

$$B_f = \frac{m^*}{\hbar e} [E_F - E_{ao}] = \frac{m^*}{\hbar} \alpha V_a \quad (5.14a)$$

$$B_f = \frac{m^*}{\hbar e} [E_{ao} - E_{qo} - (\hbar\omega_L)] = \frac{m^*}{\hbar e} [\beta eV_a - (\hbar\omega_L)] \quad (5.14b)$$

where all the symbols have the same meaning as in chapter 4.

A proportional voltage drop of 6.9 % between E_F and E_{qo} of the RTD with a 500 Å thick spacer layer is obtained from the LO phonon peak position. $\alpha + \beta$ is the same as $(E_F - E_{qo})/V_a$. The slope of B_f as a function of applied bias in Figure 5.7 (b) is 25.1 Tesla/Volt which

yields α or β of 0.043 from Eq. (5.14). If α is 0.043, β has to be 0.026 or vice versa since the proportional voltage drop between E_F and E_{q0} is 6.9 %.

5.3 Pseudomorphic RTDs

The pm-RTD with symmetric spacer layers contains $\text{Al}_{.35}\text{Ga}_{.65}\text{As}$ barriers and an $\text{In}_{.2}\text{Ga}_{.8}\text{As}$ well with 50, 100, 250, 500, and 1000 Å symmetric spacer layers. Carrier transport through the device will obviously be affected when the ground state energy in the well lies below the CB edge of the spacer layer at zero bias as in AlGaAs/InGaAs devices. Based on a simple model for the resonance energy assuming an 85 % conduction band offset [76], the calculated ground state energy in the InGaAs well at zero bias lies slightly below the Fermi level as shown by the inset of Figure 5.8. To calculate this energy level in the well, the two dimensional carrier density (n_{2d}) in the well is assumed to be

$$n_{2d} = \sum_j KT g_j \ln [1 + \exp\{(E_F - E_j)/KT\}] \quad (5.15)$$

where j is quantum subband index, g_j is the two dimensional density of state at j th subband, and E_j is the energy of the j th quantum level in the well. By solving Poission's equation iteratively for n_{2d} , the conduction band (C.B.) profile at thermal equilibrium shown in Figure 5.8 is obtained. Due to the overall requirement of charge neutrality, the ground state energy in the InGaAs well is raised so that it lies close to the Fermi energy, with the corresponding charge storage in the well. Such an effect has been observed previously in the other studies

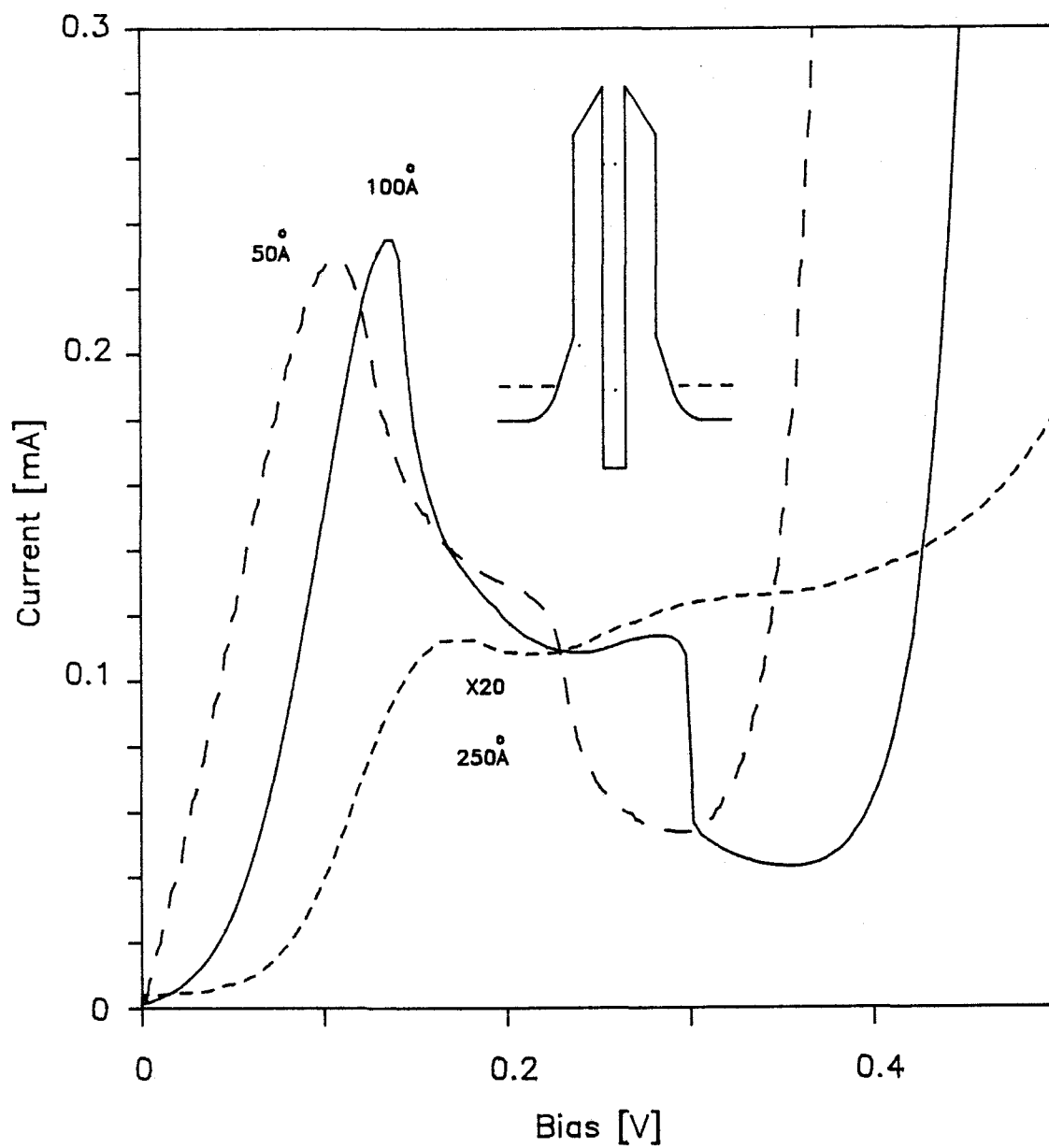


Figure 5.8: I-V characteristics of a pseudomorphic $\text{Al}_{0.35}\text{Ga}_{0.65}\text{As}/\text{In}_{0.2}\text{Ga}_{0.8}\text{As}$ RTDs with 50, 100, and 250 Å thick spacer layers measured at 77 K. The I-V curves of the pm-RTD with 250 Å thick spacer layer is magnified by 20 times. The inset figure is a calculated CB profile at thermal equilibrium.

of pm-InGaAs RTDs [77].

I-V characteristics of the pm-RTDs measured at 77 K with three different spacer thicknesses are shown in Figure 5.8. The smaller PVCR in AlGaAs/InGaAs RTDs compared to AlGaAs/GaAs RTDs is believed to arise from alloy scattering and material inhomogeneities due to indium segregation [53]. The change in I-V characteristics with increasing spacer layer thickness of the AlGaAs/InGaAs RTDs in Figure 5.8 show somewhat similar trends to the AlGaAs/GaAs RTDs for small spacer layer thicknesses. However, above 250 Å, there is a sudden drop of the PVCR (the I-V curve of the 250 Å spacer RTD is magnified by 20 times). RTDs fabricated with 500 and 1000 Å spacer layers do not show negative differential resistance (NDR) at all.

Under forward bias, the tunneling current initially flows from the emitter to the collector as unoccupied states are made available to electrons tunneling from the emitter. At resonance, electrons in the emitter side must surmount the emitter spacer barrier as well as tunnel through the first barrier in order to reach the InGaAs well, which reduces the total current density as in the previous case. Electrons in the InGaAs well must also tunnel through the second barrier as well as part of the collector spacer layer in order to reach the collector contact. However, since the resonant energy is lower than the C.B. edge on the collector side in the InGaAs case, electrons must tunnel through a wide effective barrier which greatly reduces the current at resonance in comparison to AlGaAs/GaAs devices. There exist the same trade-offs between current and PVCR with spacer layer thickness in the AlGaAs/InGaAs RTDs as in AlGaAs/GaAs RTDs. However, the critical spacer layer thickness of the former is much smaller than the latter due to

the fact that the resonance energy level in the InGaAs well is already below the CB edge at zero bias.

Figure 5.9 (a) and (b) respectively are I-V curves of the lattice matched $\text{Al}_{0.35}\text{Ga}_{0.65}\text{As}/\text{GaAs}$ and the pm- $\text{Al}_{0.35}\text{Ga}_{0.65}\text{As}/\text{In}_{0.2}\text{Ga}_{0.8}\text{As}$ RTDs with a 50 Å thick spacer layer measured at 77 and 1.8 K. The former shows improved device performance (PVCR, valley width, and peak current) at lower temperature while the latter does not. Improved performance at lower temperature of the former is achieved by reduction of ionized impurity scattering. The latter experiences alloy scattering due to the presence of the InGaAs layer in the well in addition to ionized impurity scattering. As discussed earlier in Chapter 3, InGaAs grown pseudomorphically on GaAs is strained due to lattice mismatch (7 % for InAs on GaAs). The strain changes the electronic properties of the material and creates intrinsic crystal imperfections. The InGaAs layer also increases interface roughness scattering due to In atom segregation during MBE growth [53]. Most of the scattering processes associated with the presence of the InGaAs layer, such as an alloy and interface roughness scatterings, are not strongly temperature dependent so performance of pm-RTDs at lower temperature is less improved than RTDs from the lattice matched system.

5.4 Pseudomorphic RTDs with Asymmetric Spacer

Pseudomorphic RTDs with asymmetric spacer layer configurations were studied in order to check the validity of the analysis of the role of spacer layers on pm-RTDs [78]. Pseudomorphic RTDs with asymmetric spacer layer thicknesses are composed of $\text{Al}_{0.35}\text{Ga}_{0.65}\text{As}$ barriers and

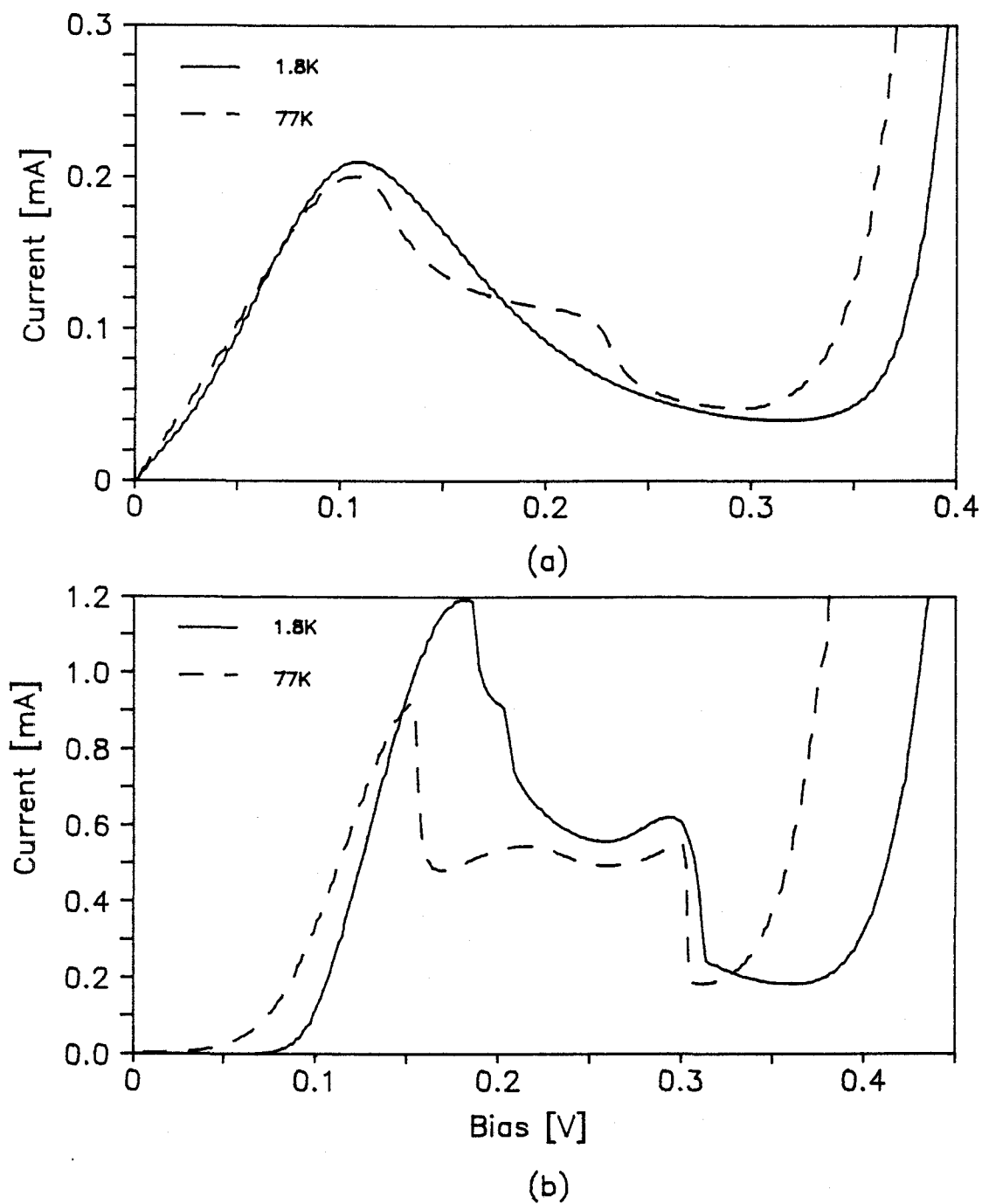


Figure 5.9: I-V characteristics of (a) the pm-Al_{0.35}Ga_{0.65}As/In_{0.2}Ga_{0.8}As RTD and (b) the lattice matched Al_{0.35}Ga_{0.65}As/GaAs RTD with 50 Å thick spacer layers measured at 77 (dashed line) and 1.8 K (solid line).

In_{0.1}Ga_{0.9}As wells. For one pm-RTD, a 50 Å spacer was grown on the top (emitter) side and a 500 Å spacer was placed on the substrate (collector) side for one sample, while the other sample had the spacer layer order reversed. RTDs with asymmetric spacer layer configurations are denoted as 50/500 RTDs (50 Å on top and 500 Å on substrate) and 500/50 RTDs after the spacer layer order from top to substrate. RTDs with asymmetric spacer layer configurations show very asymmetric I-V characteristics depending upon the bias direction. The detailed tunneling mechanisms through the two pm-AlGaAs/InGaAs RTDs with an asymmetric spacer layer is discussed separately.

5.4.1 The 50/500 RTD

Typical I-V characteristics of the 50/500 RTD measured at 77 and 1.8 K are shown in Figure 5.10. The dashed and the solid lines are the I-V curves at 77 and 1.8 K, respectively. The right inset figure is a profile of the metallurgical junction of the 50/500 RTD and the left inset figure is the CB profile at thermal equilibrium. The calculated ground state energy in the InGaAs well lies slightly below the Fermi level due to the effect of charge storage in the well which raises the ground state energy. The I-V curves of the RTD show several interesting features. First, large differences in the peak voltage (V_p) and the peak current density (J_p) are found to depend upon the bias polarity. Secondly, the I-V characteristics do not change significantly between 77 and 1.8 K in contrast to RTDs based on the lattice matched AlGaAs/GaAs system. The measured values of $V_p = 0.45$ at 77 K in forward bias (V_{CE} positive) appear to be due to tunneling through the first

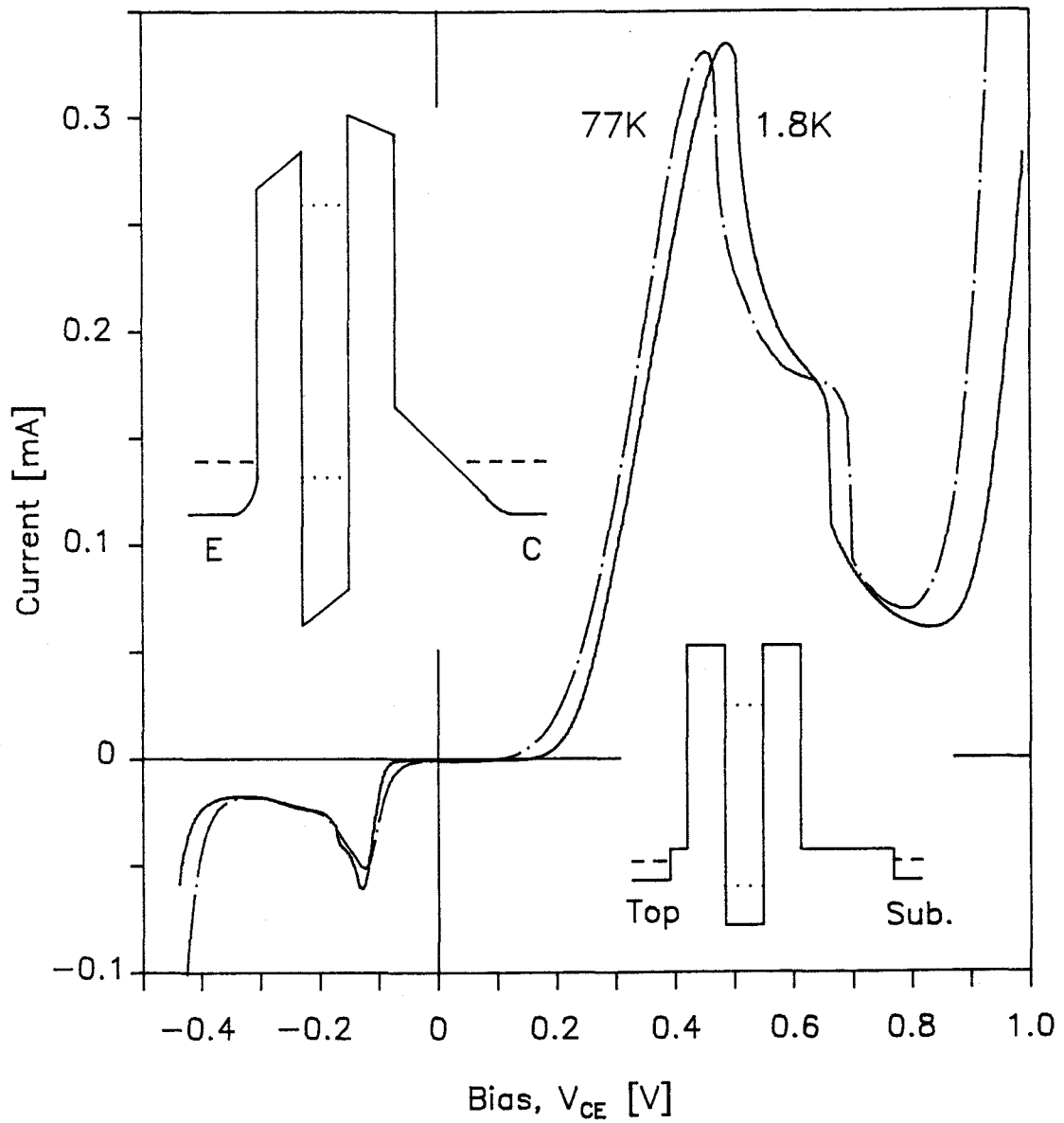


Figure 5.10: I-V characteristics of the 50/500 RTD measure at 77 and 1.8 K. The right and the left inset figures show the as-grown metallurgical CB edge and CB edge at thermal equilibrium, respectively.

excited state, while the peak voltage of 0.12 V for negative V_{CE} corresponds to tunneling through the ground state of the InGaAs well, based on the calculated position on these levels at zero bias. For positive V_{CE} , electrons from the emitter side must tunnel through the emitter and the collector barriers as well as the thick collector spacer barrier. Part of the thick collector spacer layer acts as a pseudo-barrier to ground state tunneling because the energy level in the well lies below the spacer barrier. The thick collector spacer barrier reduces the tunneling probability, which makes ground state tunneling undetectable in forward bias. However, tunneling through the ground state energy in reverse bias is possible via a two step transport processes. Electrons from the collector side are first accumulated in front of the collector barrier, which modifies the CB profile and the energy level in the accumulation layer is aligned with the ground state in the well at resonance. The accumulated electrons in the collector spacer layer tunnel through the rest of the double barrier as a second step. Thus V_p and J_p are smaller in reverse bias rather than in forward bias. The PVCs of the RTD in forward bias are 4.7 and 5.5:1, while those in reverse bias are 3.0 and 3.6:1 at 77 and 1.8 K, respectively. The enhancement of the PVCs and peak current are rather small compared to the RTDs based on the AlGaAs/GaAs material system. This result implies that additional scattering is present in the AlGaAs/InGaAs RTDs. This could be the result of alloy scattering and interface roughness scattering in the InGaAs layer which are temperature independent.

A set of four identical samples were studied in order to check the validity of the above interpretations. The samples have the same

structural parameters as the pm-AlGaAs/InGaAs RTDs with asymmetric spacer layer except for the spacer layer configuration. The samples contain 35, 50, 100, 250, and 500 Å thick symmetric spacer layers and each sample shows a V_p of 0.15, 0.145, 0.232, and 0.336 V at 77 K as shown in Figure 5.11. The straight line in the figure is a least-squares fit of the V_p 's as a function of the spacer layer thickness. The V_p of 0.145 V for the 100 Å spacer RTD was not included in the least squares fit and believed to be an experimental artifact. According to the data shown in Figure 5.11, the spacer layer has to be approximately 1000 Å thick for the V_p of 0.45 V to be ground state tunneling. Thus the V_p of 0.45 V is believed to be evidence of tunneling through the first excited level tunneling and the interesting features of this sample can be explained as follows.

5.4.2 The 500/50 RTD

The solid line in Figure 5.12 is the I-V characteristics of the 500/50 RTD at 1.8 K. The dashed line in Figure 5.12 shows the I(-V) of the 50/500 RTD at 1.8 K for an easy comparison of the two RTDs. The inset figure shows the C.B. profile of the 500/50 RTD at thermal equilibrium. The general trends in this RTD are similar to the previous 50/500 RTD except that the bias polarity is reversed. The interpretations given for the 50/500 RTD are valid for this device too. However, the PVCr and valley width of the 500/50 RTD are inferior to the previous 50/500 RTD while the current densities are higher. The PVCrs of the 500/50 RTD are 5.7 and 1.4:1 in forward and reverse bias, respectively. It is worth to mentioning again that the PVCrs of the

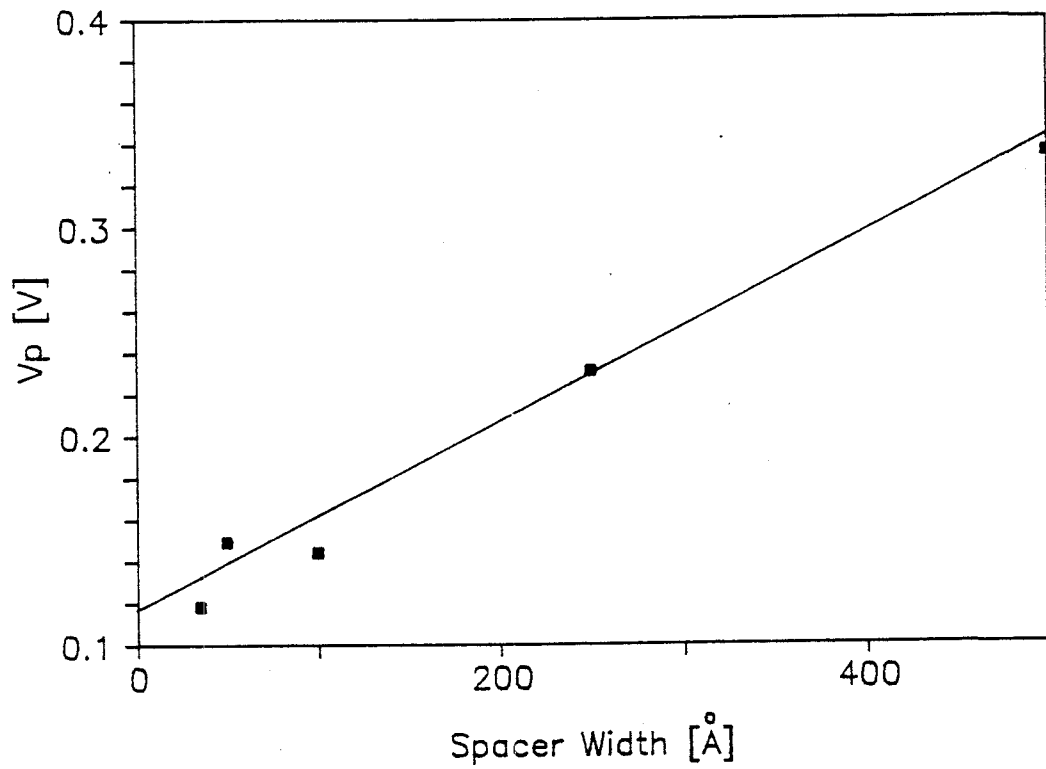


Figure 5.11: Peak voltage position of the pm-Al_{0.35}Ga_{0.65}As/In_{0.1}Ga_{0.9}As RTD with symmetric 35, 50, 100, 250, and 500 Å thick spacer layers measured at 77 K.

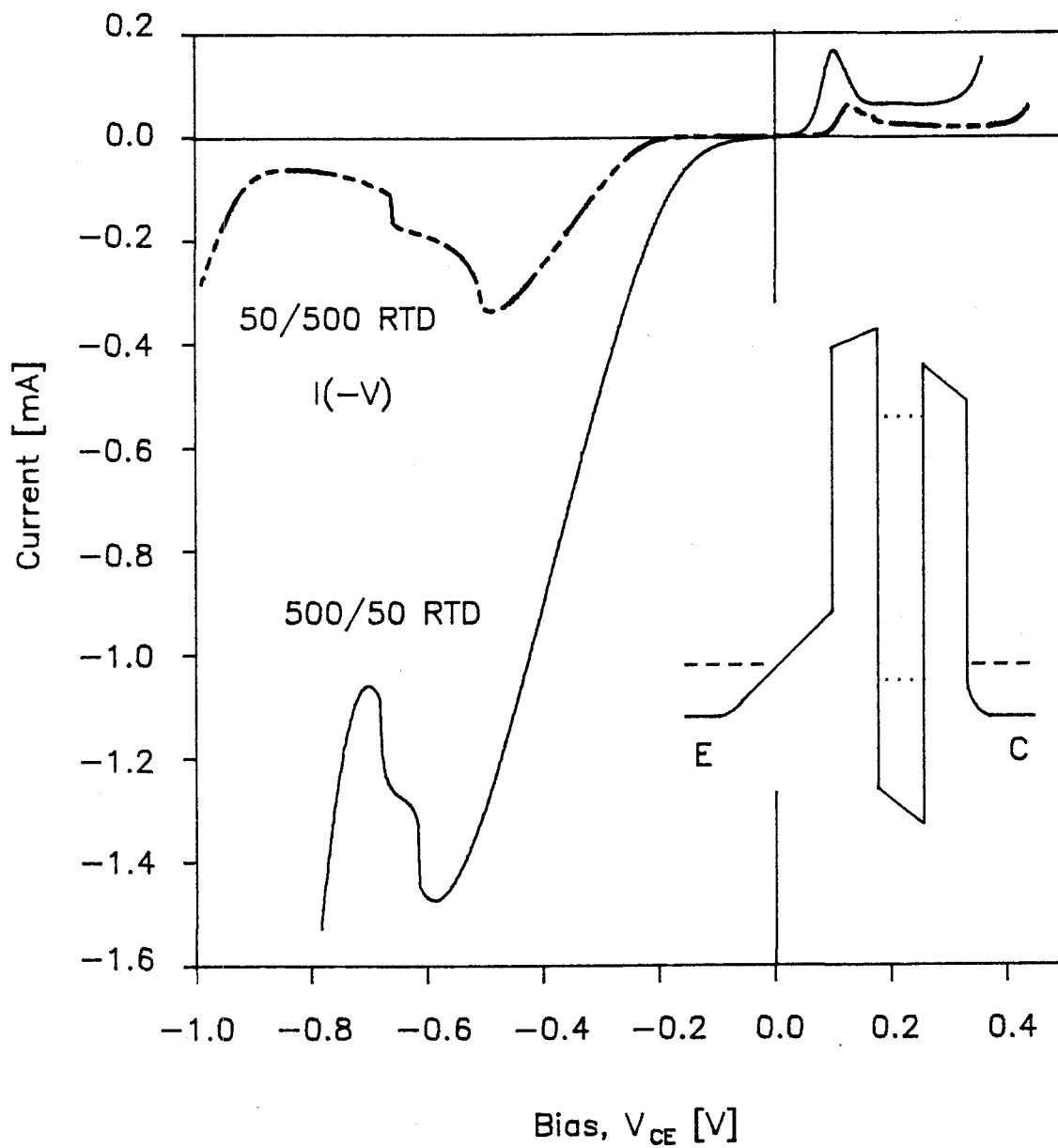


Figure 5.12: I - V characteristics of the 500/50 RTD measured at 1.8 K. The dotted curve in the figure is that of the 50/50 RTD with $I(-V)$. Inset figure shows the CB profile at thermal equilibrium.

50/500 RTD is 5.5 and 3.6:1 for the same bias configurations.

The reduction in the PVCR of the 500/50 sample is explainable in terms of silicon out diffusion in which silicon atoms in GaAs segregate during molecular beam epitaxy due to Fermi level pinning at the semiconductor surface [58]. The segregation length varies from a few tens of angstroms to a few hundreds of angstroms depending upon the growth temperature. The 50/500 RTD which has a thicker collector spacer layer (i.e. a thicker diffusion barrier for silicon from the substrate side) than the 500/50 RTD reduces ionized impurity scattering in the well. The higher current through the 50/500 RTD is not surprising since it is achieved at a cost of valley width narrowing, which implies enhancement of non-resonant current. Thus the former exhibits a better PVCR and a wider valley width than the latter. The RTD based on the $\text{Al}_{.35}\text{Ga}_{.65}\text{As}/\text{GaAs}$ material system with a 50 Å symmetric spacer layer shows twice as much current as the identical RTD with a 1000 Å spacer layer. The higher current density of the 500/50 RTD compared to the 50/500 RTD may be due to enhancement of the effective doping concentration in active region of the RTD (between the two barriers) due to silicon out diffusion during MBE growth.

The novel phenomena observed from pm-RTDs with asymmetric spacer layers could also be realized from lattice matched $\text{Al}_x\text{Ga}_{1-x}\text{As}/\text{GaAs}$ RTDs with asymmetric two step barriers. Such an RTD would have an extra barrier adjacent to one barrier with less aluminium concentration than the tunnel barrier. The extra barrier acts differently depending upon its relative height with respect to the quasi-bound energy level in the well (E_q) and E_F at the contact layer. If E_q lies below both E_F and the extra barrier height (E_{ex}), the extra barrier acts the same as in the

pm-RTD with asymmetric spacer. If E_q is below E_{ex} but above E_F , the device behaves similarly to the asymmetric pm-RTD with effectively less doping concentration in the contact layer. If E_q lies above E_F but below E_{ex} , it acts as a spacer layer. The proposed device provides much a wider degree of freedom in designing RTDs by different combination of E_F , E_q , and E_{ex} . Fabrication of these new devices could help to further the understanding of the RTD, at least in terms of space charge formation by removing the complexity due to the InGaAs layer. The idea of an extra barrier could also be realized in pm-AlGaAs/InGaAs RTDs so that the extra AlGaAs barrier acts as spacer layer [79].

5.4.3 Magnetic Field Study

Figure 5.13 (a) and (b) are SdH data showing the differential conductance of the 500/50 and the 500/50 RTDs at a fixed bias as a function of the magnetic field ($B \parallel J$), respectively. The former is forward biased and the latter is reverse biased so electrons first encounter the thicker of the two spacer layers for both cases. When both RTDs are oppositely biased, the conductance of the RTDs either decreases quadratically without any oscillations or shows very weak oscillations up to a magnetic field strengths of 8 Tesla. Figure 5.14 (a) shows the magneto-quantum oscillation period of two RTDs as a function of applied bias. The bias direction is the same as described in Figure 5.13. The squares and the triangles are the plot of oscillation periods as a function of bias for the 50/500 and the 500/50 RTDs, respectively. The solid lines are a least-squares fit of the magneto-quantum periods. The magneto-quantum oscillation period, B_f , in

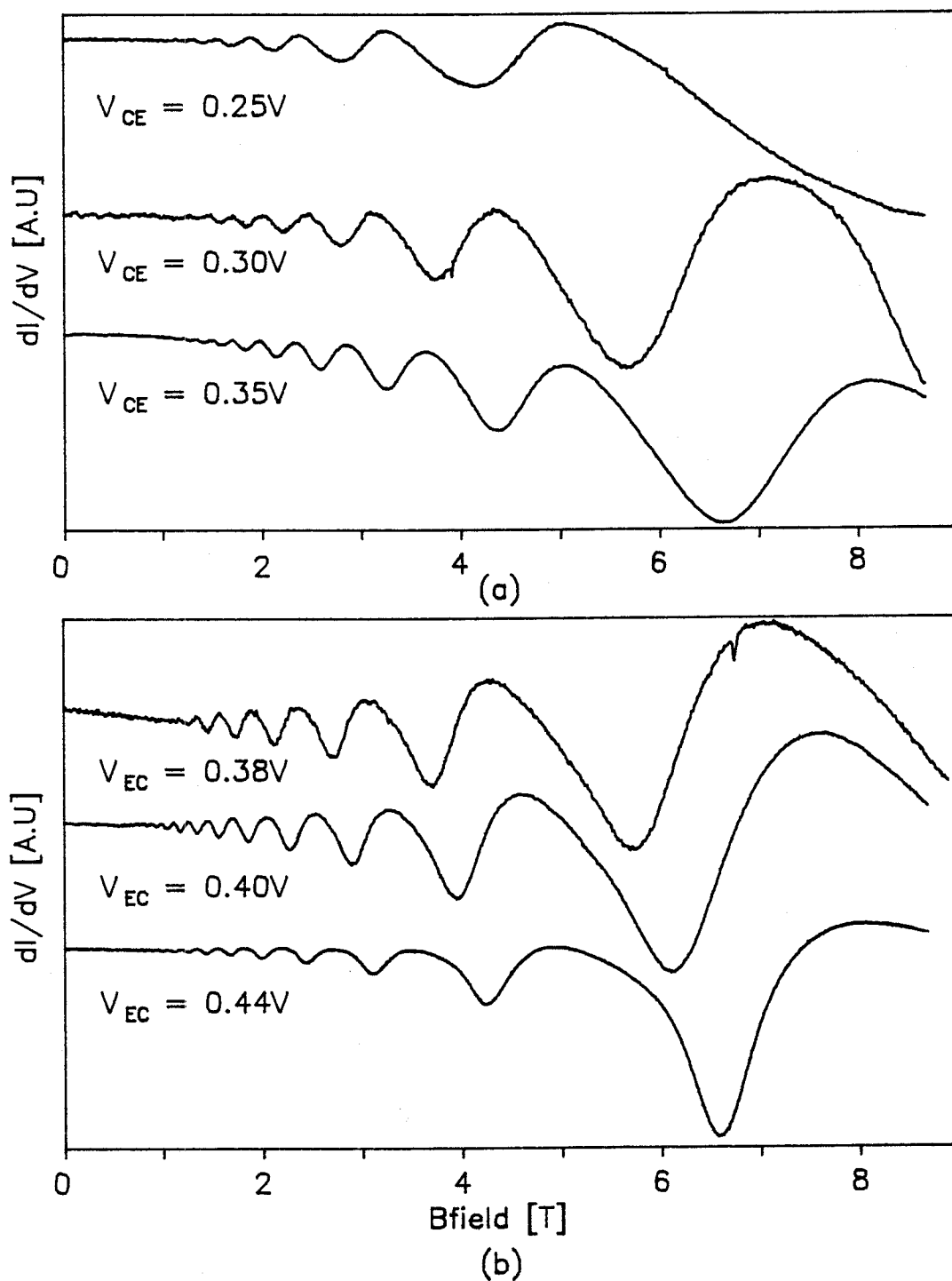


Figure 5.13: Shubnikov-de Haas oscillations of the (a) 500/50 and (b) 50/500 RTDs.

Eq. (5.14) is expressed again here for convenience.

$$B_f = \frac{m^*}{\hbar e} [E_F - E_{a0}] = \frac{m^*}{\hbar} \alpha V_a \quad (5.16a)$$

$$B_f = \frac{m^*}{\hbar e} [E_F - E_{q0} - (\hbar\omega_L)] = \frac{m^*}{\hbar e} [\beta e V_a - (\hbar\omega_L)] \quad (5.16b)$$

where Eq. (5.16a) and (5.16b) refer respectively to accumulation and inelastic tunneling as before. The slope of the least-squares fit of the 500/50 and the 50/500 RTDs are 34.5 and 20.75 Tesla/Volt, respectively. The slope is either $m^*\alpha/\hbar e$ or $m^*\beta/\hbar e$ depending on its origin as discussed previously. The higher slope corresponds to a higher α or β which signifies a larger portion of applied voltage drop occurs across the 500 Å spacer layer of the 500/50 RTD compared to that of the 50/500 RTD. Thus a 500 Å spacer layer placed in the collector side becomes effectively narrower than that in emitter side, which agrees well with a directional Si atom diffusion toward surface due to surface Fermi level pinning during MBE growth.

Figure 5.14 (b) is the forward I-V data for the 500/50 RTD at 1.8 K with a magnetic field $B = 8.7$ T and 0 T. The figure is shown here to resolve the origin of the oscillations. The two I-V curves measured at $B = 8.7$ and 0 Tesla do not show much difference. A tiny peak marked as an L0 in the valley region of the I-V curve is LO phonon assisted tunneling feature [66]. The bias voltage separation between the LO phonon peak at 203.3 mV and V_p at 106.3 mV is 97 mV. The energy separation between E_F and E_{q0} has to be the same as an $\text{In}_{0.1}\text{Ga}_{0.9}\text{As}$ LO phonon energy of 36 meV [76] in order for this to be a LO phonon assisted tunneling process. Thus the voltage drop between E_F and E_{q0} is 36 mV which is 17.7 % of the total bias at $V_a = 203.3$ mV. The relative voltage drop across each region of the device is assumed to be

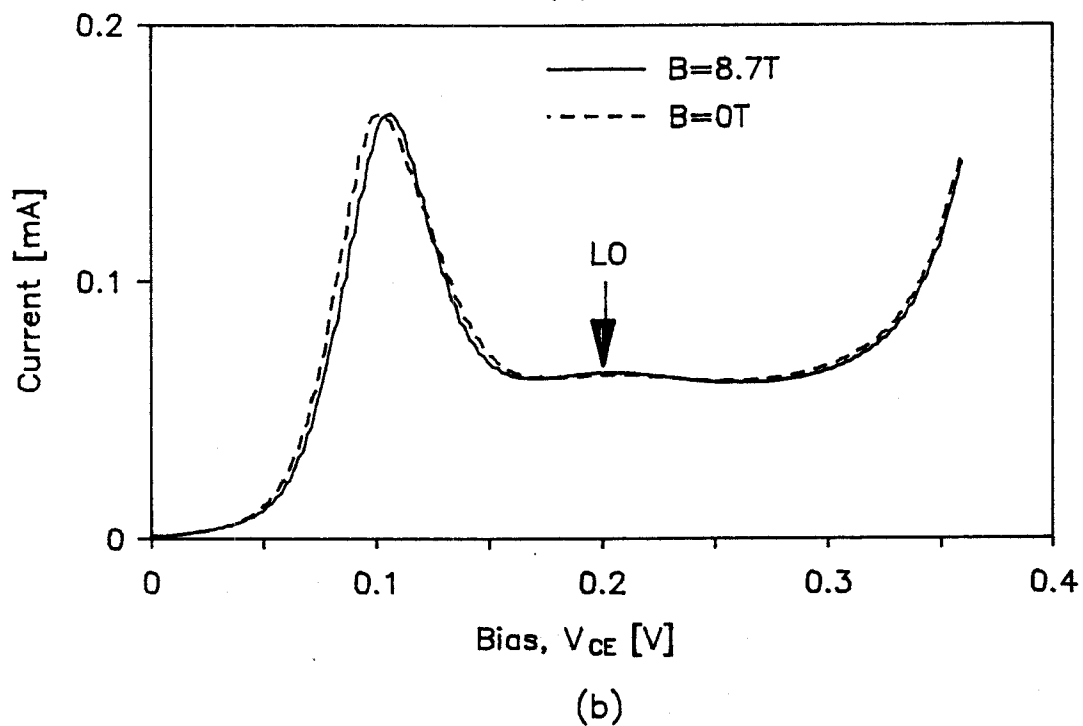
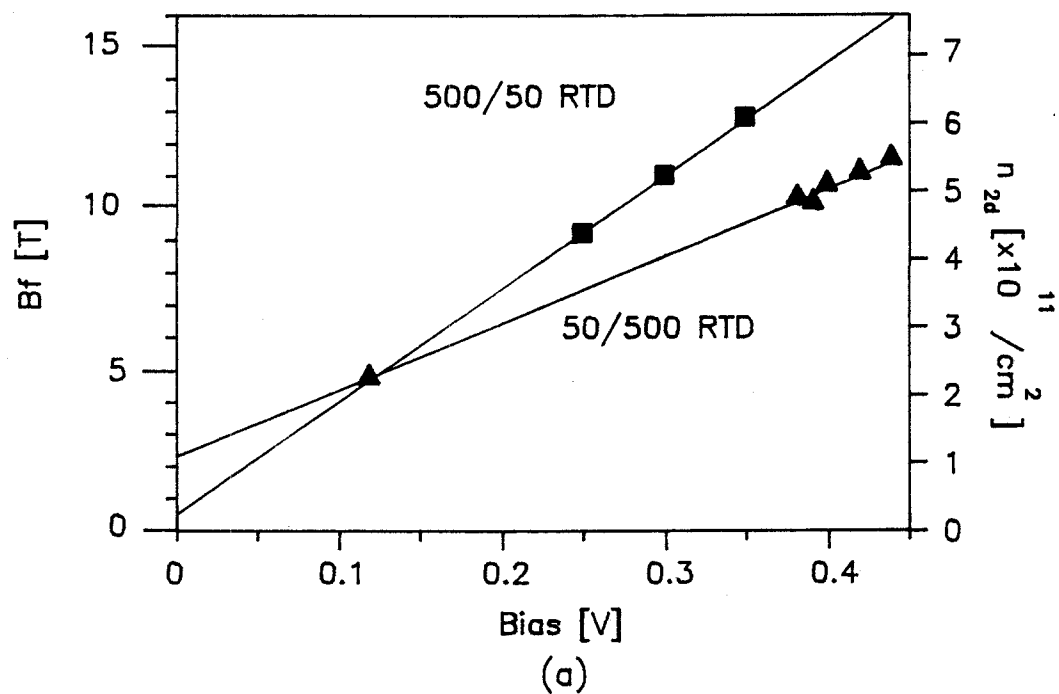


Figure 5.14: (a) SdH oscillation period of the 500/50 and 50/500 RTD as a function of applied bias. The right ordinate shows a two-dimensional carrier density with the corresponding B_f . (b) Forward I-V characteristics of the 500/50 RTD measured at 1.8 K with $B=8.7$ Tesla and 0 field. The peak marked as LO is LO phonon assisted tunneling feature.

unchanged if the device is biased in the valley region of the I-V curve, because current through the device is more or less constant in the valley region, so approximately 17.7 % of the applied bias drop between E_f and E_{q0} is assumed. Thus, $E_f - E_{q0}$ is estimated as 44.27 and 53.12 meV at V_a of 250 and 300 mV, respectively. $E_f - E_{q0}$ or $E_{a0} - E_{q0}$ are calculated to be 14.9 and 17.9 meV respectively with corresponding α or β of 5.96 %. If α is 5.96 %, β has to be 11.74 % since $\alpha + \beta$ has to be 17.7 %. The SdH oscillations due to inelastic scattering with the emission of an LO phonon show much higher oscillation period than that from the accumulation layer and RTDs containing the InGaAs layers in the well do not show the former type oscillations. Thus SdH oscillations are assumed to be from accumulation layer and α and β are estimated to be 5.96 and 11.74 % of the applied bias, respectively.

Assuming the origin of the oscillations is the accumulation layer, its periodicity is directly related to the carrier density by $n_{2d} = 2eB_f/h$, where $1/B_f = \Delta(1/B)$ and n_{2d} is a two dimensional carrier density [13] which is shown in the right ordinate of the Figure 5.14 (a). The 500/50 RTD shows a higher n_{2d} which is consistent with a higher current through the 500/50 RTD, and an effectively thicker spacer layer due to Si out diffusion.

The effect of an asymmetric spacer layer structure on transport in pseudomorphic $Al_{.35}Ga_{.65}As/In_{.1}Ga_{.9}As$ RTDs has been shown in this chapter. A thick spacer layer in front of the first barrier results in electron transport via a two step conduction process while, for a thick spacer behind the second barrier, the spacer layer acts as an effective barrier. Tunneling is through the ground state energy of the InGaAs well when the thick spacer layer is located at the leading edge of the

device while it is through the first excited state of the InGaAs well when the thick spacer layer is at the trailing edge of the diode. The RTD with a thicker spacer layer on the substrate side exhibits better performance than the RTD with a reversed order spacer layer configuration by suppressing impurity scattering in the active region of the device. Shubnikov-de Haas oscillations as well as I-V characteristics obtained from these devices shows strong dependence on the bias polarity and gives strong evidence of silicon dopant outdiffusion during MBE growth.

6. Summary and Conclusions

The purpose of this research has been to characterize the carrier transport in resonant tunneling diodes. Particular attention has been given to certain structural parameters; viz spacer layers and the presence of an InGaAs layer in the well. To accomplish this purpose, RTDs with various combinations of spacer layer configurations and InGaAs layers with different indium compositions in the well have been fabricated and characterized via electric and magnetic field measurements.

Several conclusions may be drawn concerning the results and analysis of the resonant tunneling diodes presented in this thesis. The main conclusions concerning the structural parameters on the device performance in the lattice matched and the pseudomorphic $\text{Al}_x\text{Ga}_{1-x}\text{As}/\text{In}_y\text{Ga}_{1-y}\text{As}$ RTDs may be summarized as follows:

- (1) An electric and magnetic field study of lattice matched AlGaAs/GaAs and the pseudomorphic AlGaAs/InGaAs RTDs grown by molecular beam epitaxy is presented. The valley region of the I-V curve in the presence of a quantizing magnetic field ($B\parallel J$), exhibits a large number of tunneling peaks which are shown to be due to phonon assisted tunneling and to tunneling between Landau levels. The former do not change peak position while the latter peaks change as a function of magnetic field since the phonon energy does not change with magnetic field while the spacing between the Landau ladder does change. Shubnikov de-Haas

measurements show evidence of a two dimensional quasi-bound state in the accumulation layer of the emitter and of LO phonon assisted tunneling through Landau levels in the well.

- (2) The influence of a symmetric spacer layer on lattice matched AlGaAs/GaAs RTDs has been studied. The device performance improves as the spacer layer becomes thicker below its critical width since ionized impurity scattering is reduced. The peak voltage position shifts to higher values as the spacer layer thickness increases which can easily be explained in terms of the series resistance. The thicker the spacer layer, the higher the series resistance and, consequently, the peak voltage position shifts to higher values. The spacer layer, above its critical thickness, reduces the current through the RTD significantly while the PVCR of the device stays relatively constant. This is due to the formation of a spacer barrier which acts as an extra barrier. As the spacer barrier height increases, the number of carriers available for tunneling decreases. The exact design of an optimal spacer layer thickness for a maximum peak to valley current ratio is complicated by the trade-off between improved performance due to the reduction in impurity scattering and the decreased performance because of suppression of resonant tunneling currents due to the spacer barrier.
- (3) The general performance (PVCR, valley width, and peak current) of the pm-RTDs studied is inferior to lattice matched diodes due to alloy scattering from the InGaAs layer as well as interface roughness scattering due to possible indium segregation. The

effect of the spacer layer on the pseudomorphic AlGaAs/InGaAs RTD performance depends upon the relative energy position of the quasi-bound well state. Spacer layers at the leading and trailing edges of the device act differently due to the formation of space charge regions. Spacer layers at the trailing edge of the device behave as extra tunnel barriers so they reduce the tunneling probability greatly. Spacer layers at the leading edge of the RTD form accumulation layers and reduce the current through the device similarly to that found in lattice matched AlGaAs/GaAs RTDs.

- (4) Pm-RTDs with asymmetric spacer layers have also been investigated. There is very strong evidence that the spacer layers play different roles depending upon their position: spacer layers located at the leading edge of the device form accumulation layers while those at the trailing edge act as pseudo-tunnel barriers. Pm-AlGaAs/InGaAs RTDs with asymmetric spacer layers show novel tunneling phenomena depending upon the bias directions. Tunneling is through the ground state energy of the InGaAs well when the thick spacer layer is at the leading edge of the device while it is through the first excited state of the InGaAs well when the thick spacer layer is at the trailing edge of the diode. Those observations are fully consistent with the different role of spacer layers predicted from pm-RTDs with symmetric spacer layers. The asymmetric pm-RTD with a thick spacer layer on the substrate side yield better performance than when the thick spacer layer is on top side. This result may be due to growth artifacts as follows. Silicon

impurities tends to outdiffuse during MBE growth due to surface Fermi level pinning. Thus, the RTD with a thicker spacer layer on the substrate side shows better performance. Shubnikov-de Haas oscillations obtained from these RTDs are also quite different depending upon the bias direction. Shubnikov de-Haas oscillations of RTDs are always superior when the diodes are biased in such a way that the thick spacer layer is at the leading edge of the diodes. The bias dependence of the SdH oscillation features provide strong evidence that these oscillations originate from the accumulation layer. Analysis of the SdH oscillation period of the two diodes also provides evidence of silicon outdiffusion which agrees well with the analysis obtained from I-V characteristics.

- (5) Theoretical calculations of the current-voltage characteristics of RTD are also performed. The fit between the calculated and measured I-V characteristics is poor, however, and a more complete theory, which includes carrier scattering and diffusion in the heavily doped contact region, remains as further work. A significant improvement in the calculations seems necessary to achieve a reasonable fit between the measured and the theoretical values.

Bibliography

- [1] R. Tsu and L. Esaki, Appl. Phys. Lett. **22**, 542, 1973
- [2] A. Yariv, "Introduction to optical electronics", pp. 60, 2nd ed. Holt, Rinehart and Winston, New York, 1976
- [3] S. Luryi, Appl. Phys. Lett. **47**, 490, 1985
- [4] F. Capasso, K. Mohammed and A.Y. Cho, IEEE J. of Quantum Electronics, **QE-22**, 1853, 1986
- [5] A. Douglas Stone and P.A. Lee, Phys. Rev. Lett. **54**, 1196, 1985
- [6] L.L. Chang, L. Esaki and R. Tsu, Appl. Phys. Lett. **24**, 593, 1974
- [7] A.Y. Cho and J.R. Arthur, Progr. Solid State, **10**, 157, 1975
- [8] T.C.L.G. Sollner, W.D. Goodhue, P.E. Tannenwald, C.D. Parker and D.D. Peck, Appl. Phys. Lett. **43**, 588, 1983
- [9] T.C.L.G. Sollner, P.E. Tannenwald, D.D. Peck and W.D. Goodhue, Appl. Phys. Lett. **45**, 1319, 1984
- [10] T.P.E. Broekaert, W. Lee and C.G. Fonstad, Appl. Phys. Lett. **53**, 1545, 1988
- [11] J.N. Schulman, J. Appl. Phys. **60**, 3954, 1986
- [12] W.D. Goodhue, T.C.L.G. Sollner, H.Q. Le, E.R. Brown and B.A. Vojak, Appl. Phys. Lett, **49**, 1086, 1986
- [13] M. Tsuchiya, H. Sakaki and J. Yoshino, Japanese J. of Appl. Phys. **24**, L466, 1985
- [14] Collins, D. Lowe, and J.R. Barker, J. Appl. Phys. **63**, 142, 1988
- [15] B. Rico and M. Ya. Azbel, Phys. Rev. B **29**, 1970, 1984
- [16] H.M. Yoo, S.M. Goodnick and J.R. Arthur, Appl. Phys. Lett. **56**, 86, 1990
- [17] D.K. Ferry and D.R. Fannin, "Physical Electronics", Chapter 5, Addison-Wesley, Reading, Massachusetts, 1971
- [18] D.J. Vezzetti and M.M. Cahay, J. Phys. D **19**, L53, 1986
- [19] I.I. Gol'dman and V. Krivchenokov, Problems in Quantum Mechanics, pp.60, Addison-Wesley, Reading, Massachusetts, 1961

- [20] E.O. Kane, "Basic concepts of tunneling", in Tunneling Phenomena in solids, pp.1-11, edited by Elias Burstein and Stig Lundqvist, Plenum Press, New York, 1969
- [21] K. Araki, J. Appl. Phys. **62**, 1059, 1987
- [22] G. Bastard and J.A. Brum, IEEE J. Quantum Electronics, QE-22, 1625, 1986
- [23] W.R. Frensley, J. Vac. Sci. Technol. **B 3**, 1261, 1985
- [24] H. Kroemer and Qi-Gao Zhu, J. Vac. Sci. Technol. **21**, 551, 1982
- [25] V.J. Goldman, D.C. Tsui and J.E. Cunningham, Phys. Rev. **B 35**, 9387, 1987
- [26] H. Ohnishi, T. Inata, S. Muto, N. Yokoyama and A. Shibatomi, Appl. Phys. Lett. **49**, 1248, 1986
- [27] W. Poetz, J. Appl. Phys. **66**, 2458, 1989
- [28] W.R. Frensley, Solid State Electronics, **31**, 739, 1988
- [29] M. Cahay, M. McLennan, S. Datta and M.S. Lundstrom, Appl. Phys. Lett. **50**, 612, 1986
- [30] D. Landheer and G.C. Aers, "Self-consistent calculations of tunneling current of double barrier resonant tunneling diodes using 1D density of states", presented in Proc. of Quantum Wells for Optics and Optoelectronics Topic Meeting, Salt Lake City, Utah, March 1989
- [31] R. Eisberg and R. Resnick, "Quantum physics of atoms, molecules, solids, nuclei, and particles", pp. 138, John Wiley & Sons, 2nd ed. New York, 1985
- [32] F. Capasso, K. Mohammed and A.Y. Cho, Physica, **134B**, 487, 1985
- [33] F. Capasso and R.A. Kiehl, J. Appl. Phys. **53**, 1366, 1985
- [34] F. Capasso, K. Mohammed and A.Y. Cho, IEEE J. Quantum Electronics, QE-22, 1853, 1986
- [35] F. Capasso, "New high-speed quantum well and variable gap superlattice devices", in "Picosecond Electronics and Optoelectronics", edited by G.A. Mourou, D.M. Bloom and C.H. Lee, pp. 112-130, Springer Series in Electrophysics 21, Berlin, Heidelberg, Springer-Verlag, 1985
- [36] A.R. Bonnefoi, D.H. Chow and T.C. McGill, Appl. Phys. Lett. **47**, 888, 1985

- [37] Y. Nakata, M. Asada and Y. Suematsu, IEEE J. Quantum Electronics, **QE-22**, 1880, 1986
- [38] S. Luryi and F. Capasso, Appl. Phys. Lett. **47**, 1347, 1985
- [39] A.R. Bonnefoi, T.C. McGill and R.D. Burnham, IEEE Electron Device Letters, **EDL-6**, 636, 1985
- [40] A.A. Lakhani and R.C. Potter, Appl. Phys. Lett. **52**, 1684, 1988
- [41] S. Sen, F. Capasso, A.Y. Cho and D. Sivco, IEEE Electron Devices, **ED-34**, 2185, 1987
- [42] K.G. Gunter "Compound Semiconductors", Vol. I, pp. 313, ed by R. Wolfe, Academic Press Inc., New York, 1974
- [43] J.R. Arthur, J. Appl. Phys. **39**, 4032, 1968
- [44] A.Y. Cho and H.C. Casey, Appl. Phys. Lett. **25**, 288, 1974
- [45] L. Esaki and L.L. Chang, Phys. Rev. Lett. **33**, 495, 1974
- [46] K. Ploog and K. Graf, "Molecular beam epitaxy of III-V compounds", Springer-Verlag, 1974
- [47] J.T. Ebner, "Growth, fabrication and characterization of pseudomorphic GRIN-SCH laser diodes", Ph. D. thesis, OSU, 1990
- [48] C.E.C. Wood in "The technology and physics of molecular beam epitaxy," edited by E.H.C. Parker, p. 61, Plenum Press, New York and London, 1985
- [49] F.Alexandre, L. Goldstein, G. Leroux, M.C. Joncour, H. Thibierge and E.V.K. Rao, J. Vac. Sci. Technol. **B**, 950, 1985
- [50] J.M. Van Hove and P.I. Cohen, Appl. Phys. Lett **47**, 726, 1985
- [51] J.W. Matthews and A.E. Blakeslee, J. Vac. Sci. Technol. **14**, 989, 1977
- [52] P.L. Gouley, I.J. Fritz and L.R. Dawson, Appl. Phys. Lett. **52**, 377, 1988
- [53] J.T. Ebner and J.R. Arthur, J. Vac. Sci. Technol. **A5**, 2007, 1987
- [54] D.C. Radulescu, W.J. Schaff, L.F. Eastman, J.M. Ballingall, G.O. Ramseyer and S.D. Hersee, J. Vac. Sci. Technol. **B7**, 1989
- [55] B.T. Meggitt, E.H.C. Parker and R.M. King, Appl. Phys. Lett. **33**, 528, 1978
- [56] G.E. Stillman and C.M. Wolfe, Thin Solid Films **31**, 69, 1976

- [57] R.E. Honig and D.A. Kramer, "Vapor pressure data for solid and liquid elements", in RCA Review, 285, 1969
- [58] E.F. Schubert, J.M. Kuo, R.F. Kopf, A.S. Jordan and H.S. Luftman, presented at 10th MBE workshop, North Carolina State University, 1989, to be published in J. Vac. Sci. Technol. B 1990
- [59] H.M. Yoo, 'Lift-off photolithography', MS project I, OSU, 1986
- [60] F.W. Sheard and G.A. Toombs, Appl. Phys. Lett. 52, 1228, 1988
- [61] T.J. Foster, M.L. Leadbeater, L.Eaves, M. Henini, O.H. Hughes, C.A. Payling, F.W. Sheard, P.E. Simmonds, G.A. Toombs, G. Hill and M.A. Pate, Phys. Rev. B39, 6205, 1989
- [62] E.E. Mendez, L. Esaki and W.I. Wang, Phys. Rev. B33, 2893, 1986
- [63] C.A. Payling, C.R.H. White, L. Eaves, M.L. Leadbeater, J.C. Portal, P.D. Hodson, D.J. Robbins, R.H. Wallis, J.I. Davis and A.C. Marshall, Superlattice and Microstructures 6, 193, 1989
- [64] L. Eaves, G.A. Toombs, F.W. Sheard, C.A. Payling, M.L. Leadbeater, E.S. Alves, J.C. Portal, G. Hill and M.A. Pate, Appl. Phys. Lett. 52, 212, 1988
- [65] J.G. Adler and J.E. Jackson, Rev. Sci. Instrum. 37, 1049, 1966
- [66] C.A. Payling, E.S. Eaves, T.J. Foster, M. Henini, O.H. Hughes, P.E. Simmonds, F.W. Sheard, G.A. Toombs, and J.C. Portal, Surface Science, 404, 196, 1988
- [66] V.J. Goldman, D.C. Tsui and J.E. Cunningham, Phys. Rev. B 36, 7635, 1987
- [67] S. Adachi, J. Appl. Phys. 58, R1, 1985
- [68] L. Eaves et al., in Springer Series in Solid State Science 83: "Physics and Technology of Submicron Structures", edited by H. Heinrich, G. Bauer and F. Kuchar (Spring-Verlag, Berlin, 1988), P.74
- [69] S. Ben Amor, K.P. Martin, J.J.L. Rascol, R.J. Higgins, R.C. Potter, A.A. Lakhani and H. Hier, Appl. Phys. Lett. 54, 1908 (1989)
- [70] G. Burns, C.R. Wie, F.H. Dacol, G.D. Pettit, and J.M. Woodall, Appl. Phys. Lett. 51, 1919, 1987
- [71] H.M. Yoo, S.M. Goodnick, J.R. Arthur and M.A. Reed, J. Vac. Sci. Technol., B8, 370, 1990.

- [72] K. Inoue, H. Sakaki and J. Yoshio, *Appl. Phys. Lett.* **46**, 973, 1985
- [73] S.M. Sze, "Physics of semiconductor devices", 2nd ed. pp. 614, John Wiley & Sons, New York, 1981
- [74] B.R. Nag, "Electron Transport in Compound Semiconductors", pp. 82, Springer Series in Solid-State Science 11, Springer-Verlag, 1980
- [75] R.A. Smith, "Semiconductors", 2nd ed. pp. 99, Cambridge University Press, Cambridge, 1979
- [76] T.G. Anderson, Z.G. Chen, V.D. Kulakovskii, A. Uddin and J.T. Vallin, *Phys. Rev.* **B37**, 4032, 1988
- [77] M.A. Reed and J.W. Lee, *Appl. Phys. Lett.* **50**, 845, 1987
- [78] H.M. Yoo, S.M. Goodnick and J.R. Arthur, "Electric and magnetic field study of spacer layer thickness effects in AlGaAs/InGaAs resonant tunneling diodes", to be published in 1990 Proceedings of SPIE, Quantum Well and Superlattice Physics III
- [79] H.M. Yoo, S.M. Goodnick and J.R. Arthur, "Transport in $\text{Al}_x\text{Ga}_{1-x}\text{As}/\text{In}_y\text{Ga}_{1-y}\text{As}$ resonant tunneling diode with asymmetric layers", submitted to 6th International Conference on Molecular Beam Epitaxy, San Diego